Computer Modelling of First Stage Solid State Sintering at Particle Scale

Thesis submitted for the degree of Master of Philosophy

At University of Leicester

by

Wendong Luo

Department of Engineering

University of Leicester

March 2018

Computer Modelling of First Stage Solid State Sintering at Particle Scale

Wendong Luo

Department of Engineering

University of Leicester

Abstract

Sintering, originated in ancient civilization thousands of years ago, is a typical process applied to ceramic and metal component manufacture by heating material powders until particles are fully densified and adhere to each other. With the development of controlled sintering of metal and ceramics in the early twentieth century, the technological background for modern theory and practice of sintering was established, and then experienced fast growth after the mid-1940s. In sintering study, empirical and theoretical ways are used to understand sintering behaviours and connect behaviours to sintering variables. The experimental studies and theoretical analyses have been performed quite well over the last 60 years when providing an outstanding qualitative understanding of sintering in terms of the driving forces, the mechanisms, and the influence of major sintering variables such as the particle size, temperature and applied pressure. However, the analytical solutions of experiments and the models of sintering are not so successful when providing a quantitative description for most sintering. With the development of computer technology, the powerful computing capability of computer allows us to build a complex sintering model with more sintering variables that provide a more accurate description on the effects of sintering variables.

In this thesis, a computational model is firstly presented to validate and correct the previous assumption of fast surface diffusion for modelling first-stage sintering by coupled grain-boundary and surface diffusion. There are two main achievements in this study. To be specific, the first one is providing a numerical solution for the curvature at a triple junction (pore tip), and the second one is demonstrating the effect of surface diffusion on first-stage sintering by coupled grain-boundary and surface diffusion. Then a temperature-dependent model is presented to study the effect of the fast heating rate on sintering. Based on the analysis of numerical results, the effect of spark plasma sintering on densification can be partially attributed to its fast heating rate. Finally, a computational model is presented to qualify and quantify the effects of inhomogeneity concerning sintering variables on sintering kinetics.

The work in this thesis is entirely computational and guided by existing experimental data and observations in the literature.

Acknowledgements

I would like to thank my supervisor, Professor Jingzhe Pan, for his guidance and encouragement throughout my MPhil study. Particularly, I am very grateful to Prof Pan's encouragement when I suffered a severe heath problem and experienced a long-term medical suspension in my MPhil study. If without his encouragement, I might give up my MPhil study.

I would also like to thank the co-supervisor of my project, Hongbiao Dong, for his invaluable advices. Supports from general staff in Department of Engineering, University of Leicester are highly appreciated.

Finally, I would like to thank all my colleagues, friends and family, especially my parents. Without the constant support from all of them, I would never be able to finish my MPhil study.

Published Papers from This MPhil Project

W. Luo and J. Pan, "Effects of Surface Diffusion and Heating Rate on First-Stage Sintering That Densifies by Grain-Boundary Diffusion," *J. Am. Ceram. Soc.*, **98**[11] 3483-3489 (2015).

Contents

List of Symbols

R_0	Initial radius
a	Neck Radius
γ_s	Surface tension
γ_{gb}	Grain-boundary tension
θ	Dihedral angle at the triple junction
j	Diffusive flux
μ	Chemical potential
D	Diffusivity
δ	Thickness of diffusion layer
k	Boltzmann's constant
T	Sintering temperature
s	Local coordinate along diffusion path
σ	Normal stress on grain boundary
Ω	Atomic volume
j_{gb}	Grain-boundary diffusion flux
$\mathcal{D}_{gb}$	Effective grain-boundary diffusivity
D_{gb}	Grain-boundary diffusivity
δ_{gb}	Thickness of grain-boundary diffusion layer
V_{gb}	Velocity of grain boundary
C	Integration constant
κ	Principal curvature of free surface

γ_s	Surface tension
$\mathcal{D}_s$	Effective surface diffusivity
D_s	Surface diffusivity
δ_s	Thickness of surface diffusion layer
V_s	Surface migration velocity
j_s	Surface diffusion flux
κ_{tip}	Principal curvature of the triple junction
σ_{tip}	Normal stress on the triple junction
σ_∞	Applied external pressure
V_{max}	Maximum value of surface migration velocity
R	Gas constant
D_{gb0}	Pre-exponential coefficient for grain-boundary diffusivity
D_{s0}	Pre-exponential coefficient for surface diffusivity
τ_g	A characteristic time
Q_{gb}	Activation energy of grain-boundary diffusion
Q_s	Activation energy of surface diffusion
ξ	Diffusivity ratio of Grain-boundary diffusion over surface diffusion

List of Figures

List of Tables

Chapter 1 Introduction

1.1 Introduction to Sintering

Sintering is an ancient technique that is featured with its origins in the ancient civilizations of thousands of years ago. Meanwhile, sintering is also an advanced technique of producing a wide range of high-tech components and products, such as bearings, valves and pump components used in the extreme abrasive and corrosive environment. Recently, an increasing number of nano-structured materials used in cutting edge technology are manufactured by sintering. Due to its high tech added value, advanced sintering technology has aroused attention to a great extent.

Practically speaking, sintering is a process of heating material powders until particles are fully densified and adhere to each other. Theoretically speaking, sintering is a thermal treatment that bonds particles into a coherent and predominantly solid structure via mass transport events that often occur on the atomic scale. Then, the bonding leads to strength improvement and a reduction of total free energy. As the main work of this thesis is to develop computational models of sintering, only relevant basic background of sintering is introduced in the following subsection.

1.1.1 Major Phenomena in Sintering

It is common that there are three major phenomena in sintering. The first phenomenon is formation of the grain boundary (surface loss), as shown in Fig. 1.1.
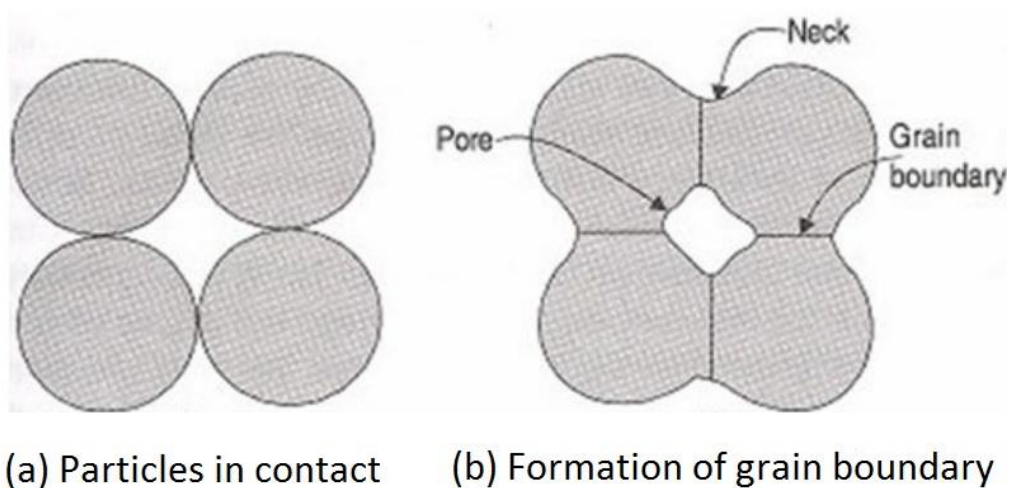
Fig. 1.1 Schematic Diagram: formation of the grain boundary

The second major phenomenon is densification from loose powder to the densified body, as shown in Fig. 1.2.
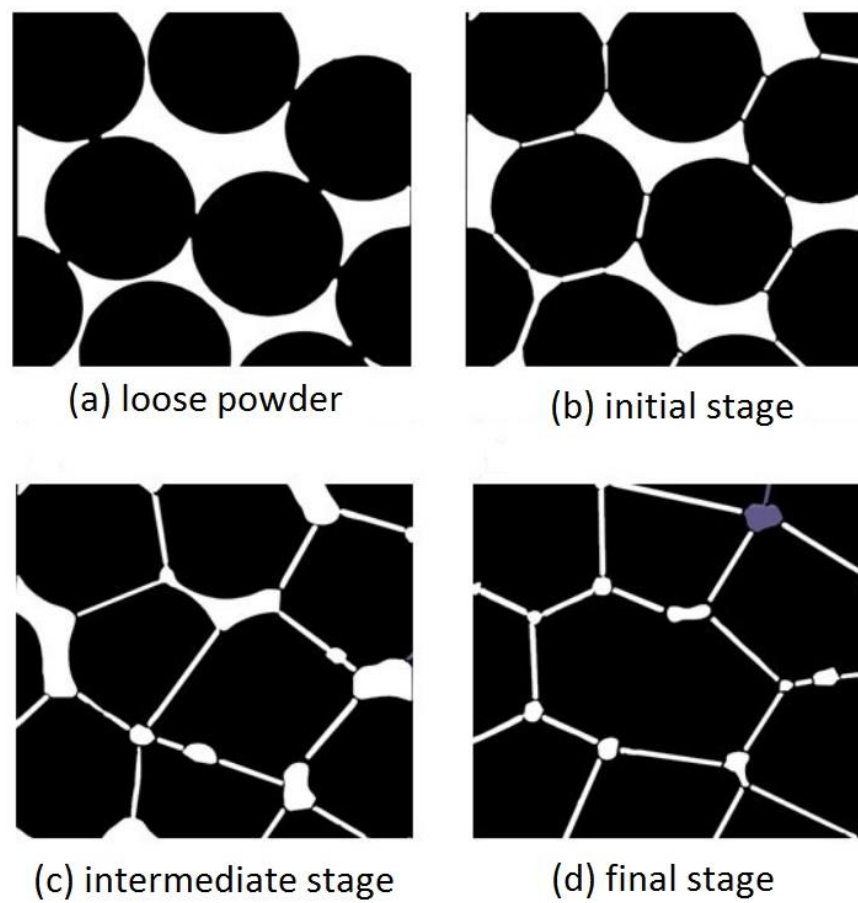
Fig. 1.2 Schematic Diagram: Densification [1]

The third phenomenon is coarsening which means big particles swallow smaller ones during sintering, as shown in Fig. 1.3.
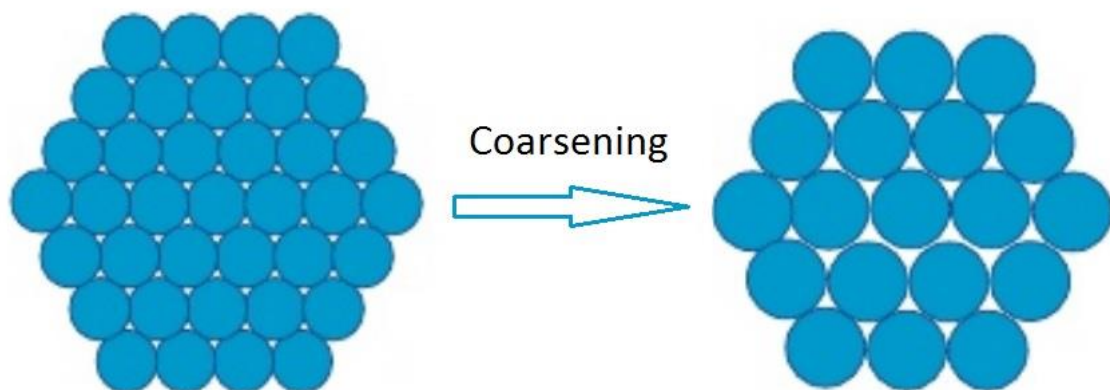
Fig. 1.3 Schematic Diagram: Coarsening [2]

1.1.2 Driving Force for Sintering

(1) Solid State Sintering

As the sintering temperature increases, two particles in contact tend to form a neck between them and bond together, as shown in Fig. 1.4. Driving force for this process, which essentially motivates sintering, is the reduction of total free energy. More specifically, the reduction of total free energy is caused by replacing the two free surfaces with a single grain-boundary in the neck region. Therefore, the general equation for the reduction of total free energy is:

$$\Delta E = -(2\gamma_{sv} - \gamma_{ss})A_c \tag{1.1}$$

where γ_{sv} represents the specific energy for the solid-vapour interface; γ_{ss} represents the specific energy for the solid-solid interface, and A_c represents the area of the contact.
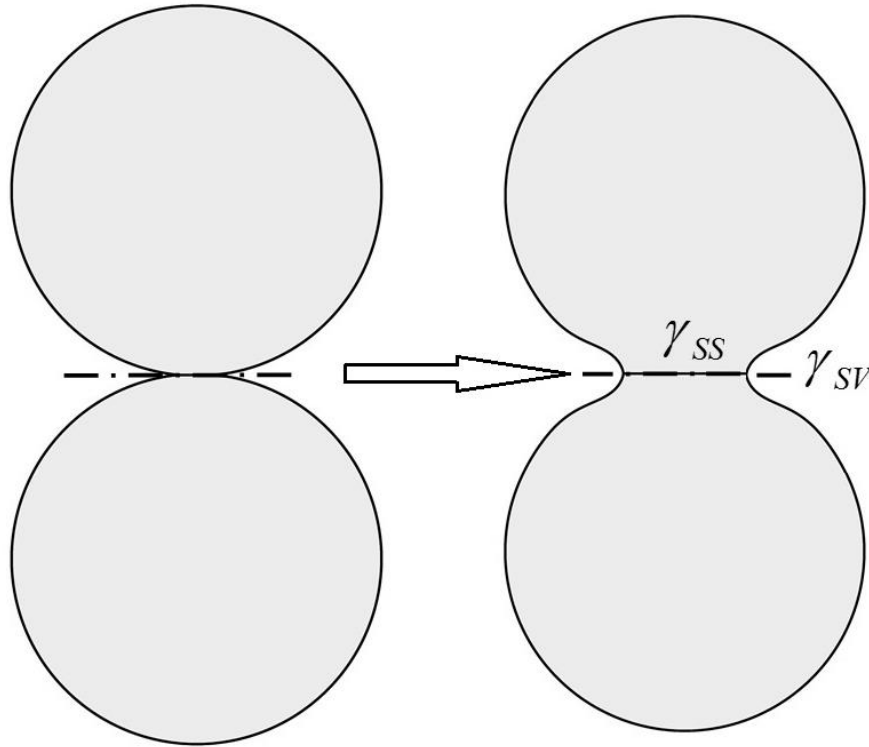
Fig. 1.4 Schematic Diagram: Sintering of Two Particles in Contact

(2) Liquid Phase Sintering

Another important mechanism is sintering in the presence of a liquid phase, as shown in Fig. 1.5. The detailed mechanism of liquid phase sintering is that aiming to sinter particles of

material A, a small amount of material B is added. As temperature rises, material B firstly melts and helps material A dissolve into B, and then forms a liquid film. The liquid film wets these two particles of material A and pulls them closer to each other. Then the neck growth is that material A dissolves into the liquid phase and then diffuses out of the contact region. The driving force for material B melting is the reduction of chemical free energy. Similarly, the driving force for neck growth is the reduction of total free energy:

$$\Delta E = -2\gamma_{LV}A_c \tag{1.2}$$

where γ_{LV} is the specific energy for the liquid-vapour interface.
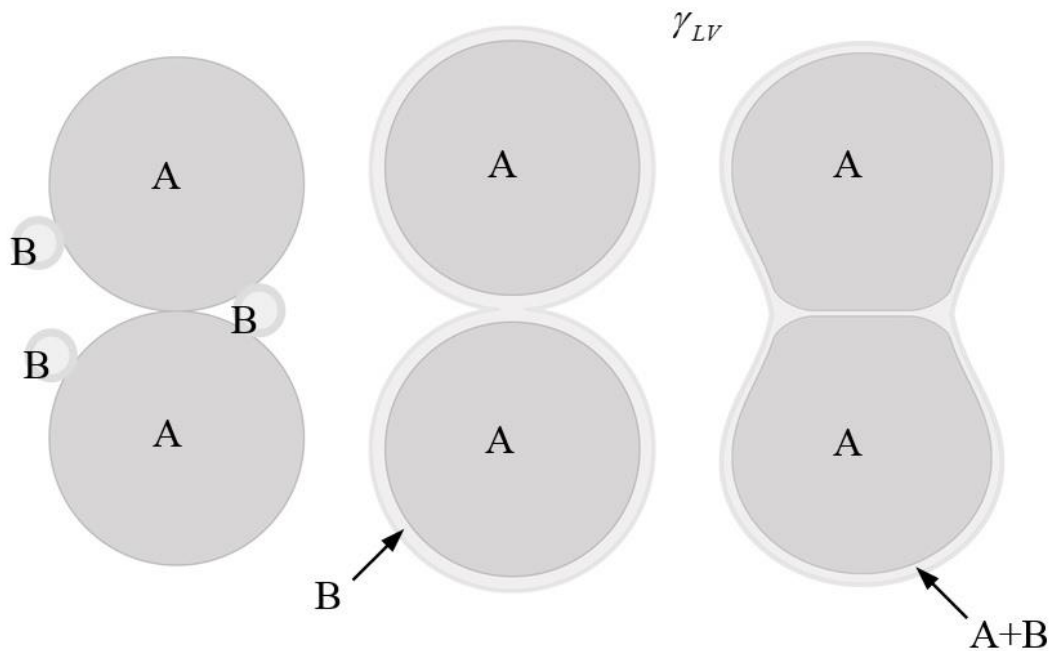
Fig. 1.5 Schematic Diagram: Liquid Phase Sintering of Two Particles

1.1.3 Classification of Sintering Mechanisms

According to the matter transport mechanism, sintering mechanisms can be classified into five categories as follows.

(1) Sintering by Grain-boundary Diffusion

The neck can be formed by matters that diffuse out of the neck and deposit them onto the particle surface, as shown in Fig. 1.6. This process contains grain-boundary diffusion j_{gb}

and surface diffusion j_s. However, if surface diffusion is faster, then grain-boundary diffusion is the rate-controlling mechanism.
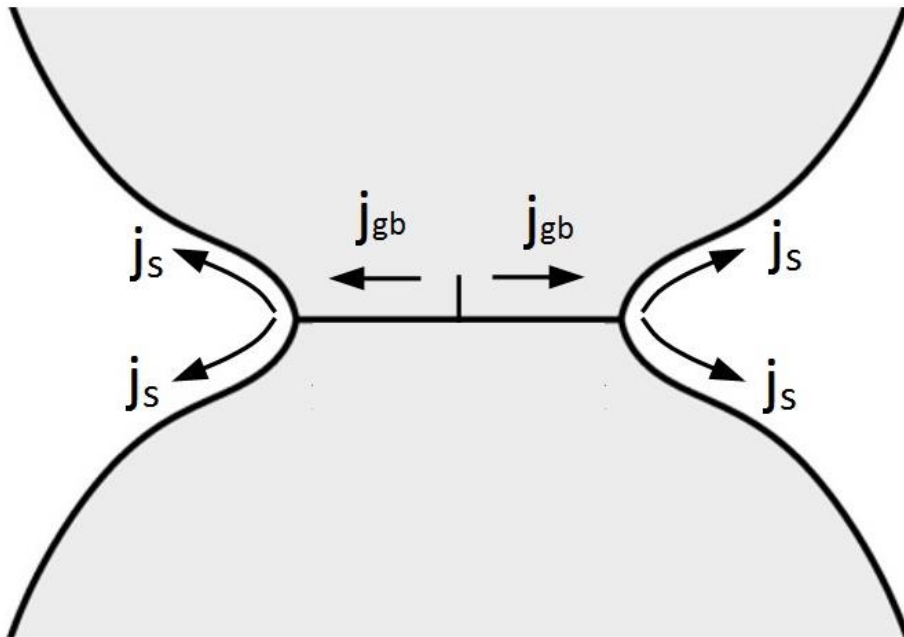
Fig. 1.6 Schematic Diagram: Sintering by Grain-boundary Diffusion

(2) Sintering by Surface Diffusion

If grain-boundary diffusion is much smaller than surface diffusion, for example sintering at relatively low temperature, the neck can be formed by matters diffusing from the particle surface onto the neck area, as shown in Fig.1.7. In this case, there is no densification in sintering, and the centres of two particles do not approach to each other.
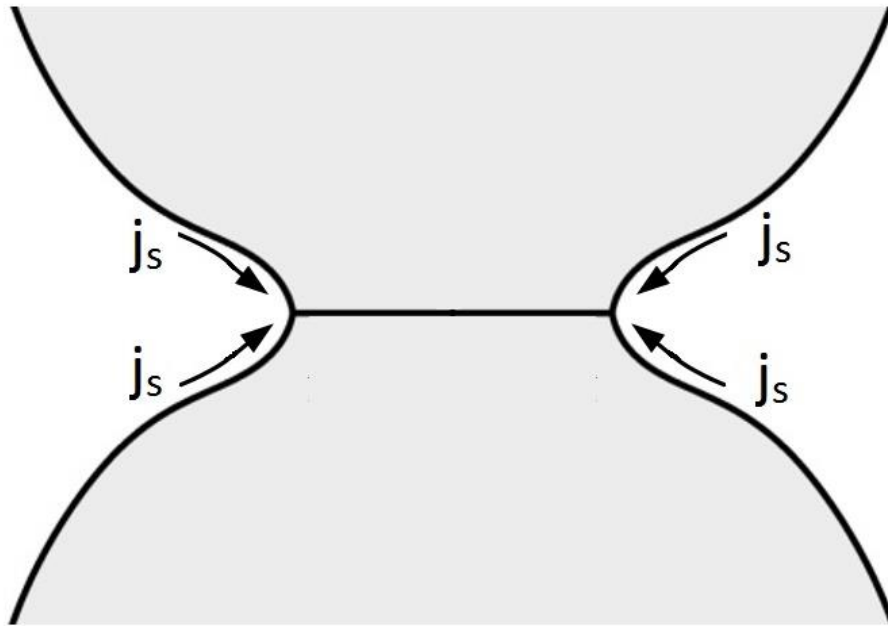
Fig. 1.7 Schematic Diagram: Sintering by Surface Diffusion

(3) Sintering by Lattice Diffusion

For large particles, the neck can grow when matter diffusing out of the grain-boundary through the particle body and depositing onto the neck surface, as shown in Fig. 1.8.
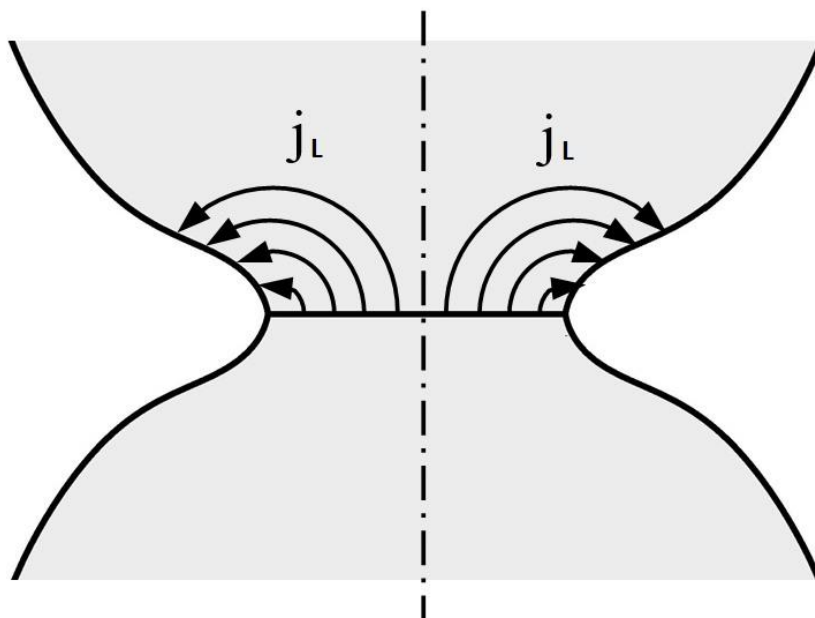
Fig. 1.8 Schematic Diagram: Sintering by Lattice Diffusion

(4) Sintering by Vapour Evaporation and Condensation

The neck can grow by atoms evaporating from the particle surface and depositing onto the neck region as shown in Fig. 1.9. Like sintering by surface diffusion, this mechanism never causes the centres of the two particles to approach to each other.
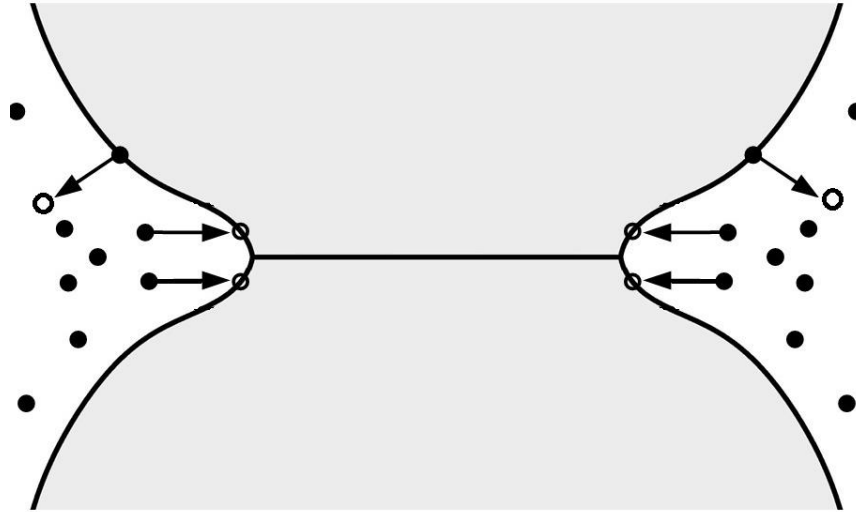
Fig. 1.9 Schematic Diagram: Sintering by Vapour Evaporation and Condensation

(5) Liquid Phase Sintering

Assuming the two particles shown in Fig. 1.10 are completely wetted by a thin film of liquid, the neck can grow when atoms dissolving into the thin liquid film between the two particles, then diffusing out of the neck through the film, and finally precipitating on Particle A.
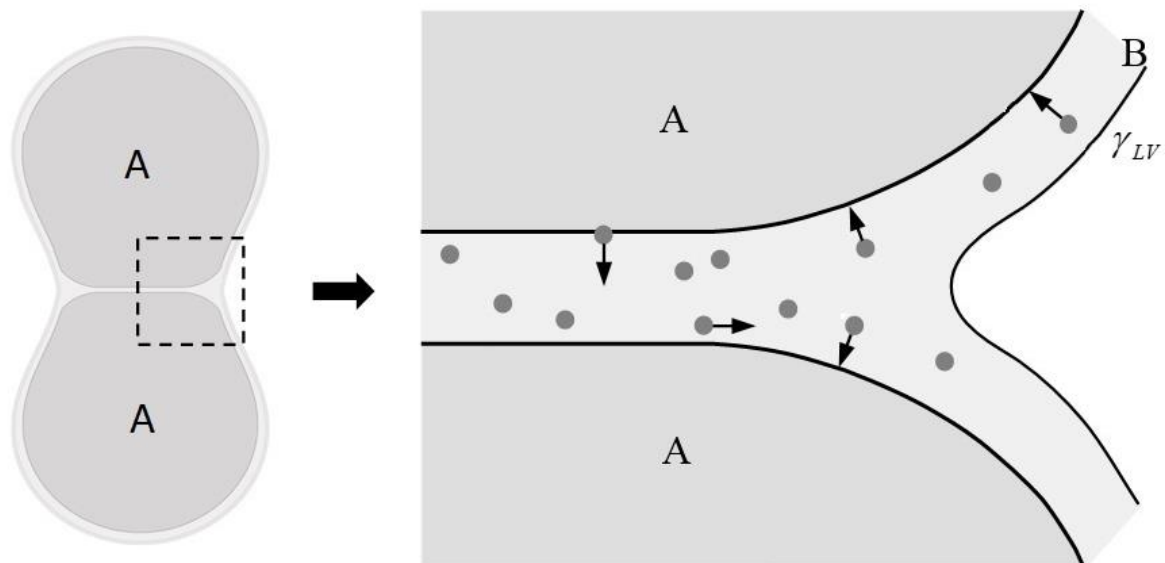
Fig. 1.10 Schematic Diagram: Liquid Phase Sintering

1.1.4 Major Sintering Variables

From an industrial point of view on sintering, the sinterability and the sintered microstructure of a powder compact are mainly determined by two categories of variables: material variables and process variables, listed in Table 1.1 [3].

Table 1.1 Major sintering variables affecting sinterability and microstructure [3]

Variables related to raw materials (material variables)	Powder: shape, size, size distribution, agglomeration, mixedness, etc.
	Chemistry: composition, impurity, homogeneity, etc.
Variables related to sintering condition (process variables)	Temperature, time, pressure, heating and cooling rate, atmosphere, etc.

1.2 Research Objectives and the Thesis Structure

1. Research Objectives

Research objectives of this thesis are studying and simulating first stage solid state sintering through computer modelling. In order to understand sintering behaviours and study the effects of sintering variables on these behaviours, several particle-scale models are developed by adopting finite difference method in this thesis. For these computational models, there are following features.

(a) They are axisymmetric models.

(b) They can simulate microstructure evolution such as grain-boundary growth and change of the particle profile.

(c) The coupled sintering mechanism of grain-boundary and surface diffusion is considered in these models.

(d) The governing equations of sintering mechanisms, such as the equation of the densification rate, are mathematically solved in these computational models.

(e) Problems of the curvature at the triple junction (pore tip) must be numerically solved rather than being estimated with a geometric way.

(f) Alumina material parameters are used for all simulations.

2. The Structure of This Thesis

In chapter 1, an overview of the thesis theme is presented, and a brief introduction to the sintering background is also given.

In chapter 2, a brief introduction to sintering modelling is presented, and a brief literature review on sintering modelling at particle scale is also given.

In chapter 3, a computational model is built to study the role of surface diffusion and external pressure on first-stage sintering where powders are densified by grain-boundary diffusion. Coupled grain-boundary and surface diffusion is considered as the mechanism for matter redistribution. There are two main achievements in this study. To be specific, the first one is providing a numerical solution to the curvature at a triple junction (pore tip), and the second one is demonstrating the effect of surface diffusion on first-stage sintering by coupled grain-boundary and surface diffusion.

In chapter 4, a computational model is built to study the role of the fast heating rate on sintering. In this study, a temperature dependent model is developed for simulating the sintering with a heating process from 600°C to 1400°C. By calculating a series of different heating rate cases, effect of the fast heating rate on sintering is revealed, and the widely observed SPS effect on densification can be partially attributed to its fast heating rate, because the rapid heating rate supports sintering to quickly pass through the low temperature domain that surface diffusion dominates, and then the blunting effect of fast surface diffusion near the triple junction is minimized.

In chapter 5, a computational model is built to qualify and quantify effects of inhomogeneity on sintering kinetics. A series of cases concerning sintering variables' inhomogeneity is computed to display their effects on sintering kinetics. Furthermore, five critical sintering variables such as the grain size, surface tension and diffusivity are chosen to study the effects of their inhomogeneity on sintering kinetics.

In chapter 6, the main achievements and conclusions of this thesis are given, and future work is also discussed.

Chapter 2 Introduction to Sintering Modelling

2.1 Introduction

In sintering study, two common ways are adopted to understand sintering behaviours and connect behaviours to sintering variables. The first one is the empirical way of measuring the sintering behaviours in the experiment under a set of controlled conditions. The second one is the theoretical way of modelling the sintering process. The theoretical analyses and experimental studies have been performed quite well over the last 60 years when providing an outstanding qualitative understanding on sintering in terms of the driving forces, the mechanisms, and the influence of major sintering variables such as the particle size, temperature and applied pressure. However, the analytical solutions of experiments are not successful enough when concerning providing a quantitative description for most sintering. Therefore, it is quite important to develop sintering modelling that can simulate and predict sintering behaviours more accurately.

For one thing, with the development of the new sintering technique as well as the increase in costs of raw material and labour, there is a strong demand for sintering modelling from the industry. From the perspective of the market, manufacturers should guarantee the performance of their products instead of providing 'typical' properties, and they have to develop robust processes to present high tolerance and net shape. In addition, with the gradually strict environmental legislations, the manufacturers should reduce their rejection rate significantly because the costs for processing the waste become extremely high. Modelling can partially solve the above issues and save the costs.

As introduced in chapter 1, the general working mechanism of sintering is as follows. For loosely compacted powder, it contains a huge number of pores, so the powder compact is brittle. With the temperature rise during sintering, material powders start adhering to each other and turn into a strong solid. Two major micro-processes namely densification (porosity reduction) and grain growth occur during sintering. Driving force for sintering is the reduction of total free energy. To be more specific, the reduction of total free energy is caused by replacing the two free surfaces with a single grain-boundary in the neck region. The external pressure applied to the powder compact gives the extra driving force that

accelerates densification during sintering. The densification process unavoidably accompanies grain growth, because the reduction in total free energy appears because of the reduction of the free surface area. Furthermore, the increase of sintering temperature leads to faster surface diffusivity, and then cause a faster sintering process. Both solid state sintering and liquid phase sintering are widely used in the industry.

Since the 1940s, a series of typical sintering models was founded by Frenkel [4], Kuczynski [5], Coble [6] and Kingery [7]. These early models tended to identify the fundamental mechanisms in sintering and laid a solid foundation for our current understanding of the sintering process. These fundamental theories are completely reviewed by German [8]. Since then, numerous models have been developed. In the 1980s, Ashby [9] collected all these models together and built their sintering mechanism maps which have been widely cited in the literature. Subsequently, the full constitutive laws were developed for the finite element analysis of sintering. The finite element analysis supports researchers to predict deformation, density and the grain size over time during an entire sintering cycle. Hence, it is an extremely powerful tool to assist development and design of products. The constitutive laws for the finite element analysis of sintering were reviewed by Cocks [10] and Olevsky [11] respectively. Besides the finite element analysis, there were another two significant developments in modelling sintering in the early 2000s. The first one is the development of the various robust numerical schemes for the computer simulation of microstructural evolution, which can be considered as the further development of the early sintering models. Cocks, Gill and Pan [12] provided a comprehensive review of a variational technique for the computer simulation. The second major development is the molecular dynamic simulation of sintering. In this type of models, the sintering process is literally simulated atom by atom on a computer. Rafii-Tabar [13] reviewed molecular dynamics which was not directed at modelling sintering but provided an excellent starting point.

2.2 A Brief Literature Review of Sintering Modelling at Particle Scale

The main purpose of this thesis is to understand sintering behaviours and study the effects of sintering variables on these behaviours through more real sintering models at particle scale. A brief literature review on the topic of sintering modelling at particle scale is presented in this section.

2.2.1 Sintering Variables

For sintering models at particle scale, there are many matured methods and classical models developed by early researchers like Frenkel [4], Kuczynski [5], Coble [6] and Kingery [7]. In addition, there are much more models developed by other authors in the subsequent studies. In general, the typical sintering variables input to these models are the particle size, the specific energies of the surface and a grain boundary, and the diffusion coefficients for the lattice, grain boundary and free surface respectively. Meanwhile, the typical sintering variables output in these models are velocity of neck growth and densification. In summary, Swinkels et al [14] and German [8] gave a complete overview on these achievements of early studies.

However, there is a common limitation in these early models based on some restricted assumptions about the geometry of particles and pores. However, in real sintering, the evolution of particles and pores is too complicated to be described mathematically. In order to derive the velocity equations, the simplified microstructure is used in these early models, but these simplifications have limited our understanding of sintering mechanisms. For example, sintering is regularly divided into three distinctive stages in early studies. To be specific, stage one is neck formation; stage two is shrinkage and stage three is coarsening, although the evolution in real sintering is continuous. For geometry assumption in early models, particles were assumed to be perfectly spherical and uniform in stage one, and particles were assumed as uniform tetrakaidecahedron grains in stage two and three. Furthermore, sintering was divided into different independent regimes, and each of these regimes is dominated by a single mechanism, although various mechanisms interact in complicated behaviours during real sintering.

With the development of computer technology, a new powerful tool called the numerical method was developed in the 1990s for computer simulation of the microstructure evolution during solid state sintering. In this new numerical simulation, the representative unit, where complete sintering mechanisms can be achieved, is simply assembled with particles of any shape and arrangement, and the scale of this representative unit can easily reach tens of thousands of particles. Inputs of this new computer simulation are the specific energy of interfaces, diffusivity, grain-boundary mobility as well as thermodynamic and kinetic properties of the material. Furthermore, external pressure applied to the powder compact can also be introduced into this new computer simulation that allows us to abandon the

limited assumptions about particle and pore geometry in classical models, and to examine the full interactions between different sintering mechanisms. In addition, a significantly typical example is shown in Fig. 2.1 [15]. Therefore, some limitations owing to over-simplifications in the early models were found in subsequent studies [16].
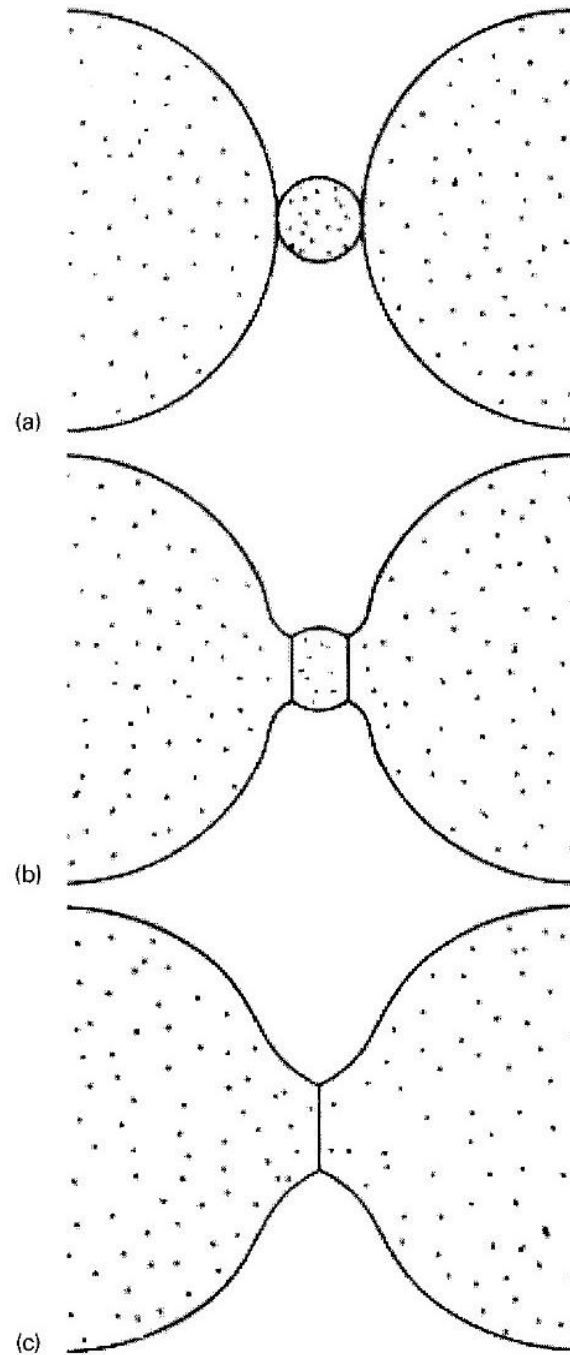
Fig. 2.1 Schematic Diagram: Computer simulation of sintering three particles: two large particles quickly grab their share of small particles between them (coupled grain growth and densification occur during sintering) [15].

2.2.2 Kinetic Laws for Solid State Sintering

There are various matter transport mechanisms leading to microstructure evolution during sintering. For solid state sintering, its main mechanisms are solid-state diffusion through different paths, power law creep, vapour evaporation and condensation, and curvature driven grain-boundary migration. The effects of these mechanisms on sintering are not the same, and they depend on the chemical composition, the particle size, sintering temperature, the external pressure and the stage of sintering.

For a numerical model, to deal with the complex microstructure and the interplay between the various mechanisms is no longer difficult. For solid state sintering, these kinetic laws have been well established in this numerical model. According to Fick's laws, the flux can be formulated in terms of the concentration gradient of diffusing species, but a more generalized form of the equations is expressed in terms of the chemical potential (the Gibbs free energy). Therefore, the diffusive flux is assumed to be linearly proportional to the gradient of the chemical potential:

$$j_i = -M_i \nabla \mu \tag{2.1}$$

where i represents the diffusion routes such as the grain boundary or the free surface, and M_i represents the relevant diffusivity strongly dependent on temperature. Herring [17] expressed the chemical potential of vacancies in terms of the principal curvature κ_s at a free surface and the normal stress σ at a grain boundary:

$$\mu = -\Omega \gamma_s \kappa_s , \qquad \text{free surface} \tag{2.2}$$

$$\mu = -\Omega \sigma , \qquad \text{grain boundary} \tag{2.3}$$

where γ_s is the specific energy of the free surface and Ω is the atomic volume. The free surface and grain-boundary diffusion are derived by substituting Eq. (2.2) and (2.3) into (2.1) respectively. For lattice diffusion, Fick's first law is often assumed to govern the vacancy diffusion inside the grains while Eq. (2.2) and (2.3) are defined as the boundary conditions for the chemical potential at the free surface and the grain boundary.

The grain growth in sintering is caused by grain-boundary migration. It is assumed that the migration velocity V_m is linearly proportional to the principal curvature κ_s of the grain boundary:

$$V_m = M_m \gamma_{gb} \kappa_{gb} \tag{2.4}$$

where M_m is the grain-boundary diffusivity which depends on temperature and γ_{gb} is the specific energy of a grain boundary.

Except for the equations mentioned above, governing equations for solid state sintering also include matter conservation, continuity of chemical potential at the interface junction, balance of interface tension at the interface junction and global force equilibrium. These conditions should be observed for numerical model development.

2.2.3 Numerical Techniques: the Finite Difference Method

Finite difference methods (FDMs) are numerical methods for solving differential equations by approximating them with difference equations, where finite differences approximate the derivatives. Perhaps Nickols and Mullins [18] were the first people to do the computer simulation of solid state sintering by adopting a finite difference method. Later, Bross and Exner [19] used this approach to study the importance of rearrangement in powders by showing angle changes in a three-particle geometry. Since then, FDMs have become a dominant approach to studying solid state sintering when an increasing number of finite difference schemes have been developed by various authors, such as Bouvard and McMeeking [20], Zhang and Schneibel [21, 22], Svoboda and Riedel [23], Zhang and Gladwell [24], and Pan [25]. These numerical studies reviewed the sintering process between two particles and significantly improved the velocity equations for neck growth and densification. However, there are still some limitations on these finite difference schemes. For example, they cannot deal with more realistic models without considering the interaction between many particles of different sizes. Furthermore, some assumptions in these numerical studies need to be validated. As computer computing capability becomes gradually powerful, many enhanced FDMs have been developed by researchers such as R. Ganeriwala, T. I. Zohdi [26, 27] and K. Shinagawa [28] in recent years. In their studies, multi-physics models were developed to simulate the more complex sintering environment.

2.2.4 Problems of Sintering Models at the Particle Level

The numerical techniques have provided a powerful tool for us to deal with real microstructure evolution and coupling issues between different mechanisms in sintering models at particle scale. However, a numerical model can perform well only if the physics

of the sintering mechanism is clear. For example, the physics of the solid-state and liquid-phase sintering model is determined by the kinetic law, and physics of viscous sintering is determined by the constitutive laws. A linear kinetic law is a common assumption in most of the existing models, but this is obviously invalid for many practical material systems and processing conditions. For example, if external pressure is applied in sintering, the relationship between the densification rate and external pressure is nonlinear, which is often observed in fine powder compacts [29]. Applying non-linear kinetic laws to the numerical techniques is not tough [30]. The real issue is to find the proper non-linear kinetic laws for numerical techniques, which can only be realised by fitting numerical simulations with experimental data.

Chapter 3 Effects of Surface Diffusion and External Pressure on First-Stage Sintering

3.1 Introduction

Surface diffusion is an important mechanism for matter redistribution. In some powder systems under certain conditions, sintering can occur along with surface diffusion alone. Kuczynski [31] considered various matter transportation mechanisms for sintering of metallic powders. However, the powder compact of most ceramics sinters results from a combination of the grain boundary and surface diffusion. In this sintering mechanism, grain-boundary diffusion at the particle contact is responsible for densification. The role of surface diffusion is however rather complex. It is often argued that surface diffusion is much faster than grain-boundary diffusion, and hence materials delivered by grain-boundary diffusion to the contact neck can be quickly redistributed onto the pore surface by surface diffusion. It follows that grain-boundary diffusion is the rate limiting process. Many analytical models for sintering from the classical model by Coble [32] to modern constitutive laws [33, 34], rely on this assumption of fast surface diffusion. As this assumption is valid for the later stage of sintering when pores are isolated, it has been generally recognised that surface diffusion plays an important role in the first stage of sintering when the contact between particles is isolated. Earlier works on this topic include those conducted by Nichols and Mullins [35], German and Lathrop [36], Bross and Exner [37] and Exner [38]. In particular, the simulation results of Exner [37] showed that surface redistribution from the grain boundary would limit grain-boundary diffusion only for high grain-boundary diffusivity.

Svoboda and Riedel [39] developed an analytical treatment for surface diffusion to model its effect on sintering behaviours. In their study, a two-dimension model for the sintering of row configuration is developed, and a numerical solution is derived to describe the whole process from initial neck formation to the later stage when the pore shape is in equilibrium or near equilibrium and finally disappears. Meanwhile, the analytical solutions of initial neck formation and the later sintering stage are derived respectively by a thermodynamic principle. J. Svoboda and H. Riedel found that the reduction of surface diffusivity has a double-fold effect on sintering behaviours during the later sintering stage. Furthermore, the ratio of surface diffusivity to grain-boundary diffusivity is considered, and the analytical

estimate based on the equilibrium pore shape can describe the effect of surface diffusivity quite well.

Bouvard and McMeeking [20] provided an analytical contact law between particles by fitting their numerical results of computer simulation concerning sintering by coupled surface and grain-boundary diffusion. Bouvard and McMeeking demonstrated that fast surface diffusion accelerates neck growth and retards shrinkage.

One technical issue for modelling the coupled surface and grain-boundary diffusion is how to calculate the curvature at the triple junction between the grain-boundary and particle surfaces, because the triple junction always keeps sharp throughout sintering, and it is especially sharper in the early sintering stage. D. Bouvard et al [20] proposed a simple estimation formula for the curvature at the triple junction, and it can be restrictedly applied for the computation combining small pressure assisted sintering and free sintering. With the development of sintering techniques, extremely high pressure can be applied during sintering, such as Spark Plasma Sintering (SPS). Therefore, the significance for numerically solving the curvature at the triple junction becomes more important. The curvature is required for both calculating surface diffusion flux and completing the solution to grain-boundary diffusion. It however does not exist mathematically because of tangential discontinuity of the free surface at the junction. Pan and Cocks [40] resolved the issue by showing that it is possible to find the expression for the chemical potential at the triple junction which should be used in the calculation instead of the curvature.

Zhang and Gladwell [41] studied the effect of surface diffusion on sintering of particles in different sizes, and found that careful treatment of the triple junction is significant when modelling the sintering process.

Despite all the existing understandings about the important role of surface diffusion, the effect of surface diffusivity is often ignored in sintering models, particularly in many studies on first-stage sintering using the discrete element method. This is mainly due to two reasons. Firstly, the problem of surface diffusion has to be solved numerically in general. It is difficult to build the numerical solution into a sintering model for the powder compact made of millions of three-dimensional particles. The assumption of fast surface diffusion simplifies the modelling effort considerably. However, recent development of combining sintering models at continuum and particle levels [42] has made it possible to take into account of surface diffusion fully in finite element analysis of sintering at the component

scale. Secondly, the assumption seems plausible. Although the effect of surface diffusion was well understood by many previous researchers, it was buried in analytical expressions and numerical details. A simple demonstration, particularly related to experimental data, on the effect of surface diffusion in densification dominated by grain-boundary diffusion is missing.

Purposes of This Chapter

The purposes of this chapter are to (a) present a simple and definitive case for invalidity of the assumption of fast surface diffusion for first-stage sintering where densification is achieved by grain-boundary diffusion, (b) provide a straightforward understanding of the reason why fast surface diffusion retards densification under such conditions and (c) show the effect of external pressure on sintering. The co-sintering problem of two spherical particles is revisited using the numerical method developed by Pan and Cocks [33]. One tool used in this demonstration is to examine the relative relation between the shrinkage and neck growth as sintering proceeds. A small ratio of shrinkage over neck growth indicates that the sintering process is detrimental to densification. The ratio is zero if grain-boundary diffusion is completely prohibited. Besides, a large ratio indicates that the sintering process favours densification. Another tool of demonstrating the effect of surface diffusion is to examine the direction of the surface diffusion flux in the vicinity of the triple junction between grain-boundary and particle surfaces. If the flux is away from the junction region, then surface diffusion supports densification by moving atoms away and depositing them onto pore surfaces. If the flux is toward the junction region, then surface diffusion is harming the densification by moving atoms from the particle surfaces onto the junction region and reducing the driving force for further densification. These tools were available to all previous researchers who have developed numerical models that have not been used to make the case for the effect of surface diffusion as far as we are aware.

3.2 Methodology

3.2.1 Assumption of Geometry and Sintering Variables

Two identical and spherical particles are considered as shown in Fig. 3.1(a) which shows sinter by coupled surface and grain-boundary diffusion. In the figure, R_0 represents the

initial radius of two particles; 2a is the neck diameter; γ_s is the surface tension; γ_{gb} is the grain-boundary tension and θ is the dihedral angle at the triple junction. A cylindrical coordinate (r, z) is used. The grain boundary is assumed as the straight and neck grow along a grain boundary. Additionally, a lower particle is fixed, while the upper particle is free to move with a velocity V_{gb}.
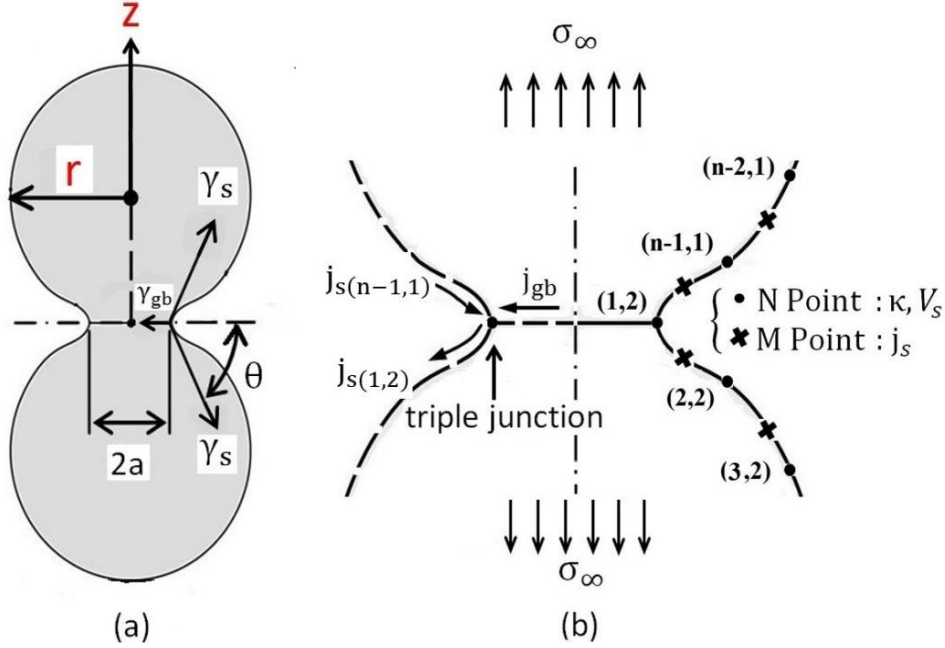
Fig. 3.1 The sintering model used in this study (a) geometry overview and (b) local details of the contact neck

3.2.2 Governing Equations and Their Numerical Solutions

According to Fick's laws, the diffusive flux j is linearly dependent on the gradient of chemical potential μ of the diffusion atoms:

$$j = -\frac{D\delta}{kT}\frac{\partial \mu}{\partial s} \tag{3.1}$$

where D is diffusivity; δ is the thickness of the diffusion layer; k is Boltzmann's constant; T is the sintering temperature and s is the local coordinate along the diffusion path.

3.2.2.1 Grain-boundary Diffusion

On the grain boundary, the chemical potential is related to the stress σ normal to the grain boundary through

$$\mu = -\Omega\sigma \tag{3.2}$$

where Ω is the atomic volume. Substituting Eq. (3.2) into Eq. (3.1) leads to

$$j_{gb} = \mathcal{D}_{gb}\frac{\partial\sigma}{\partial r} \tag{3.3}$$

in which an effective grain-boundary diffusivity has been introduced as

$$\mathcal{D}_{gb} = \frac{D_{gb}\delta_{gb}\Omega}{kT} \tag{3.4}$$

where D_{gb} is grain-boundary diffusivity and δ_{gb} is the thickness of the grain-boundary diffusion layer.

As shown in Fig. 3.2, grain-boundary diffusion j_{gb} flows through the grey ring and then becomes $j_{gb}{}'$. Consequently, this process leads to a vertical speed $-V_{gb}$ of the grain boundary. Defining the grey ring as a unit, to satisfy mass conservation at neck 1, there is

$$-V_{gb} * 2\pi r * \Delta r = j'_{gb} * [2\pi(r + \Delta r)] - j_{gb} * 2\pi r \tag{3.5}$$

When $\Delta r \to 0$, there is

$$-V_{gb} = \frac{\partial j_{gb}}{\partial r} + \frac{j_{gb}}{r} \tag{3.6}$$

According to the product rule, there is

$$-V_{gb} = \frac{1}{r} * \frac{\partial(rj_{gb})}{\partial r} \tag{3.7}$$

An approximate solution can be proposed as follows.

$$\hat{j}_{gb} = Ar + B \implies r * \hat{j}_{gb} = Ar^2 + Br \implies \frac{\partial(r\hat{j}_{gb})}{\partial r} = 2Ar + B \tag{3.8}$$

When r=0, $\hat{j}_{gb} = 0$, the value of B is easily deduced, and it equals to 0. Hence,

$$\left.\begin{matrix}\hat{j}_{gb}=Ar\\ \frac{\partial(r\hat{j}_{gb})}{\partial r}=2Ar\end{matrix}\right\} \implies \frac{\partial(r\hat{j}_{gb})}{\partial r} = 2\hat{j}_{gb} \tag{3.9}$$

When substituting Eq. (3.9) into Eq. (3.7), the expression for the grain-boundary flux j_{gb} can be obtained as

$$j_{gb} = -\frac{1}{2}V_{gb} * r \tag{3.10}$$

When substituting Eq. (3.10) into Eq. (3.3), after integration, normal stress σ at the neck can be found as

$$\sigma = -\frac{1}{4\mathcal{D}_{gb}}V_{gb}r^2 + C \tag{3.11}$$

where C is an integration constant to be determined.
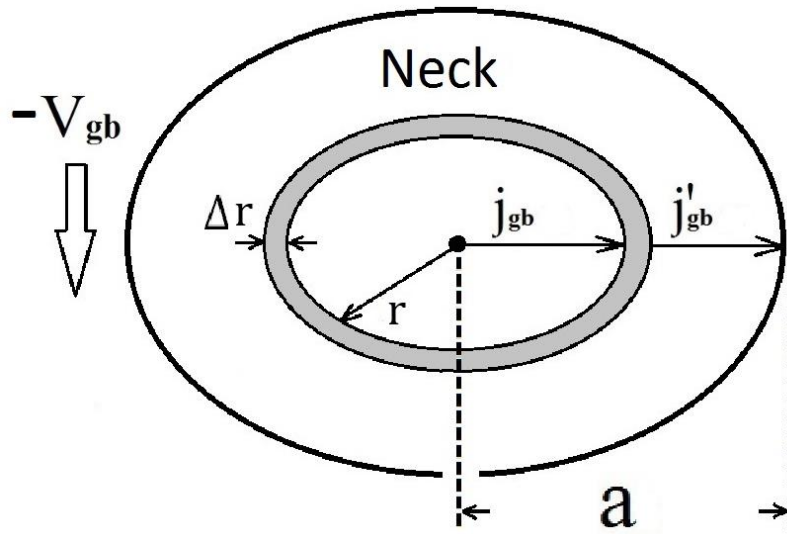
Fig. 3.2 Schematic diagram for mass conservation at the neck

3.2.2.2 Surface Diffusion

On the particle surface, the chemical potential is related to the principal curvature κ :

$$\mu = -\Omega\gamma_s\kappa \tag{3.12}$$

where γ_s is the surface tension; κ is the principal curvature of the free surface. Substituting Eq. (3.12) into Eq. (3.1) leads to

$$j_s = \mathcal{D}_s\frac{\partial\kappa}{\partial s} \tag{3.13}$$

in which the effective surface diffusivity has been introduced as

$$\mathcal{D}_s = \frac{D_s\delta_s\Omega\gamma_s}{kT} \tag{3.14}$$

where D_s is surface diffusivity and δ_s is the thickness of the diffusion layer.

To derive the expression for surface migration velocity V_s with the finite difference method, the geometry of this model is meshed as Fig. 3.1(b). In the figure, the profile of two particles is composed of many discrete nodes (N point), and then κ and V_s are defined on the N point. Furthermore, the M point is used for bisecting two neighbouring N points, and then j_s is defined on the M point.

In this discrete-node system, according to Eq. (3.13), the surface diffusive flux at any M point is obtained as

$$j_{s(i)} = \mathcal{D}_s \frac{\kappa_{(i+1)} - \kappa_i}{\Delta S_i} \tag{3.15}$$

where κ_i is the principal curvature and ΔS_i is the distance between two neighbouring M points. Apart from the triple junction, the principal curvature at the N point is defined as the sum of the maximum curvature and the minimum curvature, and it is negative for the convex surface.

In addition, mass conservation provides a relation between the surface migration velocity V_s and the surface diffusion flux j_s, as shown in Fig. 3.3. To satisfy mass conservation at the shadow area, there is

$$j_{s(i)} * 2\pi r_{(i)} - j_{s(i-1)} * 2\pi r_{(i-1)} = V_{s(i)} * A_s \tag{3.16}$$

where A_s is the shadow area.

Finally, there is

$$V_{s(i)} = \frac{2\pi * (j_{s(i)} * r_{(i)} - j_{s(i-1)} * r_{(i-1)})}{A_s} \tag{3.17}$$

Except for the triple junction, the surface diffusion flux j_s and the surface migration velocity V_s can be calculated with Eq. (3.15) and Eq. (3.17) respectively.
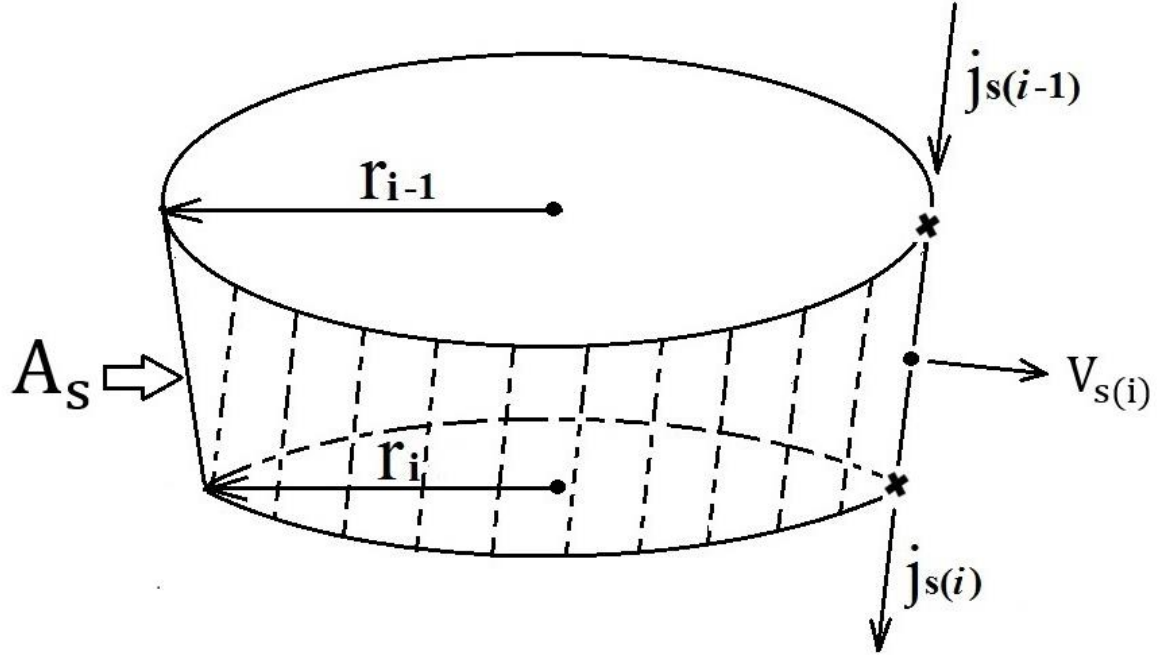
Fig. 3.3 Schematic diagram for mass conservation on the free surface

3.2.2.3 Continuity Conditions at the Triple Junction

(1) Mass conservation is satisfied at the junction.

As shown in Fig. 3.1(b), at the triple junction, mass conservation requires

$$j_{gb} = j_{s(1,2)} - j_{s(n-1,1)} \tag{3.18}$$

(2) The chemical potential is continuous at the junction.

The chemical potential must be continuous at the junction. If not, there would be an unbounded flux at the junction. Then there is

$$\mu = -\Omega\, \sigma_{tip} = -\Omega\gamma_s\kappa_{tip} \qquad \Rightarrow \qquad \sigma_{tip} = \gamma_s\kappa_{tip} \tag{3.19}$$

(3) There is equilibrium of surface tension γ_s and grain-boundary tension γ_{gb} at the triple junction.

As shown in Fig. 3.1(a), surface tension γ_s and grain-boundary tension γ_{gb} must be in equilibrium at the junction. Then there is

$$\cos\theta = \frac{\gamma_{gb}}{2\gamma_s} \tag{3.20}$$

31

3.2.2.4 Global Equilibrium of Forces

When drawing the free body diagram of the upper particle, force analysis is illustrated in Fig. 3.4. The expression of force balance is as follows.

$$\sigma_\infty \pi a^2 - 2\pi a \gamma_s \sin\theta - \int_0^a (\sigma) 2\pi r dr = 0 \tag{3.21}$$

When substituting Eq. (3.11) into Eq. (3.21), there is

$$\sigma_\infty \pi a^2 - 2\pi a \gamma_s \sin\theta + \frac{1}{8\mathcal{D}_{gb}} V_{gb} a^4 - Ca^2 = 0 \tag{3.22}$$

For the triple junction, $r = a$, and when substituting $r = a$ into Eq. (3.11), there is

$$\sigma = -\frac{1}{4\mathcal{D}_{gb}} V_{gb} a^2 + C \tag{3.23}$$

At the triple junction, $\sigma = \sigma_{tip}$. When substituting Eq. (3.19) and Eq. (3.23) into $\sigma = \sigma_{tip}$, there is

$$C = \gamma_s \kappa_{tip} + \frac{1}{4\mathcal{D}_{gb}} V_{gb} a^2 \tag{3.24}$$

When substituting Eq. (3.24) into Eq. (3.22), the equation of the shrinkage rate is obtained.

$$V_{gb} = 8\mathcal{D}_{gb} \left(\frac{\sigma_\infty}{a^2} - \frac{2\gamma_s \sin\theta}{a^3} - \frac{\gamma_s \kappa_{tip}}{a^2} \right) \tag{3.25}$$

In case of free sintering, no external pressure is applied during sintering, and the first item in brackets in Eq. (3.25) is equal to zero. From Eq. (3.25), the inside mechanism of the shrinkage rate is obvious. The shrinkage rate is under the combined effect of external pressure, free surface tension and chemical potential of the free surface at the pore tip. The external pressure σ_∞ accelerates the densification rate. Similarly, the surface tension γ_s always has a positive effect on shrinkage, which explains why the powder compact can be densified in free sintering. However, the effect of the curvature at the triple junction κ_{tip} should be further studied.
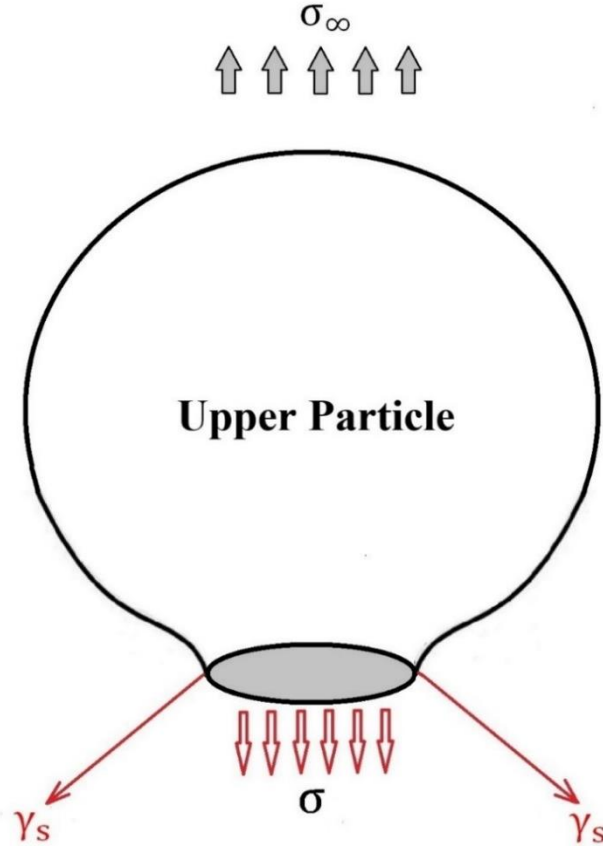
Fig. 3.4 The free body diagram of the upper particle

3.2.2.5 Completing Governing Equations and Solving κ_{tip}

For the triple junction, $r = a$. When substituting Eq. (3.10) and Eq. (3.15) into Eq. (3.18), there is

$$V_{gb} = \frac{2\mathcal{D}_s}{a_1} \left\{ \left[\frac{\kappa_{tip}}{\Delta S_{(n-1,1)}} + \frac{\kappa_{tip}}{\Delta S_{(1,2)}} \right] - \left[\frac{\kappa_{(n-1,1)}}{\Delta S_{(n-1,1)}} + \frac{\kappa_{(2,2)}}{\Delta S_{(1,2)}} \right] \right\} \tag{3.26}$$

When substituting Eq. (3.25) into Eq. (3.26), the curvature of the triple junction κ_{tip} is solved as

$$\kappa_{tip} = \frac{4\mathcal{D}_{gb}\left(\frac{\sigma_\infty}{a} - \frac{2\gamma_s \sin\theta}{a^2} \right) + \mathcal{D}_s\left(\frac{\kappa_{(2,2)}}{\Delta S_{(1,2)}} + \frac{\kappa_{(N-1,1)}}{\Delta S_{(N-1,1)}} \right)}{\frac{4\mathcal{D}_{gb}\gamma_s}{a} + \frac{\mathcal{D}_s}{\Delta S_{(N-1,1)}} + \frac{\mathcal{D}_s}{\Delta S_{(1,2)}}} \tag{3.27}$$

From Eq. (3.27), it can be observed that κ_{tip} depends on diffusivity, external stress, surface tension, the dihedral angle and local-area curvature. Furthermore, the expression of κ_{tip} is

no longer the traditional definition of curvature. It is more like a combination of all sintering variables acting at the triple junction. Therefore, it cannot be the curvature that could be uniquely determined from the local geometry of the free surface at the triple junction. If $\mathcal{D}_s \gg \mathcal{D}_{gb}$, Eq. (3.27) is reduced to $\kappa_{tip} = \kappa_1$. However, if $\mathcal{D}_{gb}$ is comparable to $\mathcal{D}_s$, then the effect of σ_∞ and γ_s cannot be ignored.

3.2.3 Update of the Particle Profile

In this model, the lower particle is fixed, and therefore its profile is only updated by the surface migration velocity V_s. Euler's method is used to describe the time step integration of the particle profile. Hence, new cylindrical coordinates (r, z) of the lower particle are expressed as follows.

$$r_{(t+\Delta t)} = r_t + V_S * n_r \Delta t$$

$$Z_{(t+\Delta t)} = Z_t + V_S * n_z \Delta t \qquad (3.28)$$

And

$$\Delta t = \frac{\Delta S_m}{V_{max}} \qquad (3.29)$$

where Δt is the time step; ΔS_m is the average of the distance between two nodes and V_{max} is the maximum value of V_s.

For the upper particle, its profile is not only updated by the surface migration velocity V_s but also by the densification rate V_{gb}, because the upper particle is free to move. Therefore, new cylindrical coordinates (r, z) of the upper particle are expressed as follows.

$$r_{(t+\Delta t)} = r_t + V_S * n_r \Delta t$$

$$Z_{(t+\Delta t)} = Z_t + V_S * n_z \Delta t + V_{gb} * \Delta t \qquad (3.30)$$

And

$$\Delta t = \frac{\Delta S_m}{V_{max}} \qquad (3.31)$$

where Δt is the time step; ΔS_m is the average of the distance between two nodes and V_{max} is the maximum value of V_s.

3.2.4 A Brief Introduction to Application of Commercial Software in This Chapter

In order to run the above mathematical model, Fortran (Formula Translation) is selected as programming language, because it is one of the most common languages in scientific computation. Then Windows Visual Studio 2010 and Intel Visual Fortran Compiler 11 are selected for programming and running model computation. Detailed steps of using the software are as follows.

Step 1: Open "Windows Visual Studio", the operation interface is shown as Fig. 3.5.
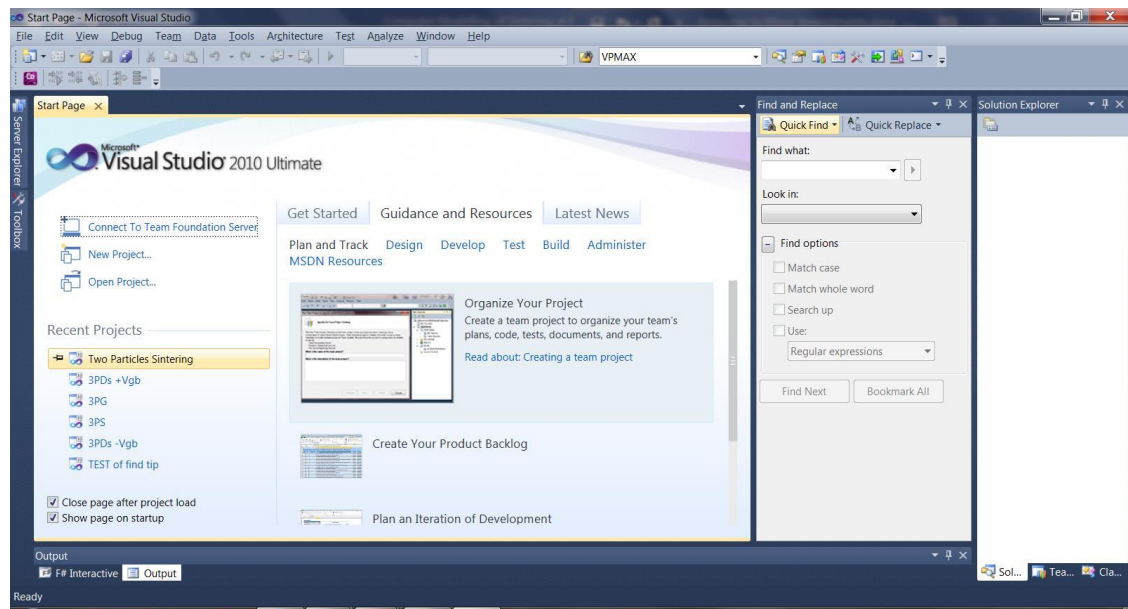
Fig. 3.5 The operation interface of "Windows Visual Studio"

Step 2: Click "File → New → Project" in upper left corner, pop-up dialog box is shown as Fig. 3.6. In this dialog box, choose "Intel(R) Visual Fortran → Empty Project".
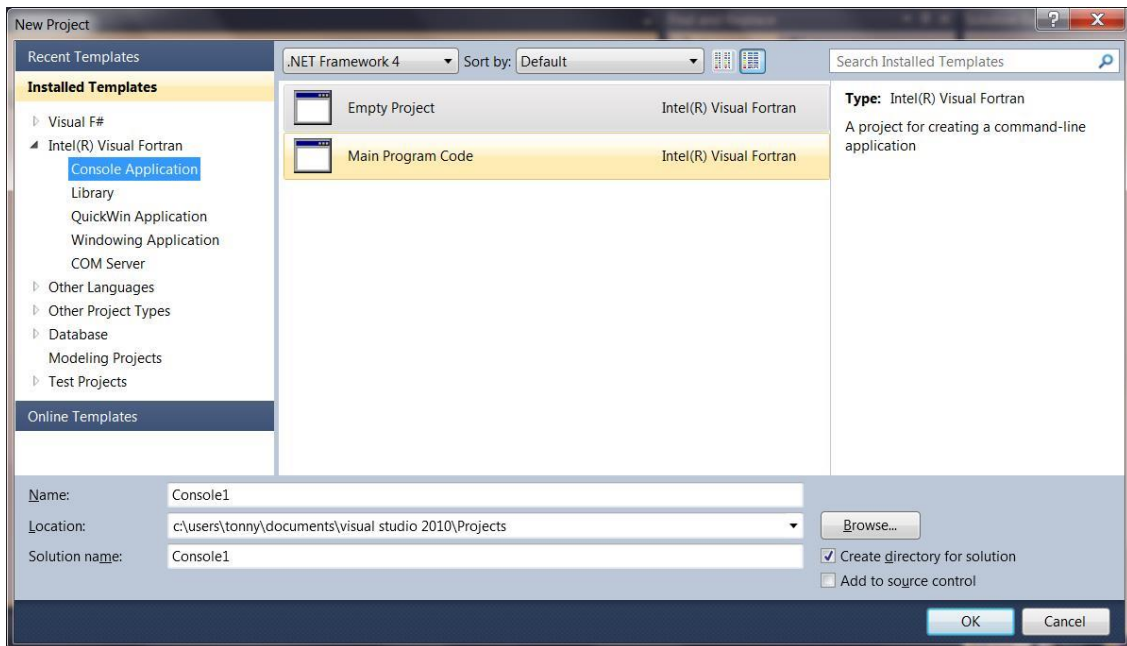
Fig. 3.6 Dialog box of choosing language compiler

Step 3: Then right click to add "New item" in "Source File of Solution Explorer" on right side, a dialog box will pop up and ask the form of Fortran code, as shown in Fig. 3.7. Choose "Fortran Free-form File (. f90)" in this dialog box.
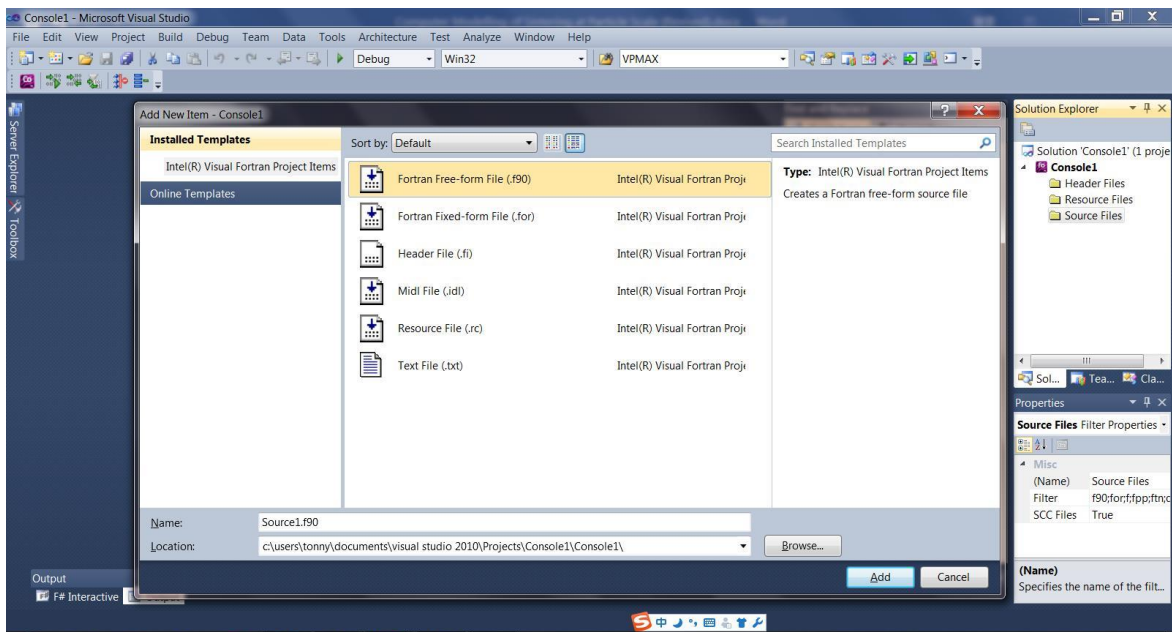
Fig. 3.7 Dialog box of choosing the form of Fortran code

Step 4: Then an empty dialog box will pop-up, and programme Fortran code in this dialog, as shown in Fig. 3.8.
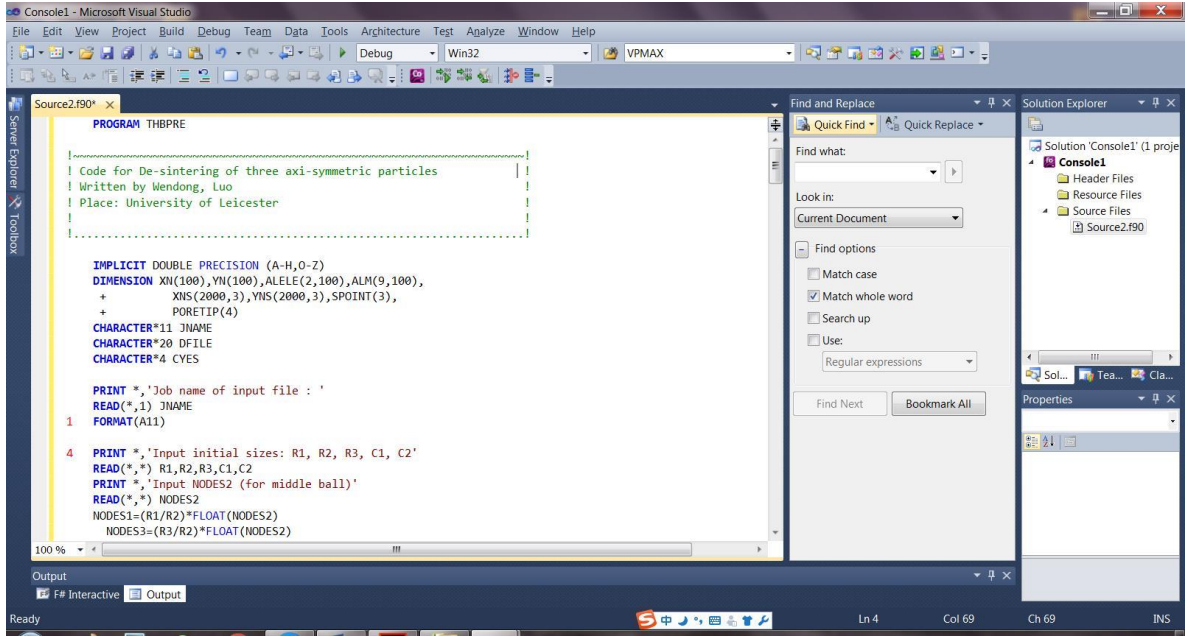
Fig. 3.8 Dialog box of programming Fortran code

Step 5: When finish programming the code, just press "F5" button, then it will start debugging.

Finally, the source code used to compute the model of Chapter three is in the CD, which is submitted with this thesis.

3.3 Effects of Surface Diffusion and External Pressure on Sintering

To simulate the real sintering, material parameters of alumina are selected in this numerical study. Table 3.1 presents the material data which are loosely based on micron-sized alumina powders [43].

Furthermore, both $\mathcal{D}_{gb}$ and $\mathcal{D}_s$ depend on temperature, so

$$\mathcal{D}_{gb} = \frac{\Omega(D_{gb0}\delta_{gb})\exp(-Q_{gb}/RT)}{kT} \tag{3.32}$$

and

$$\mathcal{D}_s = \frac{\Omega\gamma_s(D_{s0}\delta_s)\exp(-Q_s/RT)}{kT} \tag{3.33}$$

in which D_{gb0} and D_{s0} are the pre-exponential coefficients for the grain-boundary and surface diffusivity respectively; Q_{gb} and Q_s are the activation energy of the grain boundary and surface diffusion respectively and R is the gas constant. In this study, the thickness of the surface diffusion layer δ_s is taken as $\sqrt[3]{\Omega}$.

Table 3.1 Alumina Material Data Used in the Numerical Study [43]

Atomic volume $\mathbf{\Omega}$	8.47×10^{-30} m^3
Specific surface energy $\mathbf{\gamma_s}$	1.1 J/m^2
Specific grain-boundary energy $\mathbf{\gamma_{gb}}$	1.21 J/m^2
Grain-boundary thickness × pre-exponential grain-boundary diffusion coefficient $\mathbf{\delta_{gb}D_{gb0}}$	1.02×10^{-7} m^{3}s^{-1}
Activation energy for grain-boundary diffusion $\mathbf{Q_{gb}}$	5.3×10^5 J/mol
Gas constant $\mathbf{R}$	8.3144621 J/(mol K)
Boltzmann's constant $\mathbf{k}$	1.3806503×10^{-23} m^{2}kg/(s^{2}K)
Dihedral angle $\mathbf{\theta}$	$130°$
Initial particle radius $\mathbf{R_0}$	10^{-6}m

The isothermal sintering temperature is selected as $1200°$C. Using the data in Table 3.1 and the sintering temperature, Eq. (3.32) gives $\mathcal{D}_{gb} = 6.8531648\times10^{-36}$ m^{4}s/kg. The effective surface diffusivity $\mathcal{D}_s$ was varied 5 times to 10000 times of $\mathcal{D}_{gb}$ to explore the effect of surface diffusion. When presenting the results, the time is normalised by the characteristic time defined as $\tau_g = kTR^4/\delta_g D_g \Omega \gamma_s$ [20], which is the time for the neck to reach R$_0$ by grain-boundary diffusion [44]. All the simulations started from a small initial neck radius of a/R$_0$ = 0.01. In addition, a series of pressure-assisted sintering cases is also computed to reveal the effect of external pressure.

A series of numerical computation cases in this chapter is listed as Table 3.2.

Table 3.2 Numerical Computation Cases with Different $\mathcal{D}_s/\mathcal{D}_{gb}$ and σ_∞

$\mathcal{D}_s/\mathcal{D}_{gb}$ \\ σ_∞	0 MPa	-25 MPa	-50 MPa	-75 MPa	-100 MPa
5	√	√	√	√	√
50	√	√	√	√	√
100	√	√	√	√	√
1000	√	√	√	√	√
10000	√	√	√	√	√

3.3.1 Validation by Comparing with Results of Coblenz and Bouvard

At the beginning, validation of this model is carried out by comparing with analytical prediction of Coblenz et al [45] and numerical results of Bouvard et al [20], where sintering variables are $\mathcal{D}_s/\mathcal{D}_{gb} = 5$, $\theta = 130°$ and $\sigma_\infty = 0$.

Fig. 3.9 shows neck growth over time. In this figure, the overall trend of numerical results in this model fits those of Coblenz and Bouvard reasonably well. In particular, numerical results of this model are in good agreement with those of Bouvard.

Fig. 3.10 shows shrinkage over time. In this figure, numerical results of this model and those of Coblenz are somewhat different due to the error on estimating κ_{tip}, while the numerical results fit those of Bouvard quite well because of a simple estimation formula for κ_{tip} used in Bouvard's model.
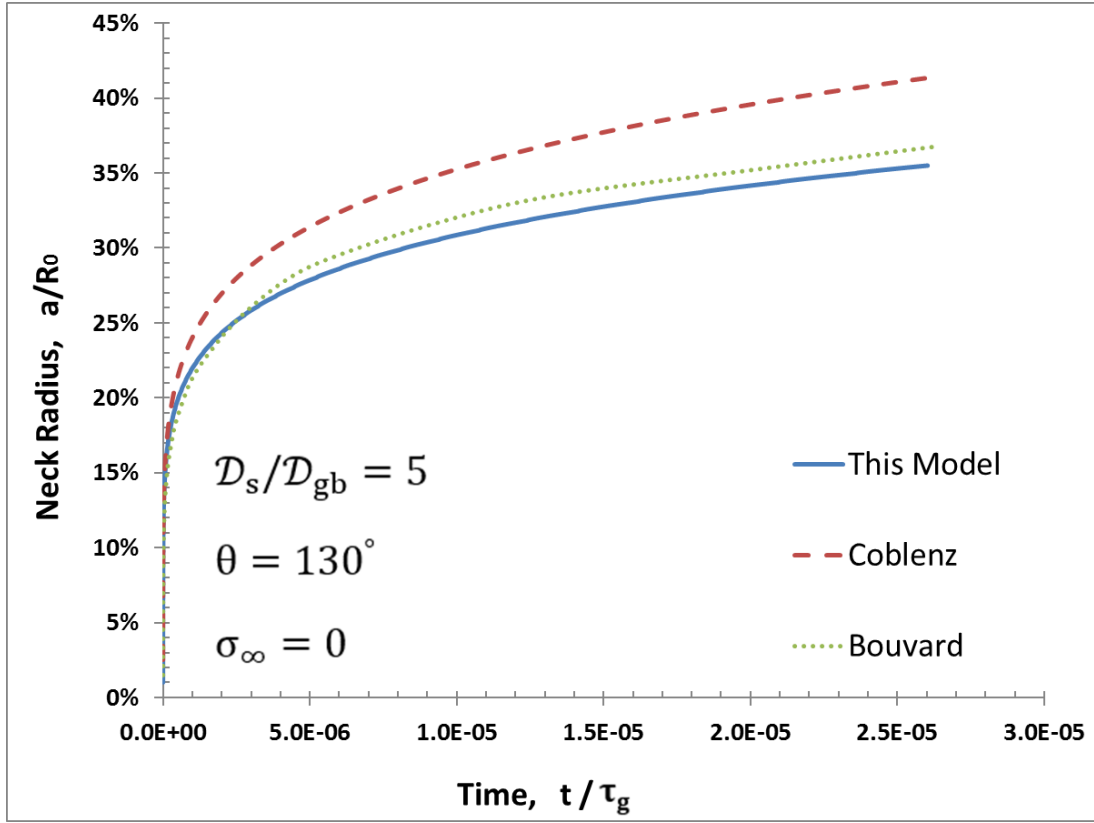
Fig. 3.9 Comparison of neck growth for $\mathcal{D}_s/\mathcal{D}_{gb} = 5$, $\theta = 130°$ and $\sigma_\infty = 0$
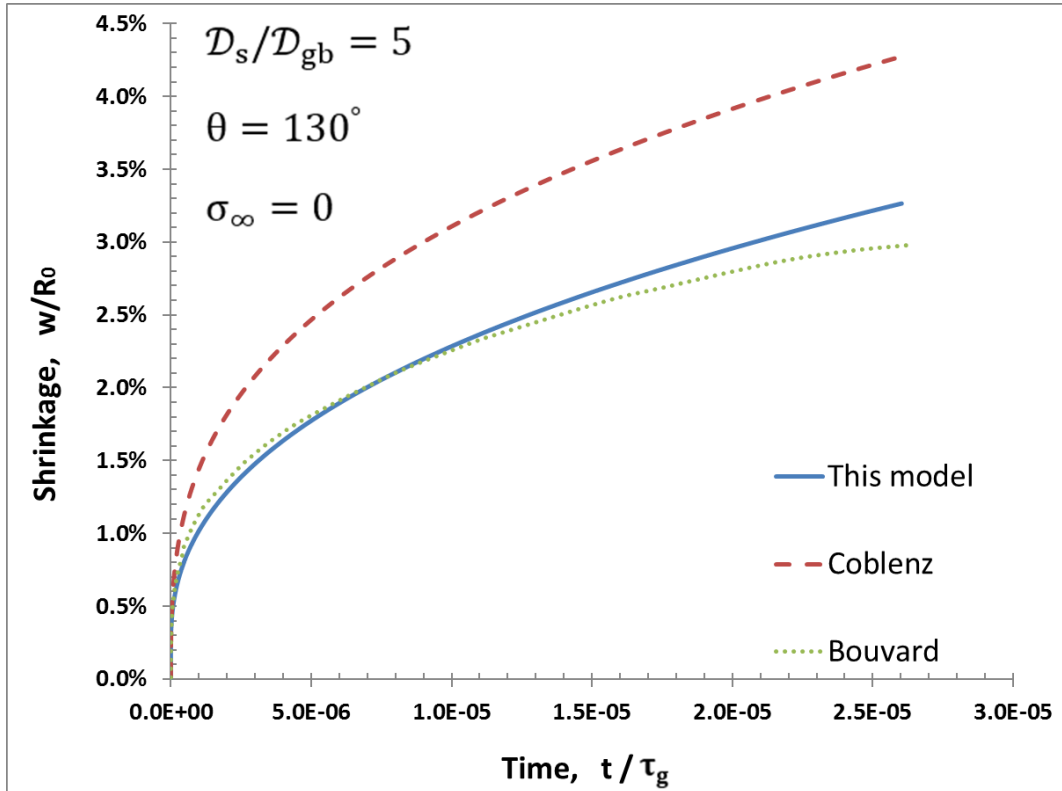
Fig. 3.10 Comparison of shrinkage for $\mathcal{D}_s/\mathcal{D}_{gb} = 5$, $\theta = 130°$ and $\sigma_\infty = 0$

3.3.2 Numerical Results

(1) $\mathcal{D}_s/\mathcal{D}_{gb} = 5$ and $\sigma_\infty = 0 \sim -100\text{MPa}$

Fig. 3.11 shows neck growth over time for $\mathcal{D}_s/\mathcal{D}_{gb} = 5$ and $\sigma_\infty = 0 \sim -100\text{MPa}$. In this figure, the neck grows relatively faster owing to the increase of external pressure during sintering.

Fig. 3.12 shows shrinkage over time for $\mathcal{D}_s/\mathcal{D}_{gb} = 5$ and $\sigma_\infty = 0 \sim -100\text{MPa}$. In this figure, the powder compact densifies much faster due to the increase of external pressure. Besides, the shrinkage of $\sigma_\infty = -100\text{MPa}$ is almost three times of free sintering.

A straightforward explanation can be given by reviewing the expression of V_{gb} [Eq. (3.25)]. When external pressure is applied, an extra driving force is added, hence leading to a faster shrinkage rate. According to the expression of j_{gb} [Eq. (3.10)], the flux of grain-boundary diffusion increases, which means more matter flows out of the triple junction and distributes on the free surface near the triple junction, thus leading to the faster neck growth. From the phenomenological point of view, the mechanism of pressure assisted sintering is like squeezing the matter out of the grain boundary, thus accelerating the densification and neck growth.
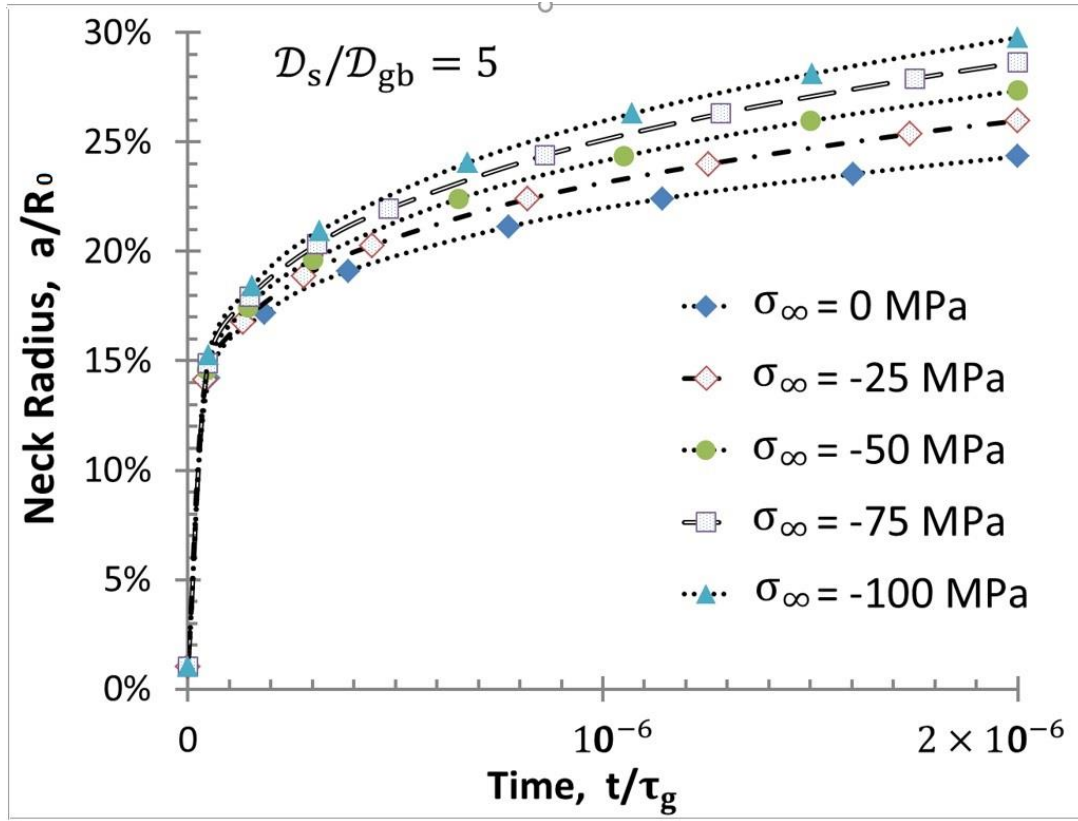
Fig. 3.11 The neck size over time for $\mathcal{D}_s/\mathcal{D}_{gb} = 5$ and $\sigma_\infty = 0 \sim -100\text{MPa}$
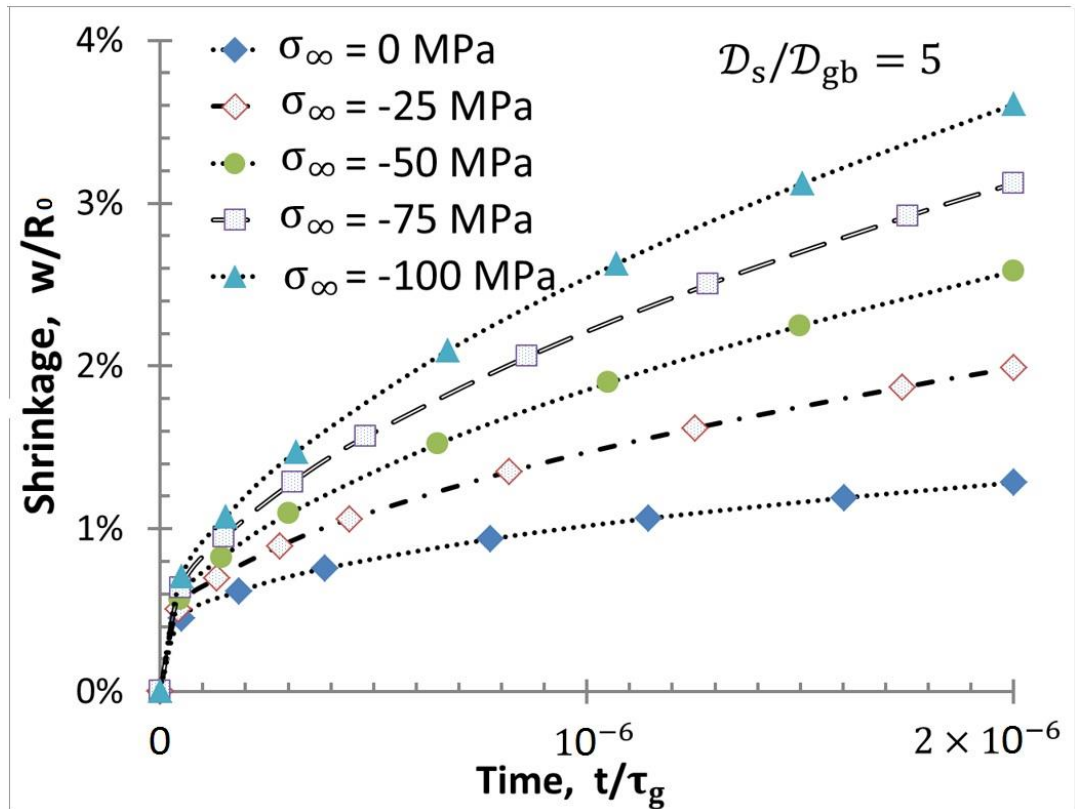
Fig. 3.12 Shrinkage over time for $\mathcal{D}_s/\mathcal{D}_{gb} = 5$ and $\sigma_\infty = 0 \sim -100\text{MPa}$

(2) $\mathcal{D}_s/\mathcal{D}_{gb} = 50$ and $\sigma_\infty = 0 \sim -100$MPa

Fig. 3.13 shows neck growth over time for $\mathcal{D}_s/\mathcal{D}_{gb} = 50$ and $\sigma_\infty = 0 \sim -100$MPa. In this figure, the similar phenomenon is observed, and the neck grows faster with the increase in external pressure.

Fig. 3.14 shows shrinkage over time for $\mathcal{D}_s/\mathcal{D}_{gb} = 50$ and $\sigma_\infty = 0 \sim -100$MPa. In this figure, the same effect of external pressure on shrinkage is observed.

Noticeably, three critical phenomena are observed as follows.

(a) Comparing the neck sizes of free sintering in Fig. 3.11 and Fig. 3.13 respectively, a faster surface diffusion leads to a lager neck size in the same time.

(b) Comparing the shrinkage of free sintering in Fig. 3.12 and Fig. 3.14 respectively, a faster surface leads to the slower shrinkage that is opposite to the case for neck growth.

(c) Comparing the neck sizes of pressure assisted sintering in Fig. 3.11 and Fig. 3.13 respectively, the effect of external pressure on neck growth is weakened.

Due to these three important phenomena, a doubt "Is fast surface diffusion a justified assumption for modelling first-stage sintering by coupled grain-boundary and surface diffusion?" is proposed.
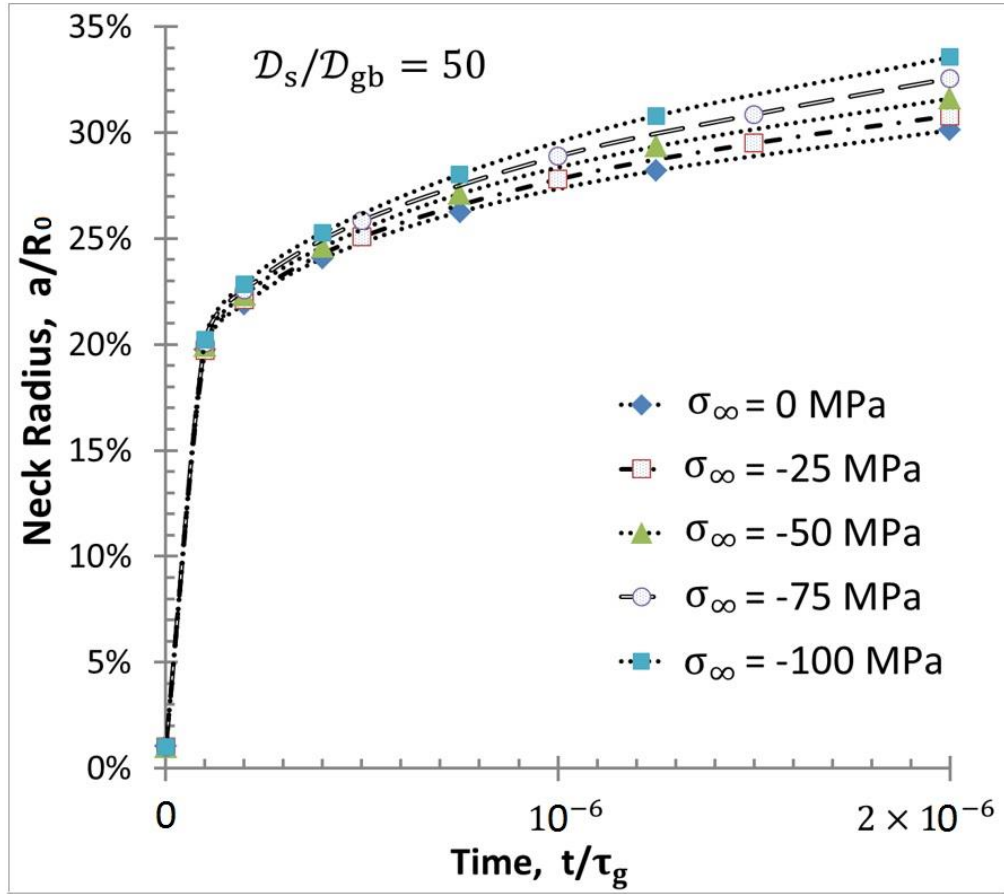
Fig. 3.13 The neck size over time for $\mathcal{D}_s/\mathcal{D}_{gb} = 50$ and $\sigma_\infty = 0 \sim -100\text{MPa}$
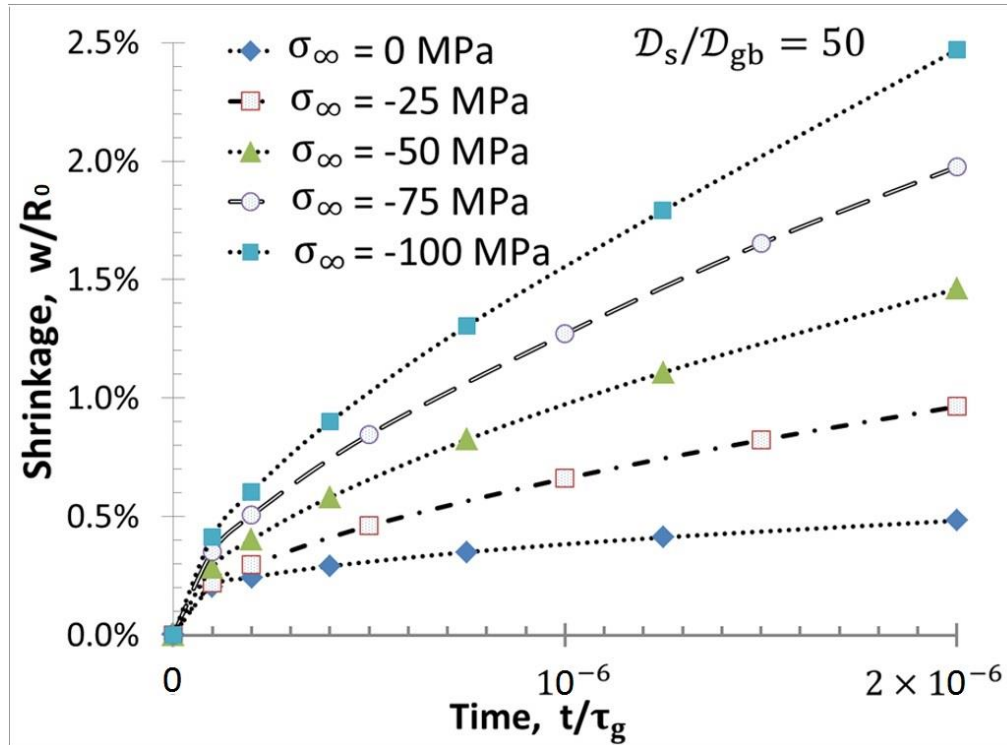
Fig. 3.14 Shrinkage over time for $\mathcal{D}_s/\mathcal{D}_{gb} = 50$ and $\sigma_\infty = 0 \sim -100\text{MPa}$

(3) $\mathcal{D}_s/\mathcal{D}_{gb} = 100$ and $\sigma_\infty = 0 \sim -100\text{MPa}$

Fig. 3.15 shows neck growth over time for $\mathcal{D}_s/\mathcal{D}_{gb} = 100$ and $\sigma_\infty = 0 \sim -100\text{MPa}$. In this figure, except for the features mentioned above, the effect of external pressure on neck growth is quite small. Specifically, if the ratio $\mathcal{D}_s/\mathcal{D}_{gb}$ keeps increasing, its effect can be ignored.

Fig. 3.16 shows shrinkage over time for $\mathcal{D}_s/\mathcal{D}_{gb} = 100$ and $\sigma_\infty = 0 \sim -100\text{MPa}$. In this figure, except the features mentioned above, the promoting effect of external pressure on shrinkage is confirmed again.
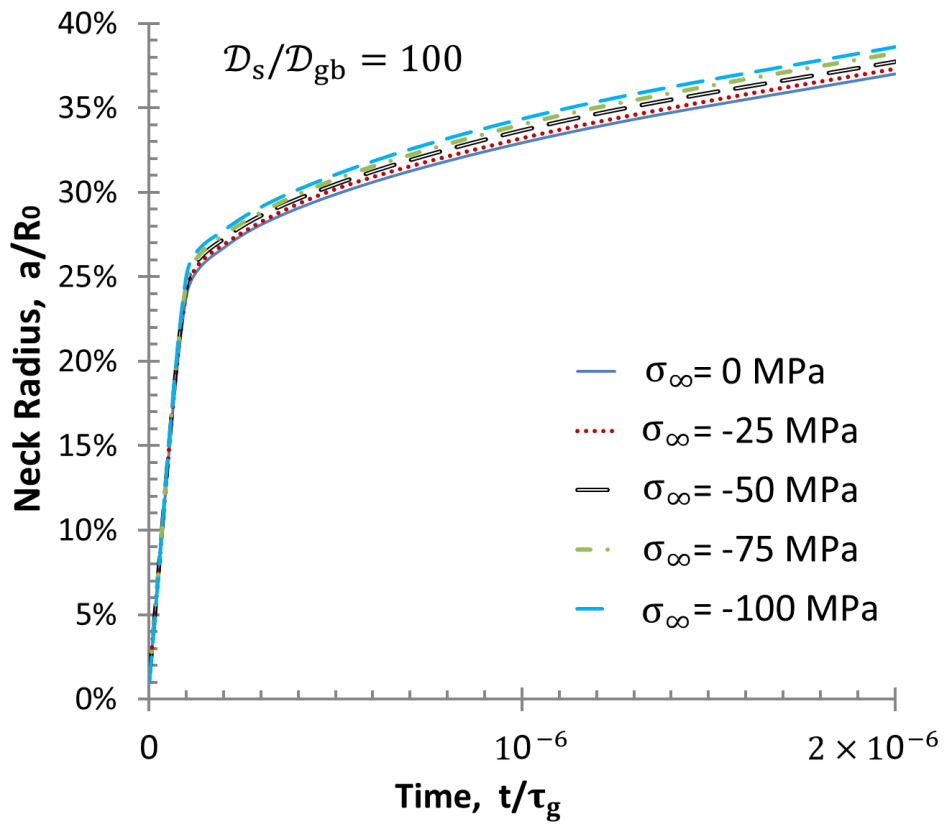
Fig. 3.15 The neck size over time for $\mathcal{D}_s/\mathcal{D}_{gb} = 100$ and $\sigma_\infty = 0 \sim -100\text{MPa}$
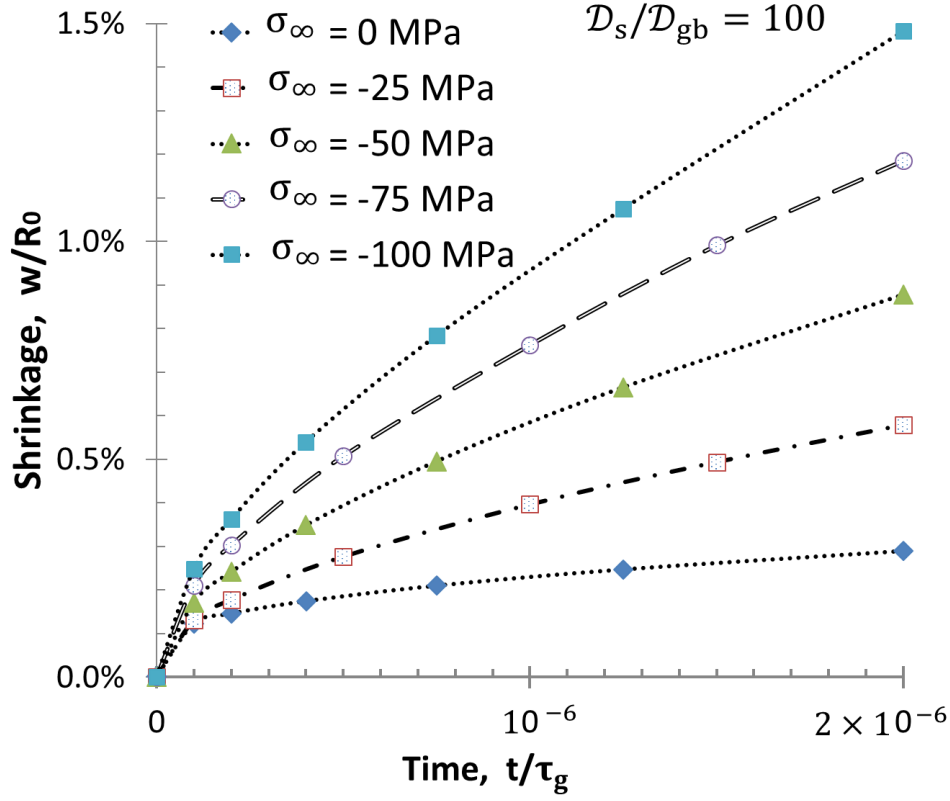
Fig. 3.16 Shrinkage over time for $\mathcal{D}_s/\mathcal{D}_{gb} = 100$ and $\sigma_\infty = 0 \sim -100$MPa

3.3.3 Effects of Surface Diffusion and External Pressure on Neck Growth

Aiming to find the inside mechanism, a series of cases listed in Table 3.2 has been computed. A fixed neck size of $\mathbf{a/R_0 = 25}$% is selected for comparing the sintering time of reaching this ratio.

Fig. 3.17 shows the time taken for the neck radius to reach a = 25% R_0 as a function of the relative diffusivity $\mathcal{D}_s/\mathcal{D}_{gb}$ for different values of the external pressure σ_∞. Three observations can be made from the figure as follows.

(a) The faster surface diffusion always leads to the faster neck growth over this large range of $\mathcal{D}_s/\mathcal{D}_{gb}$.

(b) The surface diffusion process has to be modelled in order to calculate the neck growth; i.e. the assumption of fast surface diffusion does not make sense when calculating neck growth.

(c) The effect of the applied compressive force on neck growth can be ignored if $\mathcal{D}_s/\mathcal{D}_{gb} >$ 100.
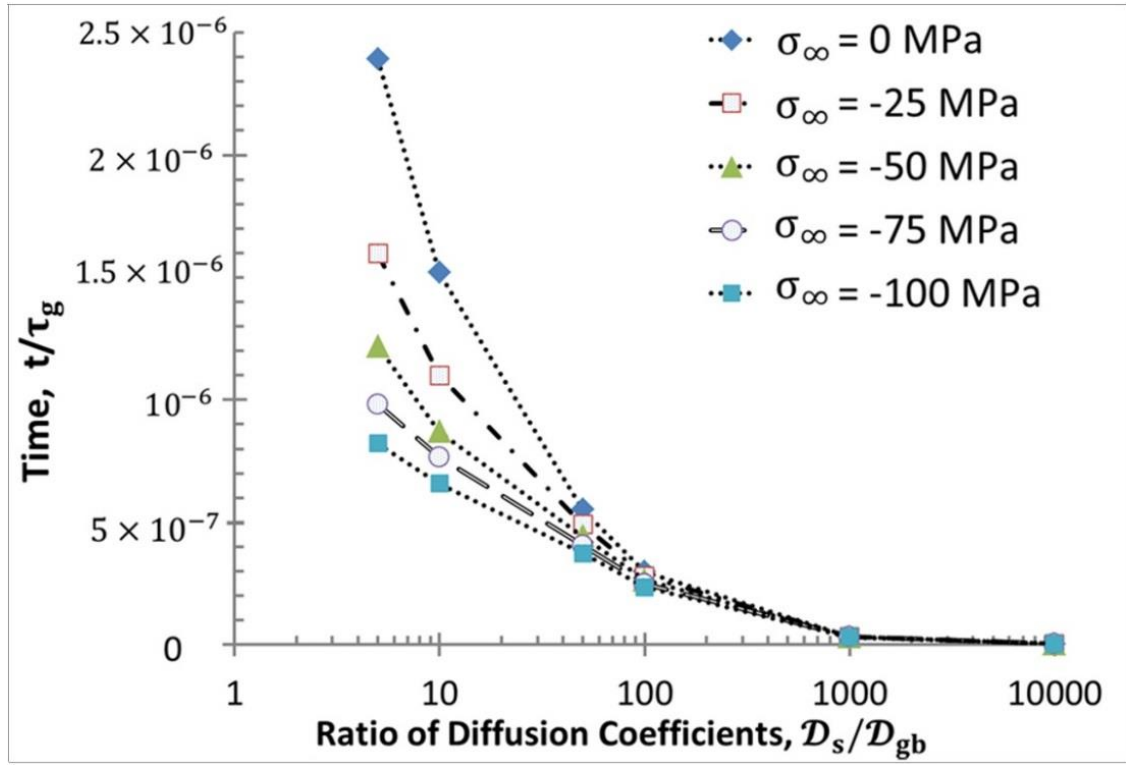
Fig. 3.17 Time taken for the neck radius to reach $a = 25\%$ R_0 as a function of the relative diffusivity $\mathcal{D}_s/\mathcal{D}_{gb}$ for different external pressure σ_∞

In order to further understand these numerical findings, Table 3.3 presents the directions of the surface diffusion flux in the vicinity of the triple junction. Then, to demonstrate the effect of surface diffusion only, results are obtained from the cases without the external pressure. The observation point is selected at a small arc length of s/R=0.06 away from the triple junction. In the numerical analysis, the surface diffusion flux may oscillate with time. In order to obtain a stabled direction, the surface diffusion flux at this point was integrated during a small period of $t = 10^{-9}\tau_g$. It can be observed that surface diffusion changes the direction at $\frac{\mathcal{D}_s}{\mathcal{D}_{gb}} = 50$, which has a profound implication on our understanding of the role played by surface diffusion during the sintering process. If surface diffusion is not too fast when compared with grain-boundary diffusion, it helps move atoms away from the triple junction. However, if surface diffusion is about 50 times faster than grain-boundary diffusion, it moves atoms from the particle surface unto the junction.

Fig. 3.18 (a), (b) and (c), the profiles of the triple junction for $\mathcal{D}_s/\mathcal{D}_{gb} = 5$ and $\mathcal{D}_s/\mathcal{D}_{gb} = 50$ are compared respectively during three different periods. In order to demonstrate the effect of surface diffusion only, results are obtained from the cases without the applied

compressive force. In the figure, because of the reversed surface diffusion for $\mathcal{D}_s/\mathcal{D}_{gb} = 50$, the neck grows faster than that of $\mathcal{D}_s/\mathcal{D}_{gb} = 5$. However, the local curvature near the junction also becomes smaller for $\mathcal{D}_s/\mathcal{D}_{gb} = 50$ than in the case of $\mathcal{D}_s/\mathcal{D}_{gb} = 5$. As shown in the next sub-section, this blunting of the triple junction retards grain-boundary diffusion as well as densification. This mechanism will be detailedly discussed in the next sub-section.

Table 3.3 The Direction of the Surface Diffusion Flux Near the Triple Junction

$\sigma_\infty = 0,$ $\mathcal{D}_s/\mathcal{D}_{gb}$	Direction of surface diffusion flux, + for away from the junction
5	**+**
10	**+**
50	**-**
100	**-**
1000	**-**

Fig. 3.18 Comparison of profiles of the triple junction for $\mathcal{D}_s/\mathcal{D}_{gb} = 5$ and 50 respectively at (a) $t/\tau_g = 10^{-7}$, (b) $t/\tau_g = 10^{-6}$ and (c) $t/\tau_g = 10^{-5}$

3.3.4 Effects of Surface Diffusion and External Pressure on Shrinkage

The fixed shrinkage of $w/R_0 = 1\%$ is selected for comparing the sintering time of reaching this ratio.

Fig. 3.19 shows the time taken for the shrinkage to reach $w = 1\% \, R_0$ as a function of $\mathcal{D}_s/\mathcal{D}_{gb}$ for a range of remote stress σ_∞. Three observations can be made from the figure as follows.

(a) The faster surface diffusion always leads to the slower shrinkage in opposite to the case for neck growth.

(b) The assumption of fast surface diffusion cannot be valid because a change in $\mathcal{D}_s/\mathcal{D}_{gb}$ always leads to a significant change in the shrinkage rate especially for free sintering.

(c) The external pressure always has a significantly beneficial effect on shrinkage.

Bouvard and McMeeking [20] reported the detrimental effect of surface diffusion on shrinkage, as shown in Fig. 3.19. In the figure, the time for cases of different diffusivity ratio ξ reaching $1\% R_0$ varies largely. Time for $\xi = 6$ reaching $1\% R_0$ is comparable to time for $\xi = 2$, because grain-boundary diffusion is much faster than surface diffusion in the sintering of these two ratios, and there is no backflow of surface diffusion near the triple junction area. Thus, the sharpness on the triple junction is kept, and densification of the powder compact is not retarded. For cases of $\xi = 0.2$ and 0.02, time for shrinkage reaching $1\% R_0$ becomes longer as ξ gets smaller. A similar explanation is given. To be specific, fast surface diffusion causes a diffusion backflow near the triple junction, and then blunting of the triple junction retards grain-boundary diffusion and densification.

The results in Fig. 3.20 confirm and strengthen their conclusion using a clearer presentation. Our study also provides a straightforward explanation for this detrimental effect – the surface diffusion changes its direction as $\mathcal{D}_s/\mathcal{D}_{gb}$ increases. As shown in the previous sub-section, the reversed surface diffusion blunts the triple junction and hence reduces the driving force for grain-boundary diffusion. Furthermore, it is important to observe from Fig. 3.20 that the detrimental effect of surface diffusion on densification is still significant even if the remote pressure is applied although this effect is significantly weakened.
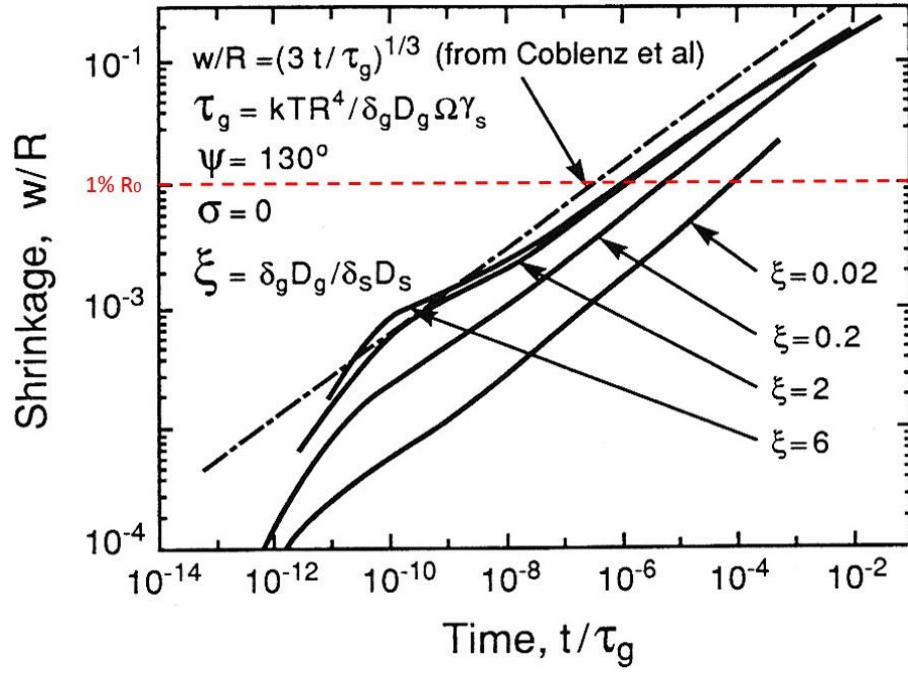
Fig. 3.19 Effect of the diffusivity ratio ξ on the evolution of the shrinkage and a comparison with the model of Coblenz for $\psi = 130°$ and $\sigma_\infty = 0$ [20]
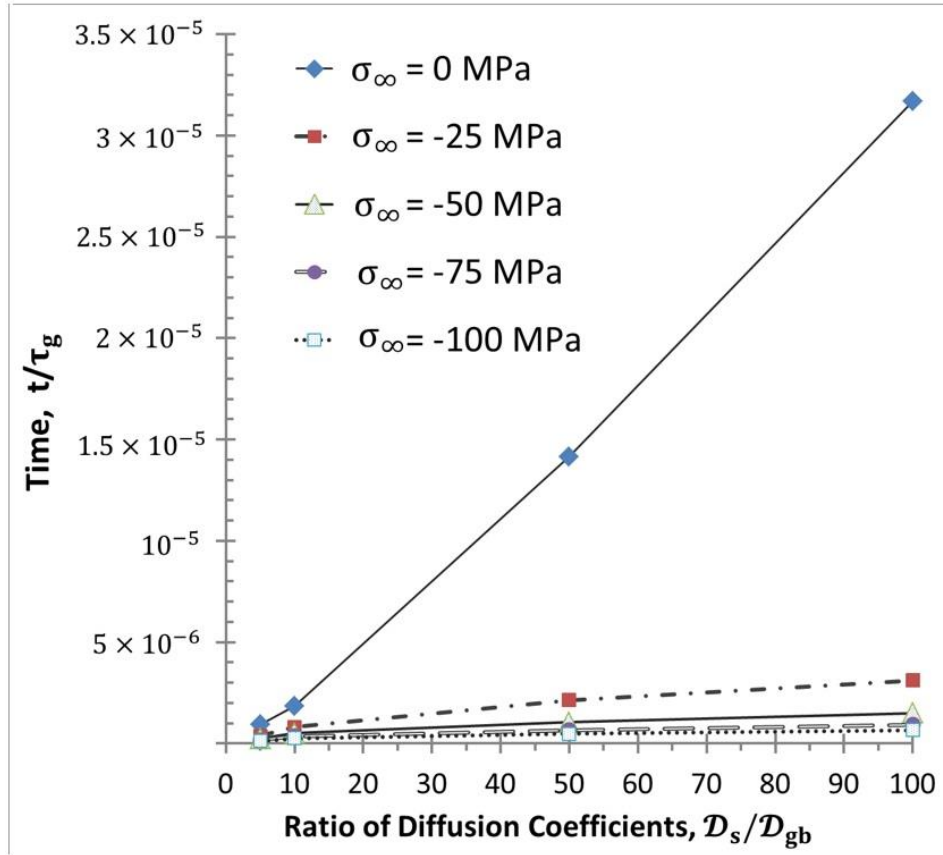
Fig. 3.20 Time taken for shrinkage to reach $w = 1\% R_0$ as function of $\mathcal{D}_s/\mathcal{D}_{gb}$ for a range of remote stress σ_∞

3.4 Summary of This Chapter

The curvature of the triple junction κ_{tip} is numerically solved as a combination of all sintering variables acting at the triple junction, which means it depends on the diffusivity, the external stress, surface tension, the dihedral angle and the local-area curvature. Therefore, it cannot be simply considered as the curvature which could be determined from the local geometry of the free surface at the triple junction. If there is more driving force for densification during sintering, they can also be added into the formula of κ_{tip}.

Furthermore, the numerical study in this chapter reveals or reconfirms the following conclusions.

(a) The assumption of fast surface diffusion is invalid for almost all practical circumstances.

(b) The faster surface diffusion always leads to a slower shrinkage rate and a faster neck growth rate.

(c) The effect of external pressure on neck growth can be ignored if surface diffusion is fast enough.

(d) The external pressure always has a significantly beneficial effect on shrinkage.

Finally, by analysing the numerical results, this study gives an extremely clear and straightforward explanation for the effect of surface diffusion. Surface diffusion in the vicinity of the triple junction changes the direction from moving atoms away from the junction to depositing atoms onto the junction as the rate of surface diffusion increases. The reverse surface diffusion blunts the triple junction and hence retards densification. It however accelerates neck growth.

Chapter 4 Effect of the Fast Heating Rate on Sintering

4.1 Introduction

Spark plasma sintering (SPS) is a recent sintering technique mainly characterized by high assisting pressure, a fast heating and cooling rate and short sintering time. These characteristics make SPS an advanced technique that can produce highly dense materials with the controlled microstructure. Due to its excellent densify effect, SPS gives an effective method for ceramics sintering, especially for nano-sized powders. However, there are many unclear understandings of the SPS's fundamental mechanism. These unclear understandings result from the complexity of the thermal, electrical and mechanical processes that may be involved during SPS.

In summary, the complexity of SPS is mainly composed of the electrical field, the stress field and the thermal field [46]. Therefore, most of the studies focus on these three aspects to reveal the working mechanism inside SPS. The main observation of this chapter concerns the fast heating process during SPS. For the effect of the fast heating (Joule heating) rate on SPS, so many experiment studies have been conducted, and many phenomenological explanations have been given, but few numerical studies were given to reveal its working mechanism during SPS.

A phenomenon was observed from SPS of Alumina by Shen et al [47] when compared with that density under a slow heating rate, and the sample is densified under a fast heating rate with a smaller grain size when heating rates range from several degrees Celsius to hundreds of degrees Celsius per minute. Additionally, Zhou et al [48] also observed a similar phenomenon from pulse electric current sintering of alumina when the grain size drastically reduces as the heating rate increases from 50 to 700ºC. Similarly, Sairam et al [49] qualitatively pointed out that Joule heating plays a governing role in densification of powder compacts during SPS of boron carbide, which leads to a higher density at lower temperature when compared with the conventional sintering technique.

Olevsky et al [50] developed a constitutive model considering the interplay between three mechanisms of material transport: surface diffusion, grain-boundary diffusion and power-law creep. Their model shows that a better sinter ability can be achieved by increasing the

heating rate and this effect is attributed to the different shapes that the pore develops under different heating rates.

Furthermore, Guillon et al [51] developed an analytical approach called master sintering curve to estimate different relative densities at different heating rates. When compared with the sample sintered with a fast heating rate, the sample sintered with a slow heating rate obtains higher density during heating.

Purposes of This Chapter

As the interest is significantly aroused by the fast heating rate in SPS, the purposes of this chapter are to (a) develop a temperature dependent model that can simulate the sintering with a heating process from 600 ºC to 1400ºC, (b) take account of surface diffusion and numerical solution of the curvature on the triple junction into this numerical model and (c) reconfirm the work of Olevsky et al [50] and provide a straightforward understanding of the reason why the fast heating rate is conducive to densification. Furthermore, different heating rates of SPS and traditional sintering are used for computation. Additionally, the external applied pressure is also introduced into this model.

4.2 Methodology

Olevsky et al [50] developed a model that predicts the increasing heating rate benefits densification because a favourable pore shape develops under the higher heating rate. In their model, surface diffusion is treated in isolation, which is a simplification that requires some validation. Hence, the study in this paper is presented following the same argument but using a fully numerical analysis.

A temperature dependent model is developed for simulating the sintering under a heating process from 600°C to 1400°C with different heating rates. Except for the diffusion coefficients, other parameters used in this chapter are the same as chapter 2. To simulate the heating process during sintering, grain-boundary diffusion coefficient $\mathcal{D}_{gb}$ and surface diffusion coefficient $\mathcal{D}_s$ are defined as temperature dependent variables.

(1) Temperature Dependence of Grain-boundary Diffusivity $\mathcal{D}_{gb}$

According to Eq. (3.32), grain-boundary diffusivity $\mathcal{D}_{gb}$ depends on temperature:

$$\mathcal{D}_{\text{gb}} = \frac{\Omega(D_{\text{gb0}}\delta_{gb})\exp(-Q_{gb}/RT)}{kT}$$

where Ω is the atomic volume; D_{gb0} is the pre-exponential coefficient for grain-boundary diffusivity; δ_{gb} is the thickness of the grain-boundary diffusion layer; Q_{gb} is the activation energy of grain-boundary diffusion; R is the gas constant; k is Boltzmann's constant and T is absolute temperature of sintering.

In order to describe the heating process, thermodynamic temperature of sintering T is defined as $T = T_0 + \text{heating rate} * \Delta t$. Table 4.1 presents the data used for $D_{\text{gb0}}\delta_{\text{gb}}$ and Q_{gb} in the simulations. These data are from a data book of alumina [52] and are selected here because they come from the single source. Furthermore, other parameters used in the numerical study are provided in Table 4.1.

Table 4.1 Values of $D_{\text{gb0}}\delta_{\text{gb}}$ and Q_{gb} Used in the Simulation

Authors	Year	$D_{\text{gb0}}\delta_{\text{gb}}$ (m^3/s)	Q_{gb} (J / mol)
Cannon et al. [53]	1980	8.6×10^{-10}	4.18×10^5

(2) Temperature dependence of surface diffusivity $\mathcal{D}_{\text{s}}$

According to Eq. (3.33), grain-boundary diffusivity $\mathcal{D}_{\text{gb}}$ depends on temperature:

$$\mathcal{D}_{\text{s}} = \frac{\Omega\gamma_{\text{s}}(D_{\text{s0}}\delta_{\text{s}})\exp(-Q_s/RT)}{kT}$$

where Ω is the atomic volume; D_{s0} is the pre-exponential coefficient for surface diffusivity; δ_{s} is the thickness of the surface diffusion layer; Q_s is the activation energy of surface diffusion and δ_{s} is simply defined as $\sqrt[3]{\Omega}$.

The definition of thermodynamic temperature in sintering T is the same. Table 4.2 shows the three sets of data for D_{s0} and Q_s used in the simulations from a data book of alumina [52]. Data for surface diffusivity reported in the literature varies significantly due to different measurement techniques. Furthermore, other parameters used in the numerical study are provided in Table 3.1.

Table 4.2 Values of D_{s0} and Q_s Used in the Simulation

Set No.	Authors	Year	D_{s0} (m^2/s)	Q_s (J / mol)
1. Minimum	Prochazka & Coble [54]	1970	4.8×10^{-6}	2.34×10^5
2. Intermediate	Prochazka & Coble [54]	1970	1.15×10^{-3}	2.8×10^5
3. Maximum	Moriyoshi & Komatsu [55]	1973	1.06×10^{-2}	2.67×10^5

(3) The trend diagram of the effective surface and grain-boundary diffusivity as function of temperature

When substituting the values in Table 4.1 and 4.2 into Eq. (3.32) and (3.33) respectively, the values of $\mathcal{D}_{gb}$ and $\mathcal{D}_s$ as the temperature function are plotted in Fig. 4.1. In the figure, it is clear that $\mathcal{D}_{gb}$ and $\mathcal{D}_s$ have extremely different dependence on the temperature because of their different activation energy. At 600 ^{o}C, $\mathcal{D}_s$ is about five orders of magnitude larger than $\mathcal{D}_{gb}$ while at 1400 ^{o}C, $\mathcal{D}_s$ is only about dozens of times larger than $\mathcal{D}_{gb}$ according to data set 2 or even slightly smaller than $\mathcal{D}_{gb}$ according data set 1. As observed in chapter two, this change in the relative diffusivity can have a profound effect on the sintering kinetics. However, at the lower temperature, the absolute diffusion rates are also several orders of magnitude smaller than those at the higher temperature. It is therefore difficult to draw conclusions by just observing Fig. 4.1. Hence, further studies are conducted in the next sub-section by simulating a series of cases of different heating rates.
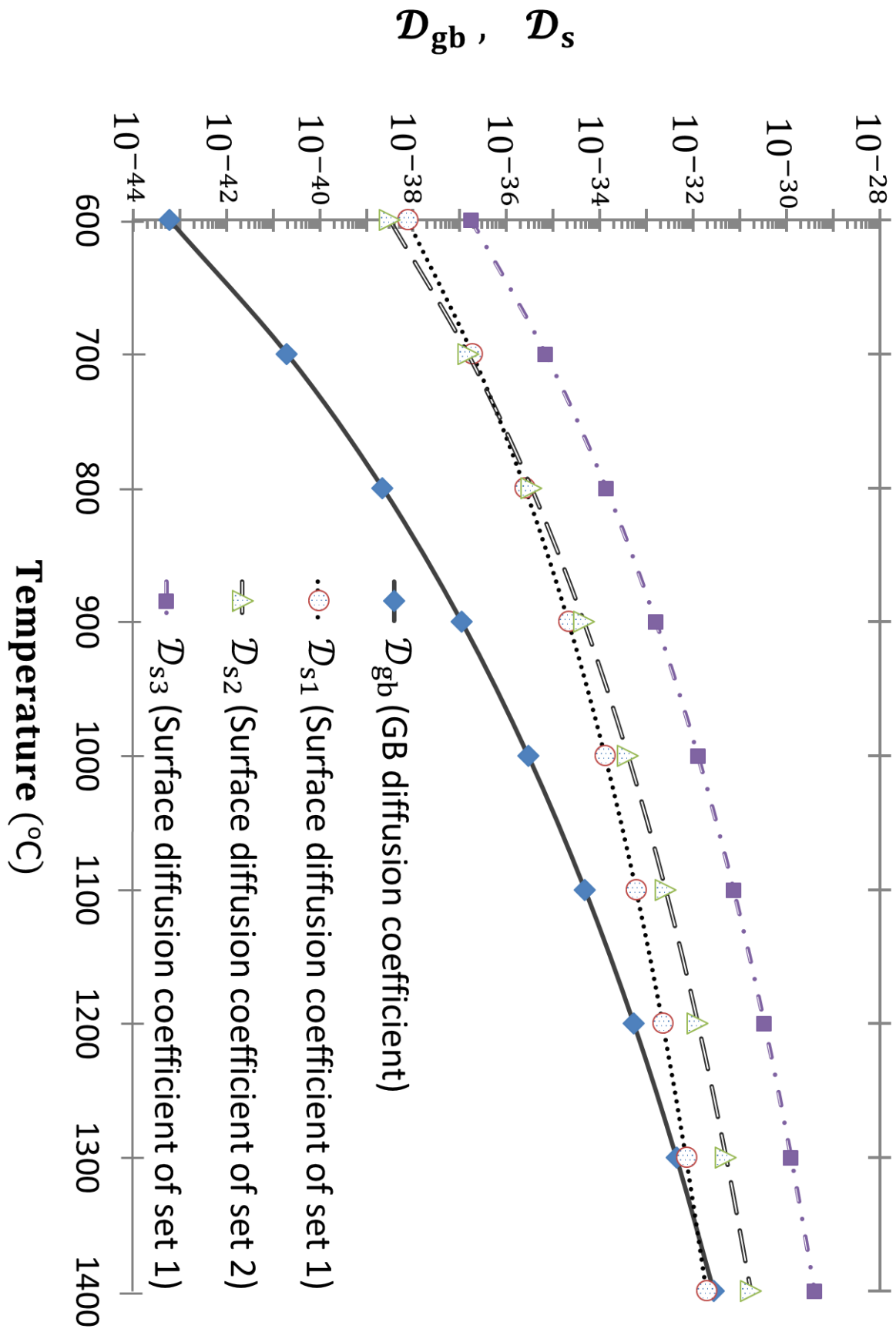
Fig. 4.1 The effective surface and grain-boundary diffusivity as function of temperature

4.3 Effect of the Heating Rate on Sintering

In order to study the effect of the heating rate on sintering, the cases of different heating rates are simulated in this study as listed in Table 4.3. Computer simulations with the temperature rise from 600°C to 1400°C are carried out using heating rates of 2 °C /min and 10 °C /min which are typical for traditional sintering [41], and using 100 °C /min and 200 °C /min which can be achieved by SPS [47]. It is difficult to compare results for the different heating rates because they all have significantly different time scales of sintering. To eliminate the effect of the time scale, different heating rates can be compared on a single standard, and the figure of shrinkage is plotted versus the neck size, which means y coordinate is shrinkage while x coordinate is the neck radius.

Table 4.3 Cases of Different Heating Rates

Simulation Cases		$\mathcal{D}_{s1}$		$\mathcal{D}_{s2}$		$\mathcal{D}_{s3}$	
External Pressure		**0**	**-50 MPa**	**0**	**-50 MPa**	**0**	**-50 MPa**
$\mathcal{D}_{gb}$	**HR=2 °C /min**	√	√	√	√	√	√
	HR=10 °C /min	√	√	√	√	√	√
	HR=100 °C /min	√	√	√	√	√	√
	HR=200 °C /min	√	√	√	√	√	√

4.3.1 Numerical Results

(1) Set 1, $\mathcal{D}_{s1}$ and $\sigma_\infty = 0, -50$MPa

Fig. 4.2 shows shrinkage versus the neck size as the temperature is increased from 600 °C to 1400 °C with different heating rates. In this case, the applied pressure is set as zero and surface diffusivity of set 1 in Table 4.2 is used. It can be observed from the figure that a higher heating rate clearly benefits densification. When comparing the two extreme cases of heating rates of 2 °C /min and 200 °C /min, at any fixed value of the neck size, the fast heating rate generates much more shrinkage than the slow one, simply because the faster heating rate helps sintering quickly pass the lower temperature range, where surface diffusion is much faster than grain-boundary diffusion as shown in Fig. 4.1, hence minimizes the blunting effect of fast surface diffusion near the triple junction.

It would be expected that this particular mechanism of the heating rate effect diminishes if the external pressure is applied. Such expectation comes from the proposition that the large

external pressure, relative to the sintering potential which is in the order of 1-2MPa for micron-sized powders, would dominate densification, and hence the blunting effect becomes less significant. Fig. 4.3 shows the numerical results for $\sigma_\infty = -50$ MPa with all other conditions identical to the case of Fig. 4.2. Obviously, the applied pressure leads to the larger shrinkage. It is interesting to observe that the heating rate effect is still significant even for such large applied pressure. The fast heating rate and high pressure used in Fig. 4.3 are typical for SPS. It is therefore reasonable to argue that limiting the backflow of surface diffusion and its corresponding blunting effect can at least partially explain the SPS effect reported in the literature.
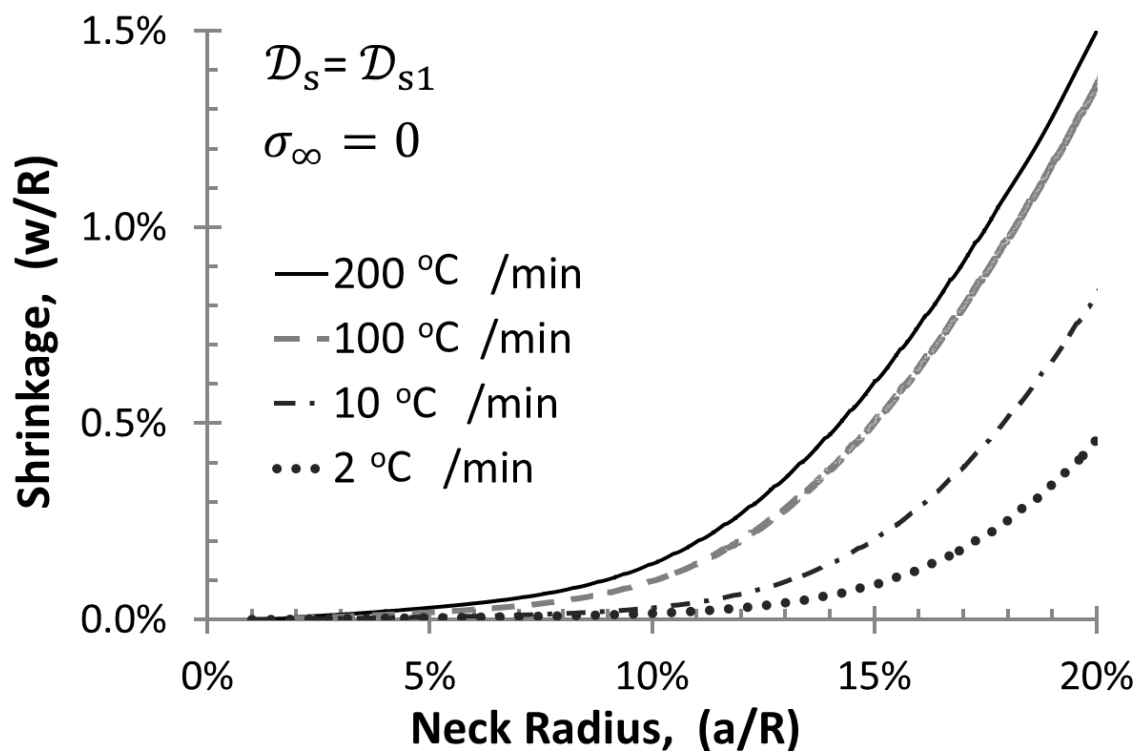
Fig. 4.2 Shrinkage versus the neck size as temperature increases from $600\,^{\circ}\mathrm{C}$ to $1400\,^{\circ}\mathrm{C}$ with different heating rates. The external pressure is zero. Data of set 1 in Table 4.2 for surface diffusivity was used.

Fig. 4.3 Shrinkage versus the neck size as temperature increases from $600\,^{\circ}C$ to $1400\,^{\circ}C$ with different heating rates. The external pressure is $\sigma_\infty = -50$ MPa . Data of set 1 in Table 4.2 for surface diffusivity was used.

(2) Set 2, $\mathcal{D}_{s2}$ and $\sigma_\infty = 0, -50$MPa

Fig. 4.4 and 4.5 show similar results using data set 2 of surface diffusivity in Table 4.2. The same effects of heating rates are observed. However, the shrinkage achieved at a fixed value of the neck size is significantly reduced when comparing with Fig. 4.2 and 4.3. It can be seen from Fig. 4.1 that the effective surface diffusivity calculated from data set 2 is higher than that from data set 1. This faster surface diffusion rate across the temperature range has led to the significant reduction in shrinkage when comparing Fig. 4.4 and 4.5 with Fig. 4.2 and 4.3. These results once again highlight the important role of surface diffusion when understanding the effect of the heating rate. By examining Fig 4.5, it can be confirmed that surface diffusion plays the significant role even when the large pressure is applied.

(3) Set 3, $\mathcal{D}_{s3}$ and $\sigma_\infty = 0, -50$MPa

Fig. 4.6 and 4.7 present similar results using data set 3 of surface diffusivity in Table 4.2. The same effects of heating rates are also observed. These figures are provided here for completeness.
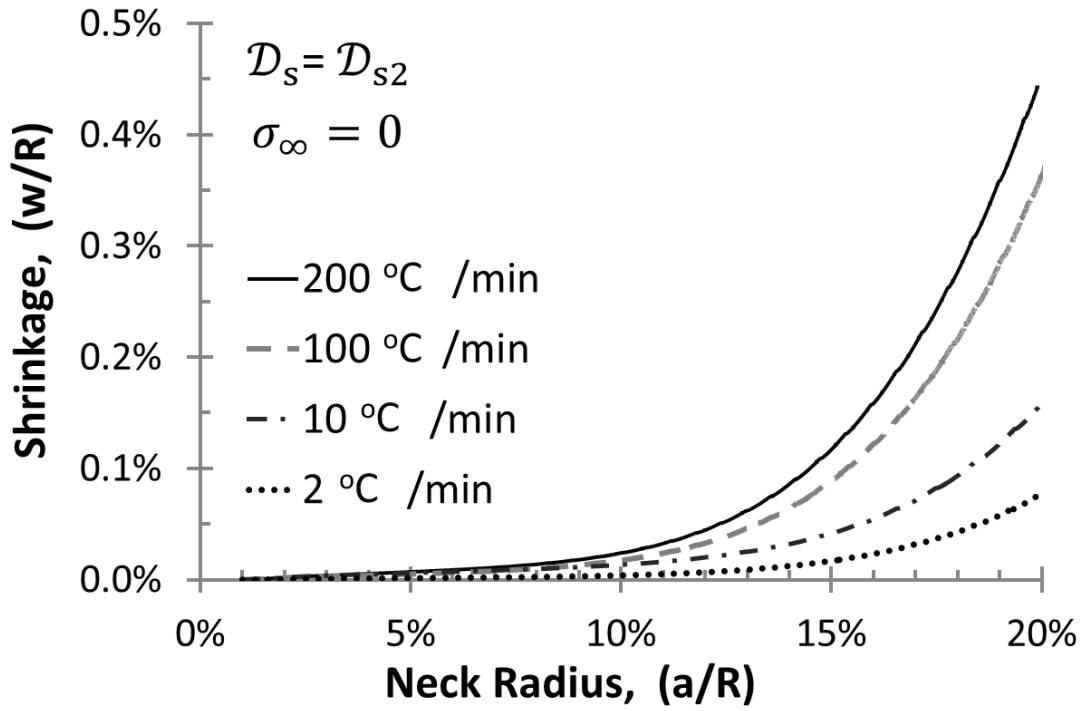
Fig. 4.4 Shrinkage versus the neck size as temperature increases from $600\,^{\circ}$C to $1400\,^{\circ}$C with different heating rates. The external pressure is zero. Data of set 2 in Table 4.2 for surface diffusivity was used.

Fig. 4.5 Shrinkage versus the neck size as temperature increases from $600\,^{\circ}$C to $1400\,^{\circ}$C with different heating rates. The external pressure is $\sigma_{\infty} = -50$ MPa . Data of set 2 in Table 4.2 for surface diffusivity was used.
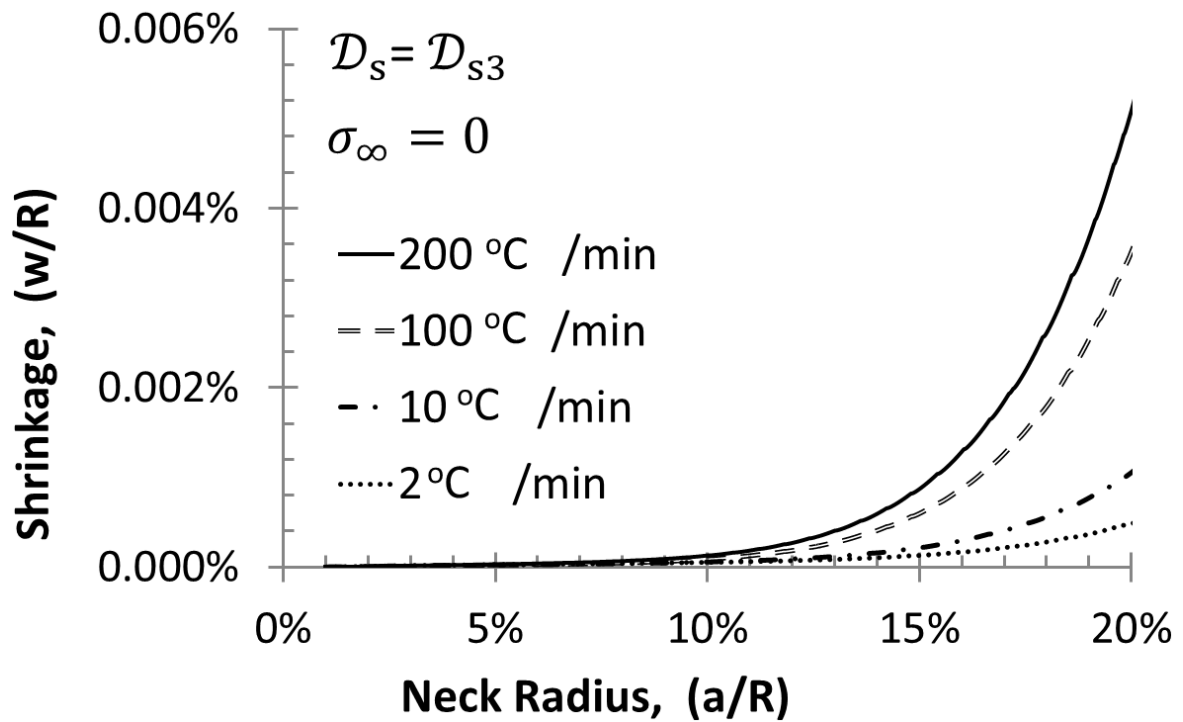
Fig. 4.6 Shrinkage versus the neck size as temperature increases from $600\,^{\circ}\text{C}$ to $1400\,^{\circ}\text{C}$ with different heating rates. The external pressure is zero. Data of set 3 in Table 4.2 for surface diffusivity was used.

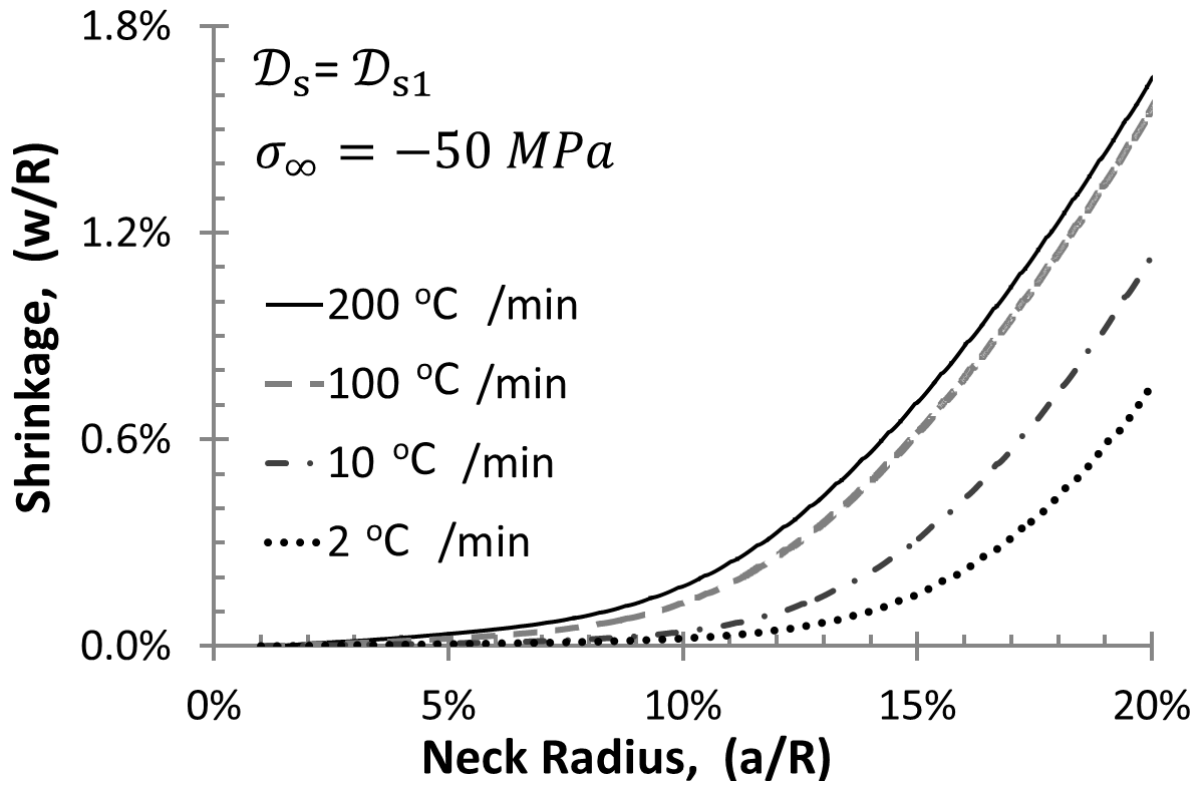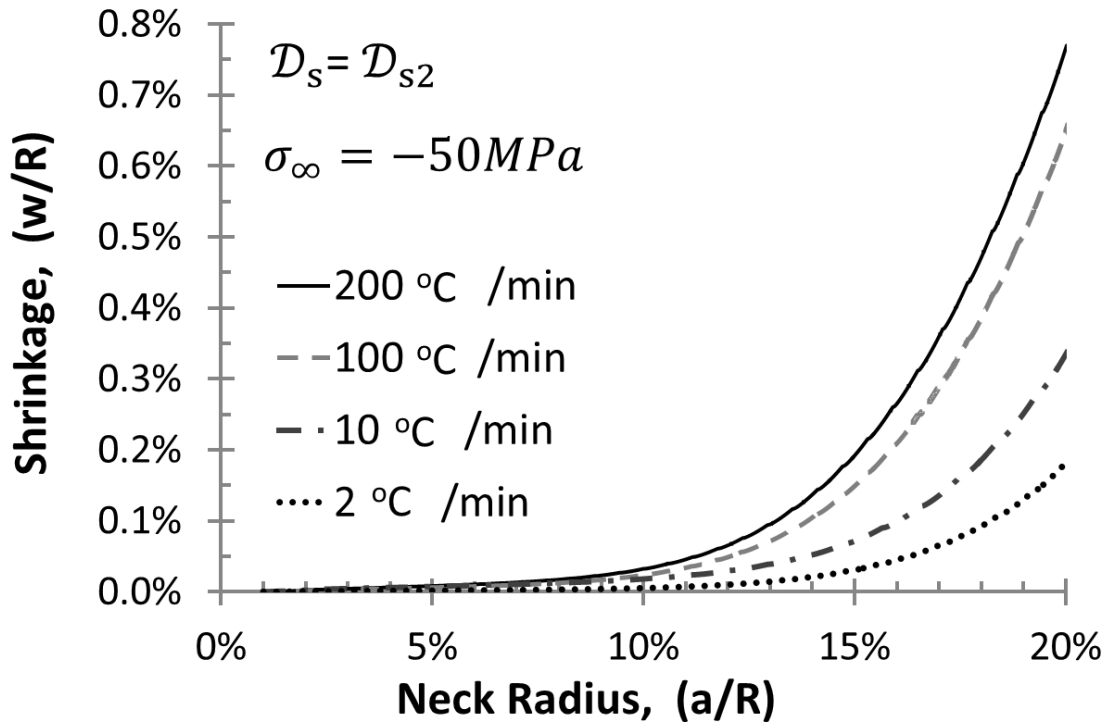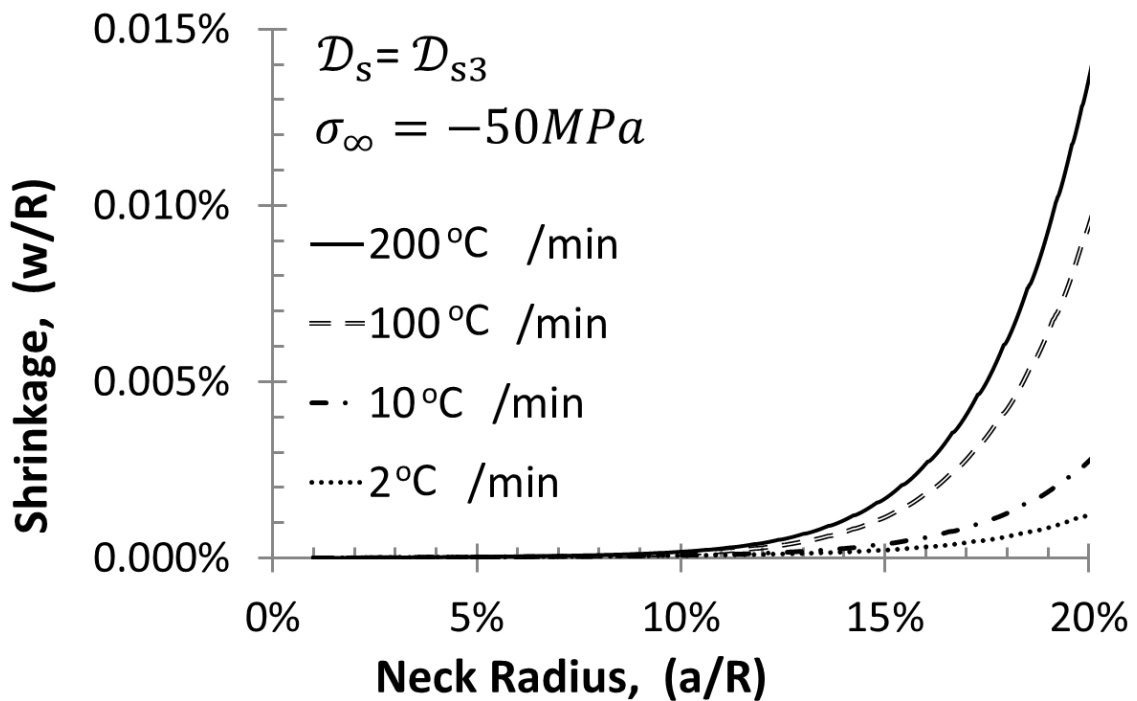**Fig. 4.7** Shrinkage versus the neck size as temperature increases from $600\,^{\circ}\text{C}$ to $1400\,^{\circ}\text{C}$ with different heating rates. The external pressure is $\sigma_\infty = -50$ MPa . Data of set 3 in Table 4.2 for surface diffusivity was used.

4.4 Summary of This Chapter

As mentioned in chapter 3, if the ratio is big enough, surface diffusion changes the direction from moving atoms away from a contact neck to depositing atoms onto it. Subsequently, the reverse surface diffusion blunts the neck and retards densification. The above mechanism can be called as "the backflow of fast surface diffusion".

By analysing the above results and considering "the backflow of fast surface diffusion", the working mechanism for the effect of the fast heating rate on sintering has been clearly revealed. As shown in Table 4.1 and 4.2, surface diffusion and grain-boundary diffusion often have different kinds of activation energy and hence different temperature dependence. As shown in Fig. 4.1, effective surface diffusivity is much larger than effective grain-boundary diffusivity at the low temperature zone (e.g. 600 to 1200 $^{\circ}$C), while effective surface diffusivity is comparable to effective grain-boundary diffusivity at the high temperature zone (e.g. beyond 1200 $^{\circ}$C), which means that fast surface diffusion dominates sintering at the low temperature range while grain-boundary diffusion takes effect on sintering at the high temperature range. When comparing with the results of conventional sintering, fast heating rates, typically used in SPS, help sintering quickly pass through the low temperature range where fast surface diffusion dominates and is detrimental to densification, and then go into the high temperature range where grain-boundary diffusion takes effect and is beneficial to densification. On the contrary, time for slow heating rates passing through the low temperature range is so long, and then the neck area becomes so flat that the driving force of shrinkage is significantly weakened.

Based on the above discussions, the beneficial effect of spark plasma sintering on densification can be, at least partially, attributed to its fast heating rate.

Chapter 5 Effects of Inhomogeneity on Sintering Kinetics

5.1 Introduction

The effects of sintering variables such as applied pressure, temperature, the heating rate and the particle size are well understood by many previous studies. For one-material powder system where identical particles are homogeneously compacted, effects of the variables on sintering kinetics are well described by existing models. However, in real sintering, the powder system cannot be completely homogeneous such as variations in packing density, pore distribution and particle sizes, as well as impurities in powder. This inhomogeneity leads to differential densification during sintering, and different regions in the powder compact sinter with different rates. Differential densification leads to transient stress inside the powder compact, which reduces the densification rate, and leads to growth of structure defects such as large pores and crack voids that limit mechanical properties of ceramic parts. Therefore, it is extremely critical to understand the effects of inhomogeneity and its mechanism on sintering kinetics. Through qualitative and quantitative analysis for the effects of inhomogeneity on sintering kinetics, sintering quality can be improved and structural defects can be reduced by controlling inhomogeneity of sintering variables during sintering.

Due to the importance of inhomogeneity during sintering, some work has been done to reveal the effects of inhomogeneity on sintering kinetics and to demonstrate its working mechanism. Evans [56] proposed a theory that the development of transient stress during sintering is similar to Thermal stress in materials due to different thermal expansion coefficients. In sintering, the volumetric strain rate replaces the thermal strain. A detailed micro model was developed by Raj and Bordia [57], while the spherical inhomogeneity was surrounded by a uniform powder matrix, as shown in Fig. 5.1(a). If spherical inhomogeneity shrinks much slower than the surrounding matrix, reaction stress is generated in the matrix that resists sintering stress, and then leads to a reduction of the densification rate, as shown in Fig. 5.1(b). If the reaction stress is high enough, cracks will appear in the matrix, as shown in Fig. 5.1(c). However, if the spherical inhomogeneity shrinks much faster than the surrounding matrix, a circumferential void will appear between them, as shown in Fig.

5.1(d). The defects illustrated in Fig. 5.1(c) and Fig. 5.1(d) have been observed by Lang [58] in his experiment studies on sintering of heterogeneous powder compacts.
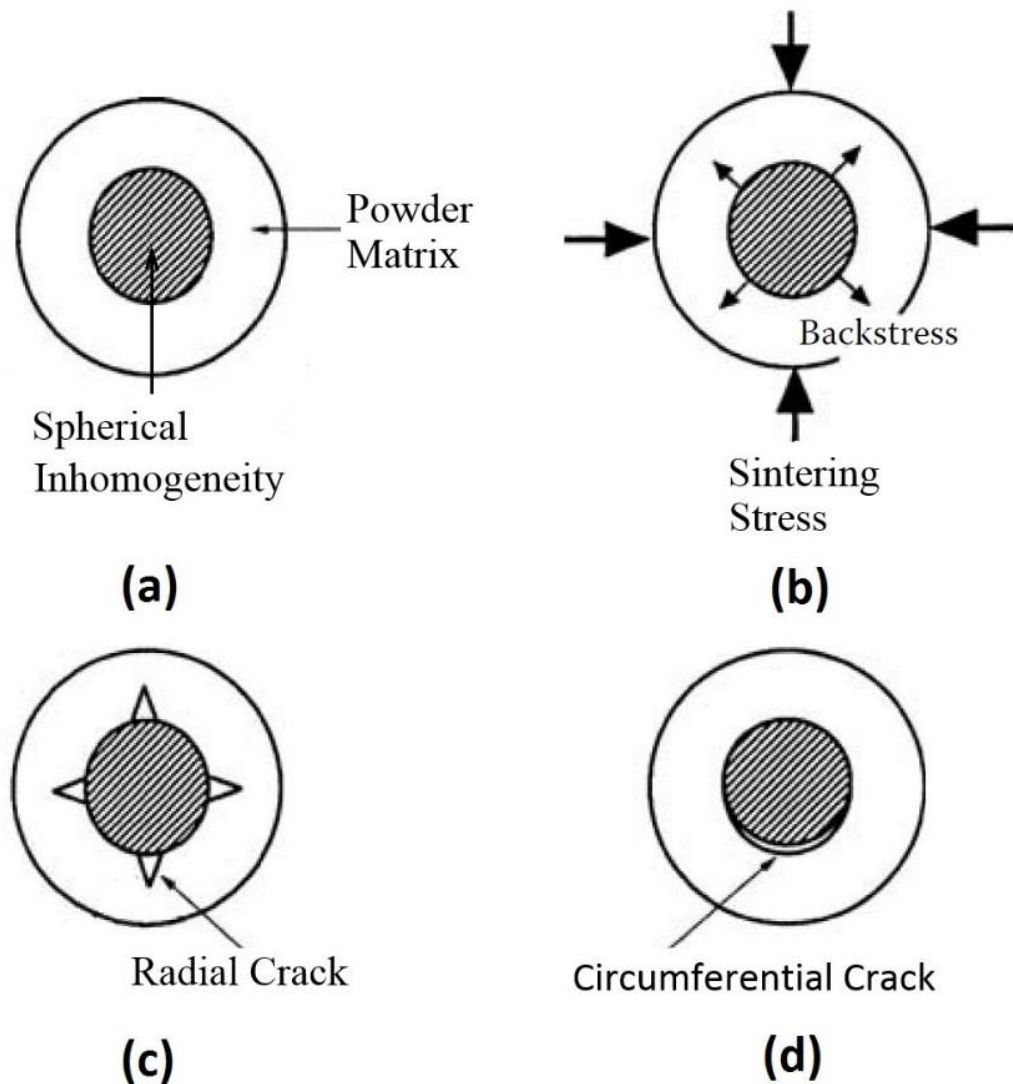
Fig. 5.1 Schematic diagram: (a) the spherical inhomogeneity surrounded by a uniform powder matrix, (b) a reduction of the densification rate because spherical inhomogeneity shrinks much slower than the surrounding matrix, (c) generation of cracks if back stress is high, (d) generation of a circumferential void if spherical inhomogeneity shrinks much faster than the surrounding matrix [57].

Weiser and Jonghe [59] developed a mesoscale model to simulate the microstructural evolution of multi particles during sintering. In their study, a detailed statistical analysis of the evolution reveals that large pores and structural voids occur due to the rearrangement of particles under differential densification, as shown in Fig. 5.2.
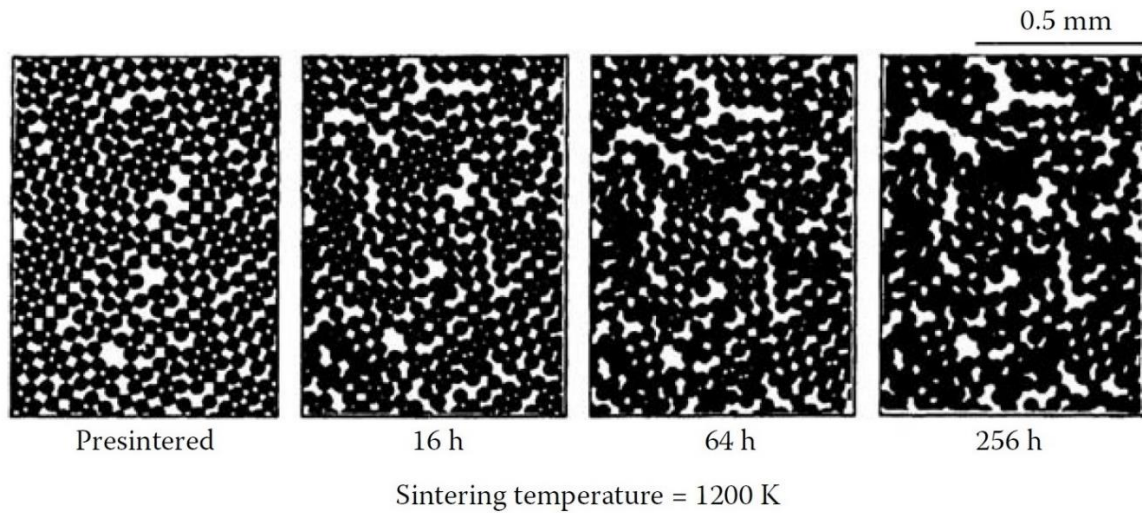
Fig. 5.2 The two-dimensional sphere array showing sintering behaviour and evolution of the structure [59]

Sudre and Lange [60] observed a critical structure called "three-grain bridge" which is located between two denser regions in the powder compact, as shown in Fig. 5.3. Then de-sintering process of "three-grain bridge" was described in detail in Lange's follow-up study [61, 62]. Unlike the de-sintering in constrained sintering which starts with a sintered body, de-sintering of three-grain bridge in the powder compact is concurrent with densification. In addition, unlike the de-sintering in constrained sintering which is caused by morphological instability, de-sintering of three-grain bridge in the powder compact is partially due to the inhomogeneity of sintering variables and external tensile stress. The denser regions apply the tensile stress to three-grain bridge that increases the aspect ratio of three-grain bridge, hence increasing morphological instability and then partially leading to de-sintering. However, effects of inhomogeneity on de-sintering and its working mechanism are not mentioned in Lange's study.
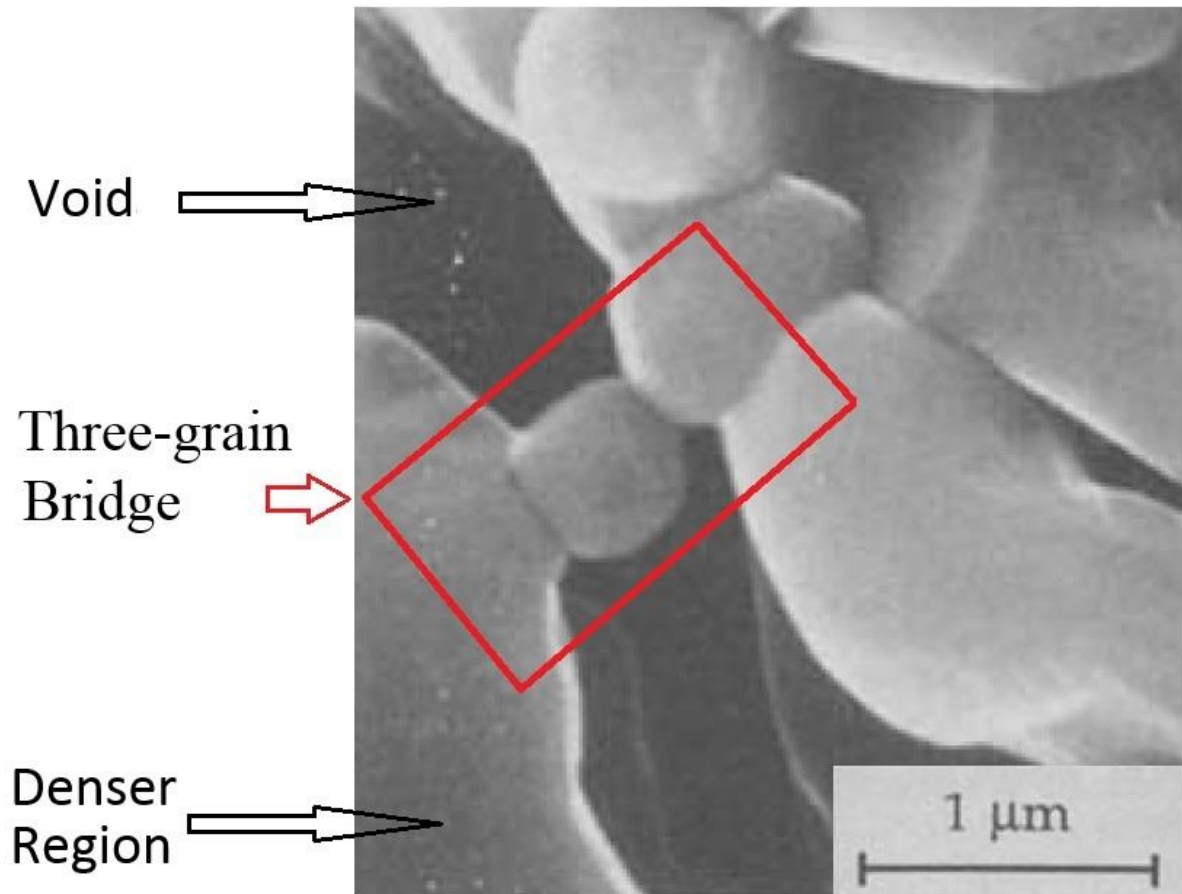
Fig. 5.3 The three-grain bridge located between two denser regions in the powder compact [60].

Purposes of This Chapter

The purposes of this chapter are to (a) present a simple and definitive case for understanding the effects of inhomogeneity on sintering kinetics as well as its working mechanism, (b) observe the evolution of the grain boundary during sintering with considering fast surface diffusion, and (c) qualify and quantify the effects of sintering variables' inhomogeneity.

In this study, a geometry of three-grain bridge shown in Fig. 5.3 is adopted. In addition to that, the co-sintering problem of three spherical particles is solved by employing a similar numerical method of chapter 2.

The upper and lower particles of three-grain bridge are fixed, and the middle particle is free to move. The direction of its movement is used to describe the sintering kinetics under the effects of inhomogeneity. If the middle particle moves towards the upper particle, a sintering process happens between them, when a de-sintering process happens between the lower particle and the middle particle.

5.2 Methodology

5.2.1 Assumption of Geometry and Sintering Variables

Three spherical particles of different sizes are considered as shown in Fig. 5.4(a), and it is sintered by coupled surface diffusion and grain-boundary diffusion. In the figure, R represents the radius of the particle; a is the neck size. A cylindrical coordinate (r, z) is used. A grain boundary is assumed as the straight and the neck that grow along the grain boundary. Additionally, particle 1 and particle 3 are fixed, while particle 2 is free to move with velocity $V_{(2)}$.

The definition of material parameters is the same as chapter 2, shown in Fig. 5.4(b). In the figure, $\mathcal{D}_{gb}$ is grain-boundary diffusivity; $\mathcal{D}_s$ is free surface diffusivity; γ_s is surface tension; γ_{gb} is grain-boundary tension and θ is the dihedral angle at the triple junction.

Finally, all sintering variables used in this chapter are listed as follows.

(a) Particles radius: R_1, R_2, R_3

(b) Neck size: a_1, a_2

(c) Surface diffusion coefficient: $\mathcal{D}_{s(1)}$, $\mathcal{D}_{s(2)}$, $\mathcal{D}_{s(3)}$

(d) Grain-boundary diffusion coefficient: $\mathcal{D}_{gb(1)}$, $\mathcal{D}_{gb(2)}$

(e) Dihedral angle: θ_1, θ_2

(f) Surface tension: $\gamma_{s(1)}$, $\gamma_{s(2)}$

(g) Grain-boundary tension: $\gamma_{gb(1)}$, $\gamma_{gb(2)}$
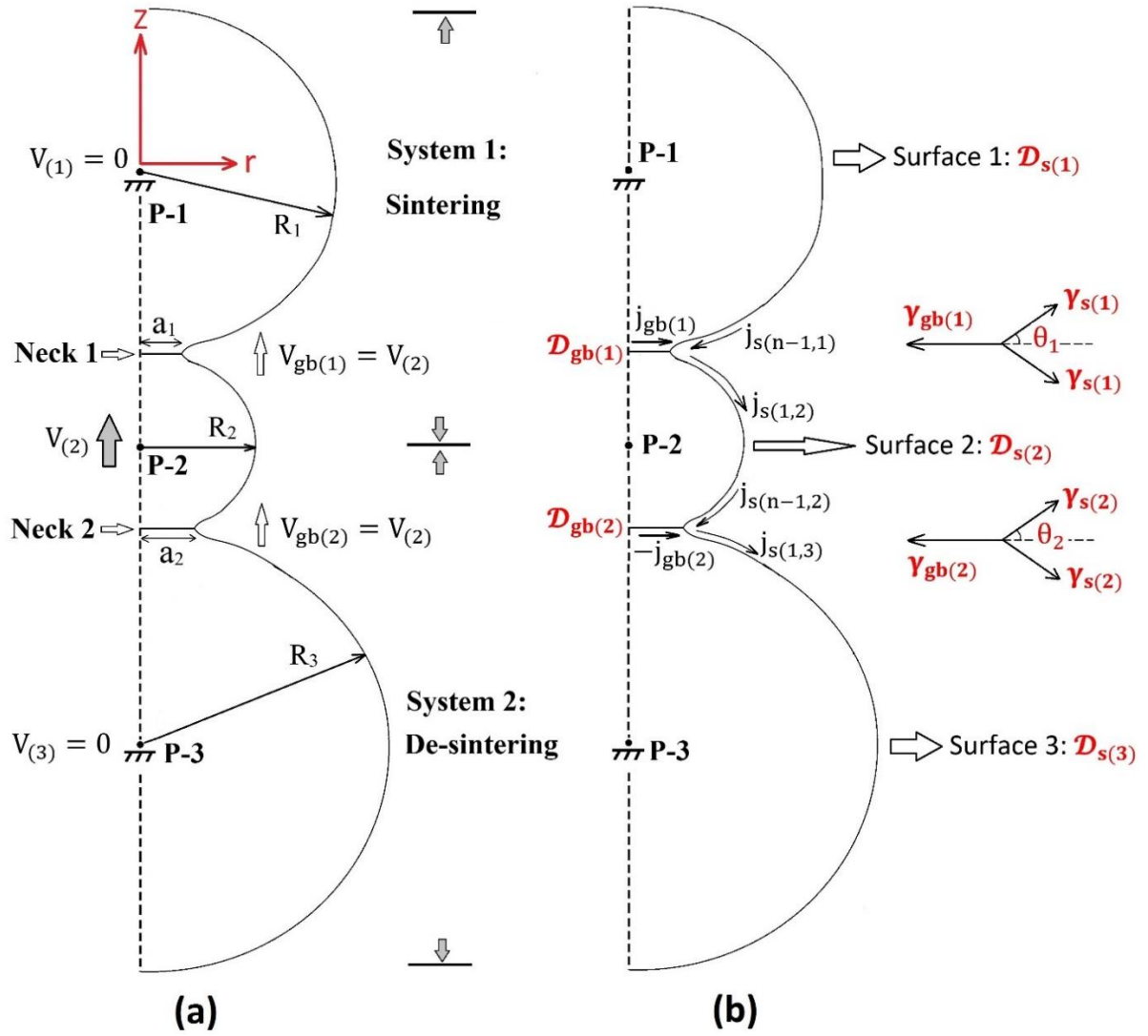
Fig. 5.4 Assumption of geometry and sintering variables

5.2.2 Governing Equations and Their Numerical Solutions

According to Fick's laws, the diffusive flux j is linearly dependent on the gradient of chemical potential µ regarding the diffusion atoms:

$$j = -\frac{D\delta}{kT}\frac{\partial \mu}{\partial s} \tag{5.1}$$

where D is diffusivity; δ is the thickness of the diffusion layer; k is Boltzmann's constant; T is the sintering temperature and s is the local coordinate along the diffusion path.

5.2.2.1 Grain-boundary Diffusion

On the grain boundary, the chemical potential is related to the stress σ normal to the grain boundary through

$$\mu = -\Omega\sigma \tag{5.2}$$

where Ω is the atomic volume. Substituting Eq. (5.2) into Eq. (5.1) leads to

$$j_{gb} = \mathcal{D}_{gb}\frac{\partial\sigma}{\partial r} \tag{5.3}$$

in which an effective grain-boundary diffusivity has been introduced as

$$\mathcal{D}_{gb} = \frac{D_{gb}\delta_{gb}\Omega}{kT} \tag{5.4}$$

where D_{gb} is grain-boundary diffusivity and δ_{gb} is the thickness of the grain-boundary diffusion layer.

(1) Neck 1

As shown in Fig. 5.4(a), particle 2 approaches to particle 1 with a speed of $V_{(2)}$, and hence the grain boundary of neck 1 obtains velocity $V_{gb(1)}$, where $V_{gb(1)}$ equals to $V_{(2)}$. As shown in Fig. 5.5(a), grain-boundary diffusion $j_{gb(1)}$ flows through the grey ring and then becomes $j_{gb(1)}{}'$. Consequently, this process leads to a vertical speed $V_{gb(1)}$. Defining the grey ring as a unit to satisfy mass conservation at neck 1, there is

$$V_{gb(1)} * 2\pi r * \Delta r = j'_{gb(1)} * [2\pi(r + \Delta r)] - j_{gb(1)} * 2\pi r \tag{5.5}$$

When $\Delta x \to 0$, then there is

$$V_{gb(1)} = \frac{\partial j_{gb(1)}}{\partial r} + \frac{j_{gb(1)}}{r} \tag{5.6}$$

According to the product rule, there is

$$V_{gb(1)} = \frac{1}{r} * \frac{\partial(rj_{gb(1)})}{\partial r} \tag{5.7}$$

An approximate solution can be proposed as follows.

$$\hat{j}_{gb(1)} = Ar + B \quad \Rightarrow \quad r * \hat{j}_{gb(1)} = Ar^2 + Br \quad \Rightarrow \quad \frac{\partial(r\hat{j}_{gb(1)})}{\partial r} = 2Ar + B \tag{5.8}$$

When r=0, $\hat{j}_{gb(1)} = 0$. The value of B is easily derived and equal to 0. Hence,

$$\left.\begin{array}{l} \hat{j}_{gb(1)}=Ar \\ \frac{\partial (r\hat{j}_{gb(1)})}{\partial r}=2Ar \end{array}\right\} \Rightarrow \frac{\partial (r\hat{j}_{gb(1)})}{\partial r} = 2\hat{j}_{gb(1)} \tag{5.9}$$

When substituting Eq. (5.9) into Eq. (5.7), the expression for the grain-boundary flux $j_{gb(1)}$ can be obtained as

$$j_{gb(1)} = \frac{1}{2}V_{gb(1)} * r \tag{5.10}$$

When substituting Eq. (5.10) into Eq. (5.3), after integration, normal stress σ_1 at neck 1 can be found as

$$\sigma_1 = \frac{1}{4\mathcal{D}_{gb(1)}}V_{gb(1)}r^2 + C_1 \tag{5.11}$$

where C_1 is an integration constant to be determined.
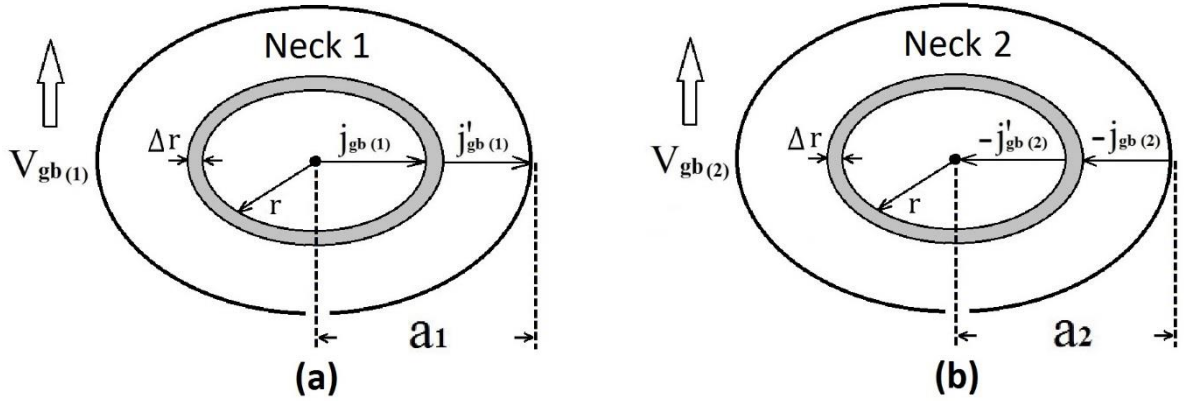
Fig. 5.5 The schematic diagram for mass conservation at (a) neck 1 and (b) neck 2

(2) Neck 2

Similarly, particle 2 is away from particle 3 with a speed of $V_{(2)}$, and hence the grain boundary of neck 2 obtains velocity $V_{gb(2)}$, where $V_{gb(2)}$ equals to $V_{(2)}$. As shown in Fig. 5.5(b), grain-boundary diffusion $j_{gb(2)}$ flows through the grey ring and then becomes $j_{gb(2)}'$. Consequently, this process leads to vertical speed $V_{gb(2)}$. When defining the grey ring as a unit, to satisfy mass conservation at neck 2, there is

$$V_{gb(2)} * 2\pi r * \Delta r = -j_{gb(2)}' * [2\pi(r + \Delta r)] - (-j_{gb(2)} * 2\pi r) \tag{5.12}$$

After a similar derivation, the expression for the grain-boundary flux $j_{gb(2)}$ and normal stress σ_2 can be found as

$$j_{gb(2)} = -\frac{1}{2}V_{gb(2)} * r \tag{5.13}$$

and

$$\sigma_2 = -\frac{1}{4\mathcal{D}_{gb(2)}}V_{gb(2)}r^2 + C_2 \tag{5.14}$$

where C_2 is an integration constant to be determined.

5.2.2.2 Surface Diffusion

On the particle surface, the chemical potential is related to the principal curvature κ :

$$\mu = -\Omega\gamma_s\kappa \tag{5.15}$$

where γ_s is the surface free energy; κ is the principal curvature of the free surface. Substituting Eq. (5.15) into Eq. (5.1) leads to

$$j_s = \mathcal{D}_s\frac{\partial\kappa}{\partial s} \tag{5.16}$$

in which the effective surface diffusivity has been introduced as

$$\mathcal{D}_s = \frac{D_s\delta_s\Omega\gamma_s}{kT} \tag{5.17}$$

where D_s is surface diffusivity and δ_s is the thickness of the diffusion layer.

To derive the expression for surface migration velocity V_s with the finite difference method, the geometry of this model is meshed as shown in Fig. 5.6. In the figure, the profile of three particles is composed of many discrete nodes (N point), and then κ and V_s are defined on the N point. Furthermore, the M point is used for bisecting two neighbouring N points, and then j_s is defined on the M point.

In this discrete-node system, according to Eq. (5.16), the surface diffusive flux at any M point is obtained as

$$j_{s(i)} = \mathcal{D}_s\frac{\kappa_{(i+1)}-\kappa_i}{\Delta S_i} \tag{5.18}$$

where κ_i is the principal curvature and ΔS_i is the distance between two neighbouring M points. Apart from the triple junction, the principal curvature at the N point is defined as the sum of the maximum curvature and the minimum curvature, and it is negative for the convex surface.
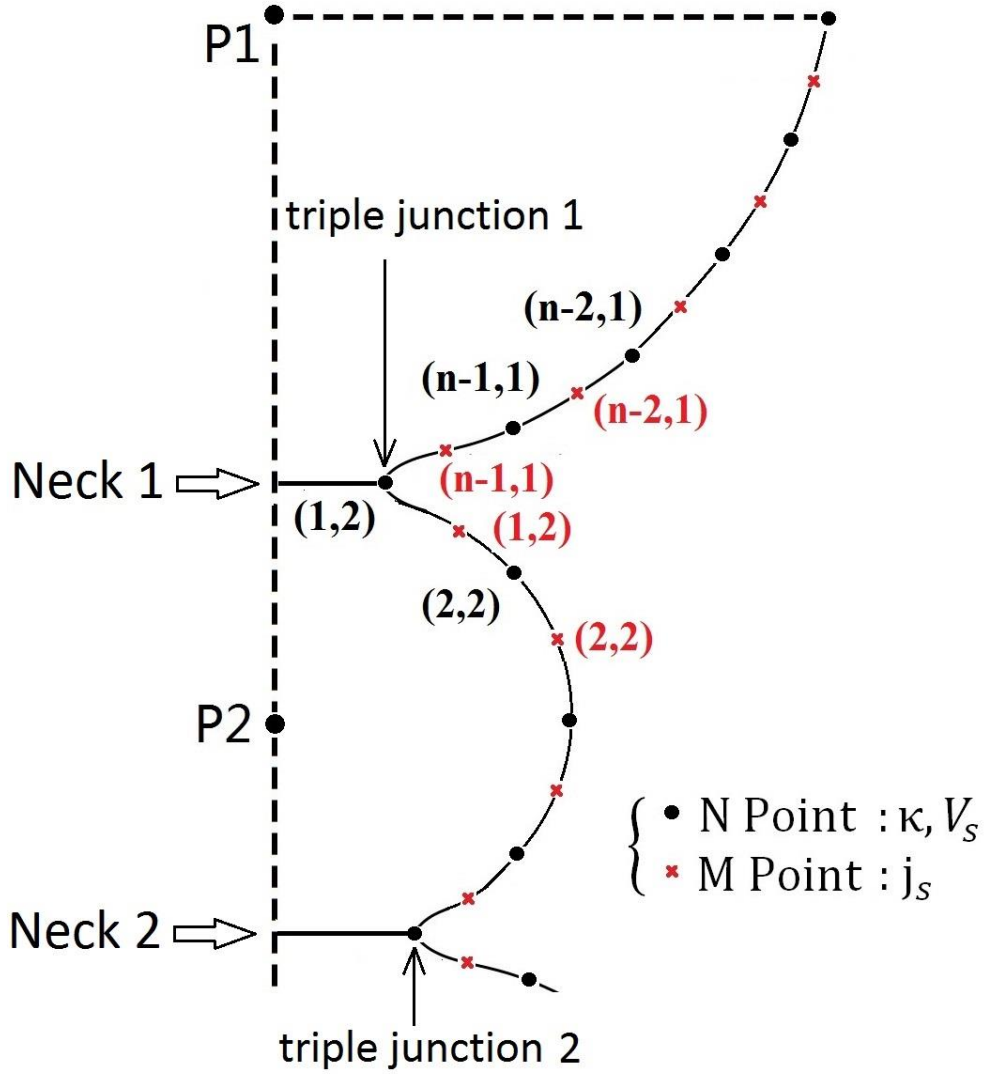
Fig. 5.6 The schematic diagram for meshing geometry

In addition, mass conservation provides a relation between the surface migration velocity V_s and the surface diffusion flux j_s, as shown in Fig. 5.7. To satisfy mass conservation at the shadow area, there is

$$j_{s(i)} * 2\pi r_{(i)} - j_{s(i-1)} * 2\pi r_{(i-1)} = V_{s(i)} * A_s \tag{5.19}$$

where A_s is the shadow area.

Finally, there is

$$V_{s(i)} = \frac{2\pi * (j_{s(i)} * r_{(i)} - j_{s(i-1)} * r_{(i-1)})}{A_s}$$ (5.20)

Except for the triple junction, the surface diffusion flux j_s and the surface migration velocity V_s can be calculated with Eq. (5.18) and Eq. (5.20) respectively.
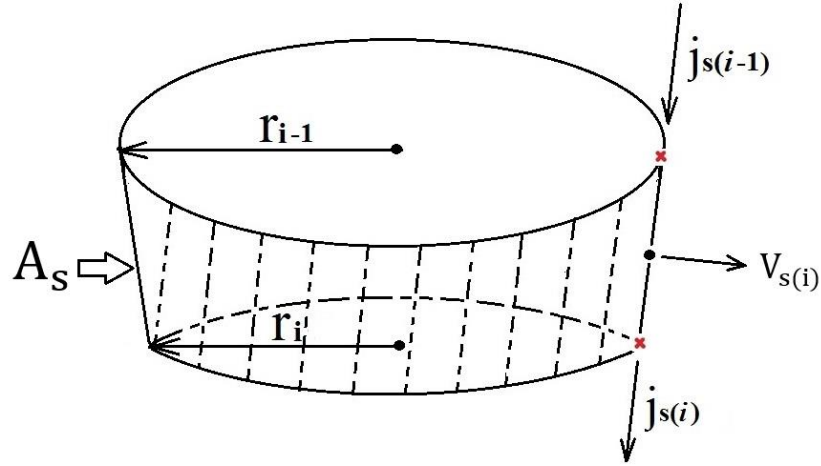
Fig. 5.7 The schematic diagram for mass conservation on the free surface

5.2.2.3 Continuity Conditions at Triple Junctions

(1) Mass conservation is satisfied at the junction.

As shown in Fig. 5.4(b), at triple junction 1, mass conservation requires

$$\dot{j}_{gb(1)} = \dot{j}_{s(1,2)} - \dot{j}_{s(n-1,1)}$$ (5.21)

As shown in Fig. 5.4(b), at triple junction 2, mass conservation requires

$$\dot{j}_{gb(2)} = \dot{j}_{s(n-1,2)} - \dot{j}_{s(1,3)}$$ (5.22)

(2) The chemical potential is continuous at the junction.

The chemical potential must be continuous at the junction. If not, there would be the unbounded flux at the junction.

For triple junction 1, there is

$$\mu_1 = -\Omega\,\sigma_{tip(1)} = -\Omega\gamma_{s(1)}\kappa_{tip(1)} \quad \Rightarrow \quad \sigma_{tip(1)} = \gamma_{s(1)}\kappa_{tip(1)}$$ (5.23)

For triple junction 2, there is

$$\mu_2 = -\Omega \, \sigma_{tip(2)} = -\Omega \gamma_{s(2)} \kappa_{tip(2)} \quad \Rightarrow \quad \sigma_{tip(2)} = \gamma_{s(2)} \kappa_{tip(2)} \tag{5.24}$$

(3) Equilibrium of surface tension γ_s and grain-boundary tension γ_{gb} at the triple junction is presented.

As shown in Fig. 5.4(b), surface tension γ_s and grain-boundary tension γ_{gb} must be in equilibrium at the junction.

For triple junction 1, there is

$$\cos \theta_{(1)} = \frac{\gamma_{gb(1)}}{2\gamma_{s(1)}} \tag{5.25}$$

For triple junction 2, there is

$$\cos \theta_{(2)} = \frac{\gamma_{gb(2)}}{2\gamma_{s(2)}} \tag{5.26}$$

5.2.2.4 Global Equilibrium of Force

When drawing the free body diagram of particle 2, force analysis is illustrated in Fig. 5.8. The expression of force balance is as follows.

$$2\pi a_1 \gamma_{s(1)} \sin \theta_1 + \int_0^{a_1} (\sigma_1) 2\pi r dr = 2\pi a_2 \gamma_{s(2)} \sin \theta_2 + \int_0^{a_2} (\sigma_2) 2\pi r dr \tag{5.27}$$

When substituting Eq. (5.11) and Eq. (5.14) into Eq. (5.27), there is

$$2\pi a_1 \gamma_{s(1)} \sin \theta_1 + \frac{1}{8 \mathcal{D}_{gb(1)}} V_{gb(1)} a_1^4 + C_1 a_1^2$$

$$= 2\pi a_2 \gamma_{s(2)} \sin \theta_2 - \frac{1}{8 \mathcal{D}_{gb(2)}} V_{gb(2)} a_2^4 + C_2 a_2^2 \tag{5.28}$$

For triple junction 1, $r = a_1$. When substituting $r = a_1$ into Eq. (5.11), there is

$$\sigma_1 = \frac{1}{4 \mathcal{D}_{gb(1)}} V_{gb(1)} a_1^2 + C_1 \tag{5.29}$$

At triple junction 1, $\sigma_1 = \sigma_{tip(1)}$. When substituting Eq. (5.23) and Eq. (5.29) into $\sigma_1 = \sigma_{tip(1)}$, there is

$$C_1 = \gamma_{s(1)}\kappa_{tip(1)} - \frac{1}{4\mathcal{D}_{gb(1)}}V_{gb(1)}a_1^2 \tag{5.30}$$

For triple junction 2, $r = a_2$. When substituting $r = a_2$ into Eq. (5.14), there is

$$\sigma_2 = -\frac{1}{4\mathcal{D}_{gb(2)}}V_{gb(2)}a_2^2 + C_2 \tag{5.31}$$

At triple junction 2, $\sigma_2 = \sigma_{tip(2)}$. When substituting Eq. (5.24) and Eq. (5.31) into $\sigma_2 = \sigma_{tip(2)}$, there is

$$C_2 = \gamma_{s(2)}\kappa_{tip(2)} + \frac{1}{4\mathcal{D}_{gb(2)}}V_{gb(2)}a_2^2 \tag{5.32}$$

As shown in Fig. 5.4(a), $V_{gb(1)} = V_{gb(2)} = V_{(2)}$. When substituting Eq. (5.30) and Eq. (5.32) into Eq. (5.28), there is

$$V_{(2)} = \frac{8\left[a_1^2\gamma_{s(1)}\kappa_{tip(1)} - a_2^2\gamma_{s(2)}\kappa_{tip(2)}\right] + 16\left[a_1\gamma_{s(1)}\sin\theta_1 - a_2\gamma_{s(2)}\sin\theta_2\right]}{\frac{a_1^4}{\mathcal{D}_{gb(1)}} + \frac{a_2^4}{\mathcal{D}_{gb(2)}}} \tag{5.33}$$
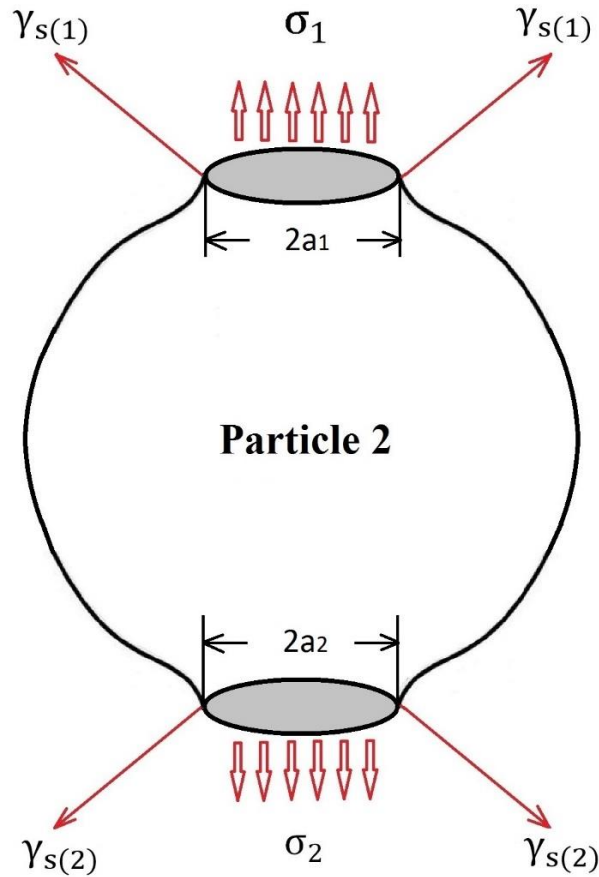

Fig. 5.8 The free body diagram of particle 2

5.2.2.5 Completing Governing Equations and Solving κ_{tip}

For triple junction 1, $r = a_1$ and $V_{gb(1)} = V_{(2)}$. When substituting Eq. (5.10) and Eq. (5.18) into Eq. (5.21), there is

$$V_{(2)} = \frac{2}{a_1} \left\{ \left[\frac{\mathcal{D}_{s(1)}\kappa_{(n-1,1)}}{\Delta S_{(n-1,1)}} + \frac{\mathcal{D}_{s(2)}\kappa_{(2,2)}}{\Delta S_{(1,2)}} \right] - \left[\frac{\mathcal{D}_{s(1)}}{\Delta S_{(n-1,1)}} + \frac{\mathcal{D}_{s(2)}}{\Delta S_{(1,2)}} \right] * \kappa_{tip(1)} \right\} \tag{5.34}$$

For triple junction 2, $r = a_2$ and $V_{gb(2)} = V_{(2)}$. When substituting Eq. (5.13) and Eq. (5.18) into Eq. (5.22), there is

$$V_{(2)} = \frac{2}{a_2} \left\{ \left[\frac{\mathcal{D}_{s(2)}\kappa_{(n-1,2)}}{\Delta S_{(n-1,2)}} + \frac{\mathcal{D}_{s(3)}\kappa_{(2,3)}}{\Delta S_{(1,3)}} \right] - \left[\frac{\mathcal{D}_{s(2)}}{\Delta S_{(n-1,2)}} + \frac{\mathcal{D}_{s(3)}}{\Delta S_{(1,3)}} \right] * \kappa_{tip(2)} \right\} \tag{5.35}$$

For easier derivation, some temporary terms are used to replace constant terms in Eq. (5.33), Eq. (5.34) and Eq. (5.35) as follows.

In Eq. (5.34), $A_1 = \frac{\mathcal{D}_{s(1)}\kappa_{(n-1,1)}}{\Delta S_{(n-1,1)}} + \frac{\mathcal{D}_{s(2)}\kappa_{(2,2)}}{\Delta S_{(1,2)}}$ and $B_1 = \frac{\mathcal{D}_{s(1)}}{\Delta S_{(n-1,1)}} + \frac{\mathcal{D}_{s(2)}}{\Delta S_{(1,2)}}$.

In Eq. (5.35), $A_2 = \frac{\mathcal{D}_{s(2)}\kappa_{(n-1,2)}}{\Delta S_{(n-1,2)}} + \frac{\mathcal{D}_{s(3)}\kappa_{(2,3)}}{\Delta S_{(1,3)}}$ and $B_2 = \frac{\mathcal{D}_{s(2)}}{\Delta S_{(n-1,2)}} + \frac{\mathcal{D}_{s(3)}}{\Delta S_{(1,3)}}$.

In Eq. (5.33), $A_3 = a_1 \gamma_{s(1)} \sin\theta_1 - a_2 \gamma_{s(2)} \sin\theta_2$, $A_4 = \frac{a_1^4}{\mathcal{D}_{gb(1)}} + \frac{a_2^4}{\mathcal{D}_{gb(2)}}$, $B_3 = a_1^2 \gamma_{s(1)}$ and $B_4 = a_2^2 \gamma_{s(2)}$.

Then Eq. (5.33), Eq. (5.34) and Eq. (5.35) are simplified as follows.

$$V_{(2)} = \frac{8[B_3 \kappa_{tip(1)} - B_4 \kappa_{tip(2)}] + 16A_3}{A_4} \tag{5.36}$$

$$V_{(2)} = \frac{2}{a_1}(A_1 - B_1 \kappa_{tip(1)}) \tag{5.37}$$

$$V_{(2)} = \frac{2}{a_2}(A_2 - B_2 \kappa_{tip(2)}) \tag{5.38}$$

Three unknown variables $\kappa_{tip(1)}$, $\kappa_{tip(2)}$ and $V_{(2)}$ are finally solved through Eq. (5.36), Eq. (5.37) and Eq. (5.38). Therefore, governing equations of this model are complete and all variables are solved.

5.2.3 Update of the Particle Profile

In this model, particle 1 and 3 are fixed. Therefore, their profiles are only updated by the surface migration velocity V_S. Euler's method is used to describe the time step integration of the particle profile. Hence, new cylindrical coordinates (r, z) are expressed as follows.

$$r_{(t+\Delta t)} = r_t + V_S * n_r \Delta t$$

$$Z_{(t+\Delta t)} = Z_t + V_S * n_z \Delta t \tag{5.39}$$

and

$$\Delta t = \frac{\Delta S_m}{V_{max}} \tag{5.40}$$

where Δt is the time step; ΔS_m is the average of the distance between two nodes and V_{max} is the maximum value of V_S.

For particle 2, its profile is updated not only by the surface migration velocity V_S but also by moving velocity of particle 2 $V_{(2)}$, because particle 2 is free to move. Therefore, new cylindrical coordinates (r, z) of particle 2 are expressed as follows.

$$r_{(t+\Delta t)} = r_t + V_S * n_r \Delta t$$

$$Z_{(t+\Delta t)} = Z_t + V_S * n_z \Delta t + V_{(2)} * \Delta t$$
$$\tag{5.41}$$

and

$$\Delta t = \frac{\Delta S_m}{V_{max}} \tag{5.42}$$

where Δt is the time step; ΔS_m is the average of the distance between two nodes and V_{max} is the maximum value of V_S.

5.3 Effects of Inhomogeneity on Sintering Kinetics

In this section, effects of inhomogeneity on sintering kinetics are studied through analysing numerical results. The observation mainly concerns two aspects. To be specific, the first one is the direction of particle 2 movement under the effect of inhomogeneity, and the second one is neck evolution at two grain boundaries when considering fast surface diffusion.

Importantly, inhomogeneity is mainly reflected in six kinds of parameters which are listed as follows.

(a) Inhomogeneity of grain-boundary diffusion coefficient: $\mathcal{D}_{gb(1)}$, $\mathcal{D}_{gb(2)}$

(b) Inhomogeneity of surface diffusion coefficient: $\mathcal{D}_{s(1)}$, $\mathcal{D}_{s(2)}$, $\mathcal{D}_{s(3)}$

(c) Inhomogeneity of surface tension: $\gamma_{s(1)}$, $\gamma_{s(2)}$

(d) Inhomogeneity of initial neck size: a_1, a_2

(e) Inhomogeneity of particle radius: R_1, R_2, R_3

For diffusion coefficients of different grain boundaries, their inhomogeneity can be more than ten times due to a slight difference on the thickness of the diffusion layer and activation energy [63]. Similarly, for surface diffusion coefficients of different free surfaces, their inhomogeneity can be more than ten times too. For surface tension and grain-boundary tension, their inhomogeneity owing to nonuniform packing among particles can be several times [64]. For the initial neck size and the particle radius, their inhomogeneity can be simply and clearly understood by Fig. 5.3.

To study the effect of each parameter inhomogeneity on sintering kinetics, six corresponding cases are designed for numerical computation, and they are isothermal sintering at $1200^{\circ}C$. Furthermore, reference values are set for each kind of parameters. Reference values of $\mathcal{D}_{gb}$ and γ_s are the same as those used in chapter 2. To consider the effect of fast surface diffusion, the reference value of $\mathcal{D}_s$ is one hundred times of $\mathcal{D}_{gb}$. At last, all reference values are shown in table 5.1.

When presenting the results, time is normalised by the same characteristic time τ_g used in chapter 2; meanwhile, shrinkage between particles and neck growth is normalised by the reference value of the radius.

Table 5.1. Reference Values Used in This Numerical Study

Grain-boundary diffusion coefficient $\mathcal{D}_{gb}$	6.8531648×10^{-36} m^4s/kg
Surface diffusion coefficient $\mathcal{D}_s$	$100\ \mathcal{D}_{gb}$
Surface tension γ_s	$1.1\ J/m^2$
Particle radius R	$10^{-6}m$
Initial neck size a	$5\%\ R$
Dihedral angle θ	$130°$

5.3.1 Numerical Results

(1) Inhomogeneity of Grain-boundary Diffusion

In this case, the inhomogeneity of grain-boundary diffusion results from their different diffusion coefficients. Hence, the grain-boundary diffusion coefficient of neck 2 $\mathcal{D}_{gb(2)}$ is equal to the reference value in table 5.1, and the grain-boundary diffusion coefficient of neck 1 $\mathcal{D}_{gb(1)}$ is ten times of $\mathcal{D}_{gb(2)}$. The radius ratio of three particles, $R_1:R_2:R_3$, is 5:1:5, where R_2 is equal to the reference value. Furthermore, other parameters are equal to reference values.

Fig. 5.9 shows the shrinkage between two particles over time. The positive value represents two particles that are close to each other, while the negative value represents that they are away from each other. Two observations can be made from this figure:

(a) Particle 2 moves towards particle 1 due to the larger grain-boundary diffusion on neck 1, while away from particle 3.

(b) The effect of grain-boundary diffusion inhomogeneity on particle movement is extremely weak.

Fig. 5.10 shows the neck radius over time. Two observations can be made from this figure:

(a) Both neck 1 and neck 2 grow due to the backflow of fast surface diffusion on the triple-junction area, which is mentioned in chapter 2.

(b) The effect of grain-boundary diffusion inhomogeneity on neck growth can be ignored.
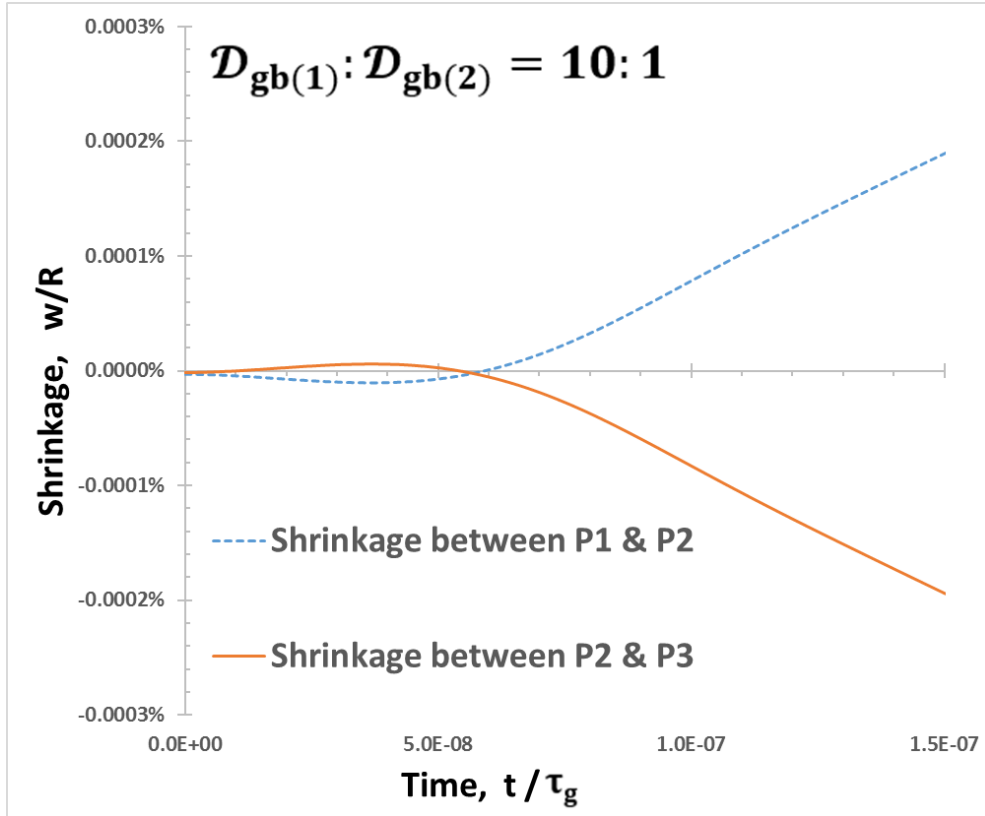
Fig. 5.9 Shrinkage between two particles over time for $\mathcal{D}_{gb(1)}:\mathcal{D}_{gb(2)} = 10:1$
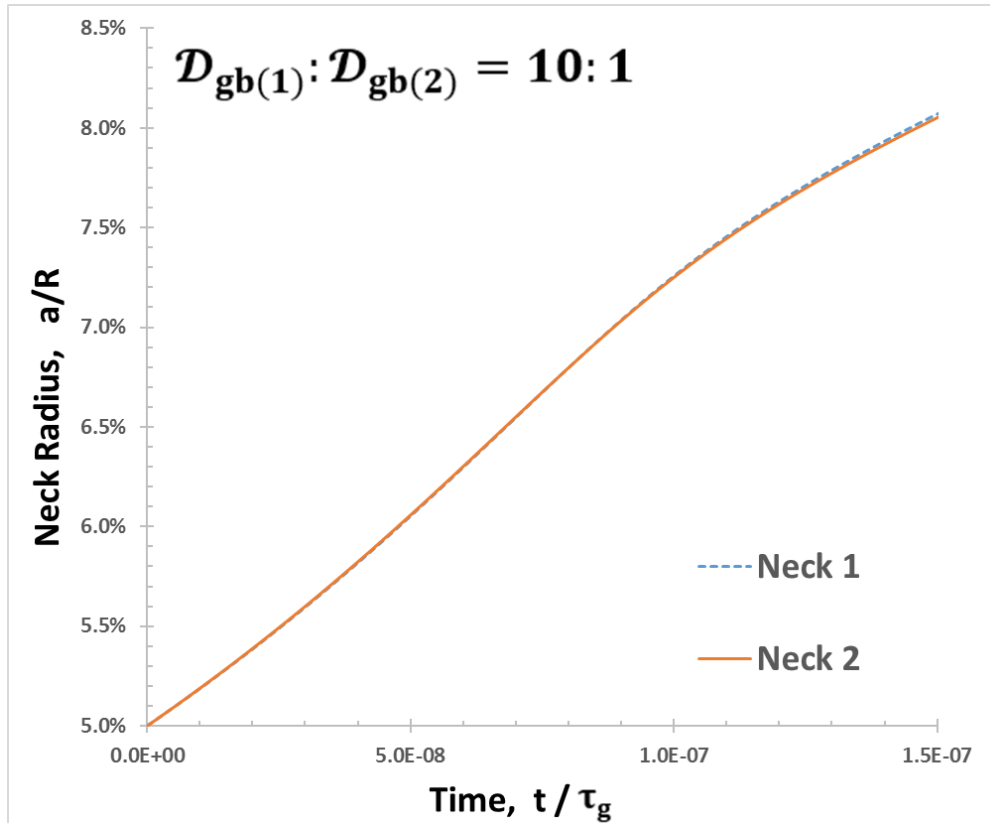
Fig. 5.10 The neck radius over time for $\mathcal{D}_{gb(1)}:\mathcal{D}_{gb(2)} = 10:1$

81

(2) Inhomogeneity of Surface Diffusion

In this case, the inhomogeneity of surface diffusion results from their different diffusion coefficients. Hence, diffusion coefficients of surface 2 and surface 3, and $\mathcal{D}_{s(2)}$ and $\mathcal{D}_{s(3)}$, are equal to reference values in table 5.1, and the diffusion coefficient of surface 1 $\mathcal{D}_{s(1)}$ is ten times of the reference value. The radius ratio of three particles, $R_1:R_2:R_3$, is 5:1:5 where R_2 is equal to the reference value. Furthermore, other parameters are equal to reference values.

Fig. 5.11 shows the shrinkage between two particles over time. Similar observations can be made from this figure:

(a) Particle 2 moves towards particle 1 due to the larger surface diffusion on surface 1, while away from particle 3.

(b) The effect of surface diffusion inhomogeneity on particle movement is extremely weak too.

Fig. 5.12 shows the neck radius over time. The same features as Fig. 5.10 are observed from this figure:

(a) Both neck 1 and neck 2 grow due to the backflow of fast surface diffusion.

(b) The effect of surface diffusion inhomogeneity on neck growth can be ignored.

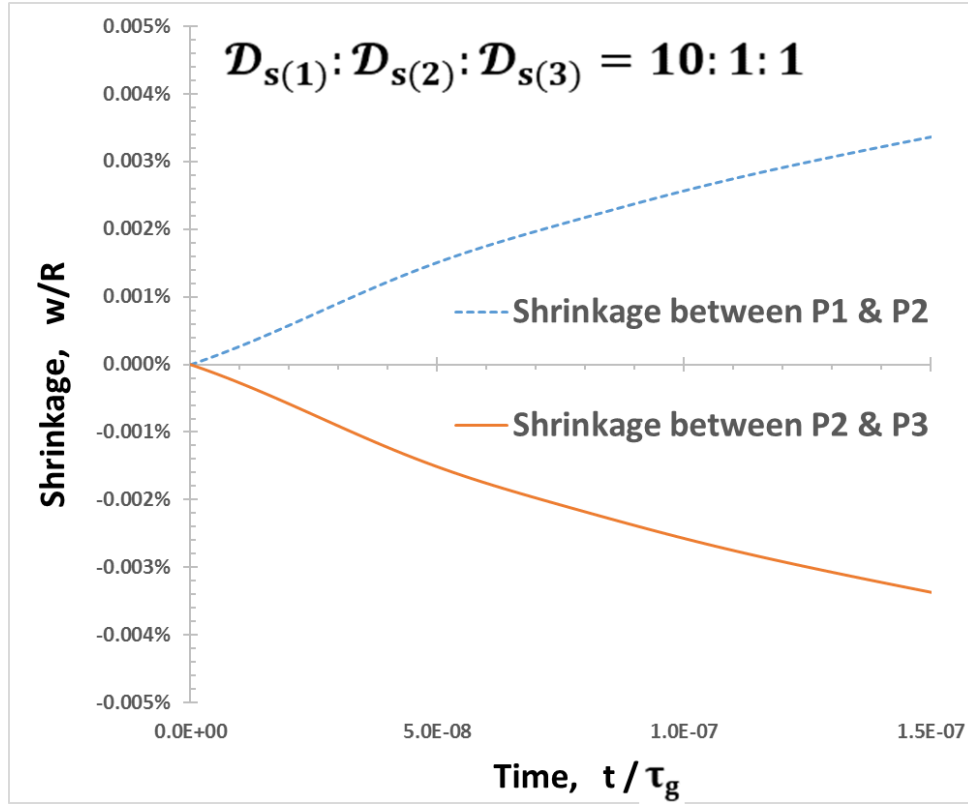**Fig. 5.11** Shrinkage between two particles over time for $\mathcal{D}_{s(1)}:\mathcal{D}_{s(2)}:\mathcal{D}_{s(3)} = 10:1:1$
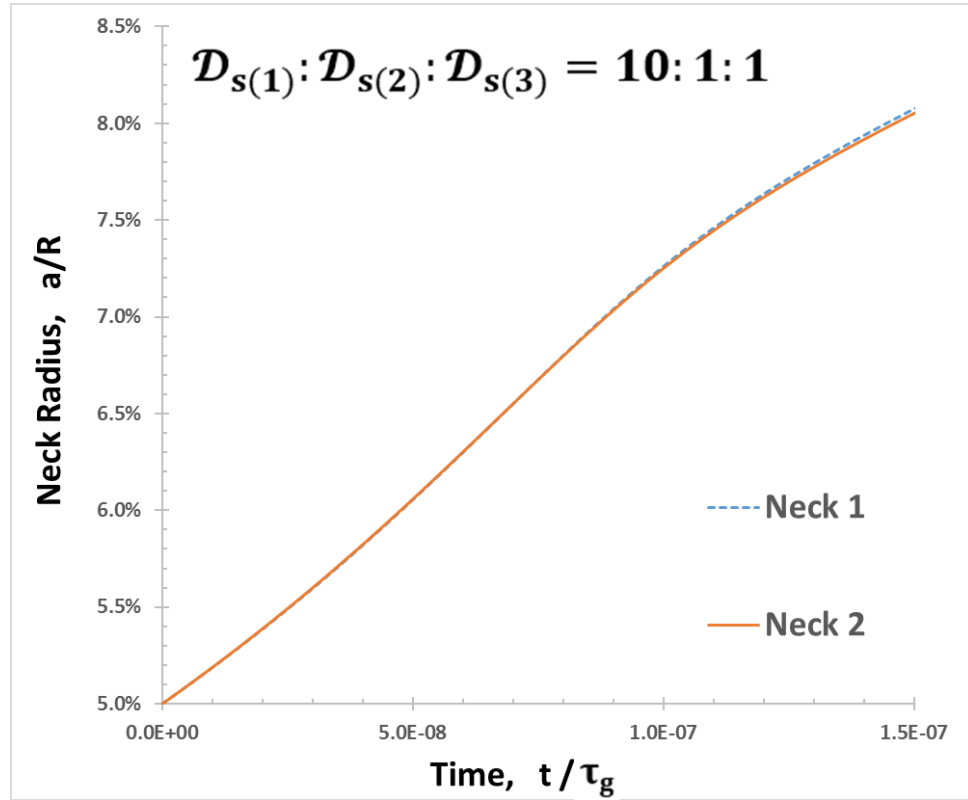
Fig. 5.12 The neck radius over time for $\mathcal{D}_{s(1)}:\mathcal{D}_{s(2)}:\mathcal{D}_{s(3)} = 10:1:1$

(3) Inhomogeneity of Surface Tension

In this case, the inhomogeneity results from different surface tension at triple junction 1 and triple junction 2. Hence, surface tension at triple junction 2 $\gamma_{s(2)}$ is equal to the reference value in table 5.1, and surface tension at triple junction 1 $\gamma_{s(1)}$ is ten times of $\gamma_{s(2)}$. The radius ratio of three particles, R_1:R_2: R_3, is 5:1:5, where R_2 is equal to the reference value. Furthermore, other parameters are equal to reference values.

Fig. 5.13 shows the shrinkage between two particles over time. Two observations can be made from this figure:

(a) Particle 2 moves towards particle 1 due to the larger surface tension at triple junction 1, while away from particle 3.

(b) Compared with the inhomogeneity of grain-boundary diffusion and surface diffusion, the effect of surface tension inhomogeneity on particle movement is noticeable.

Fig. 5.14 shows the neck radius over time. From this figure, observation can be made, and both necks are growing owing to the backflow of fast surface diffusion, and neck 1 grows faster than neck 2 because of the larger surface tension at triple junction 1.
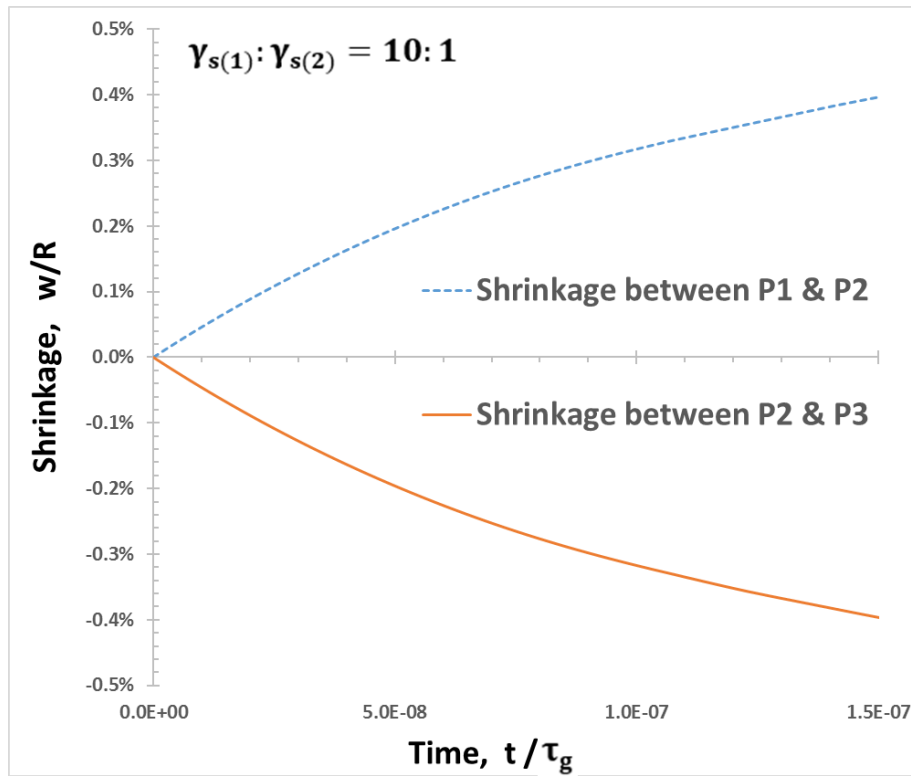
Fig. 5.13 Shrinkage between two particles over time for $\gamma_{s(1)}:\gamma_{s(2)} = 10:1$
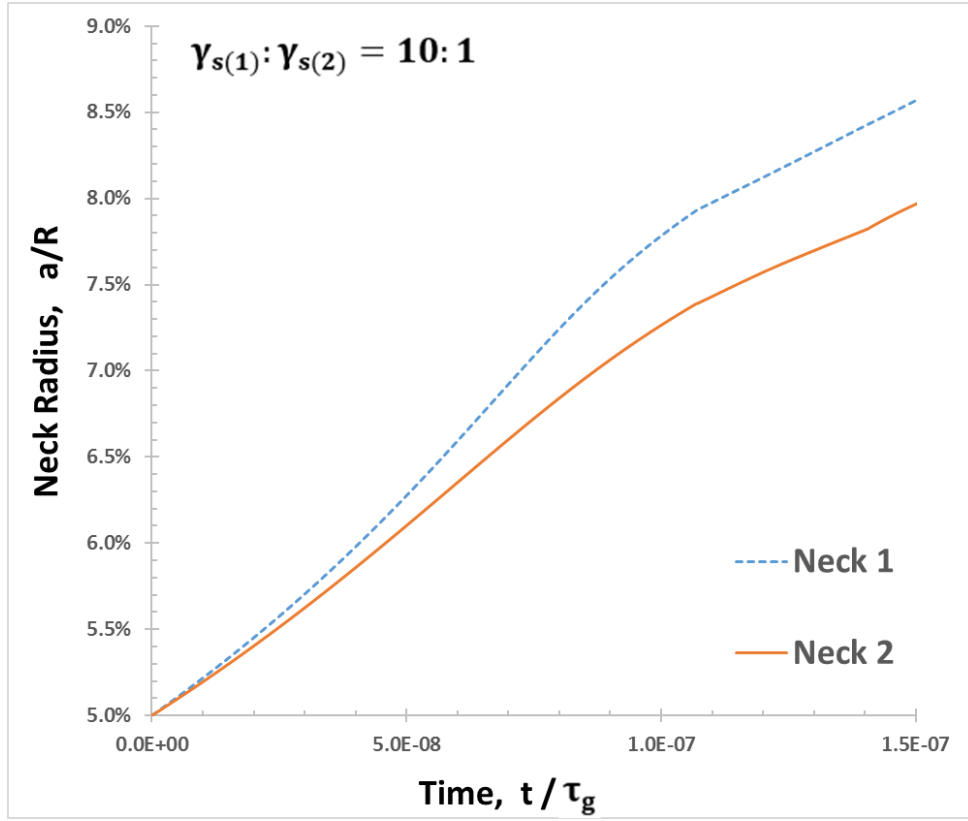
Fig. 5.14 The neck radius over time for $\gamma_{s(1)}:\gamma_{s(2)} = 10:1$

(4) Inhomogeneity of the Initial Neck Size

In this case, the inhomogeneity results from different initial sizes of neck 1 and neck 2. Hence, the initial size of neck 2 a_2 is equal to the reference value in table 5.1, and the initial size of neck 1 a_1 is twice of a_2. The radius ratio of three particles, $R_1:R_2:R_3$, is 5:1:5, where R_2 is equal to the reference value. Furthermore, other parameters are equal to reference values.

Fig. 5.15 shows the shrinkage between two particles over time. Two observations can be made from this figure:

(a) Particle 2 moves towards particle 1 due to a larger initial size of neck 1, while away from particle 3.

(b) The effect of initial neck size inhomogeneity on particle movement is obvious, but smaller than surface tension inhomogeneity.

Fig. 5.16 shows the neck radius over time. Similar observation can be made, and both necks are growing, while neck 1 grows faster than neck 2 due to its larger initial neck size.

85

Fig. 5.15 Shrinkage between two particles over time for $a_1 : a_2 = 2{:}1$
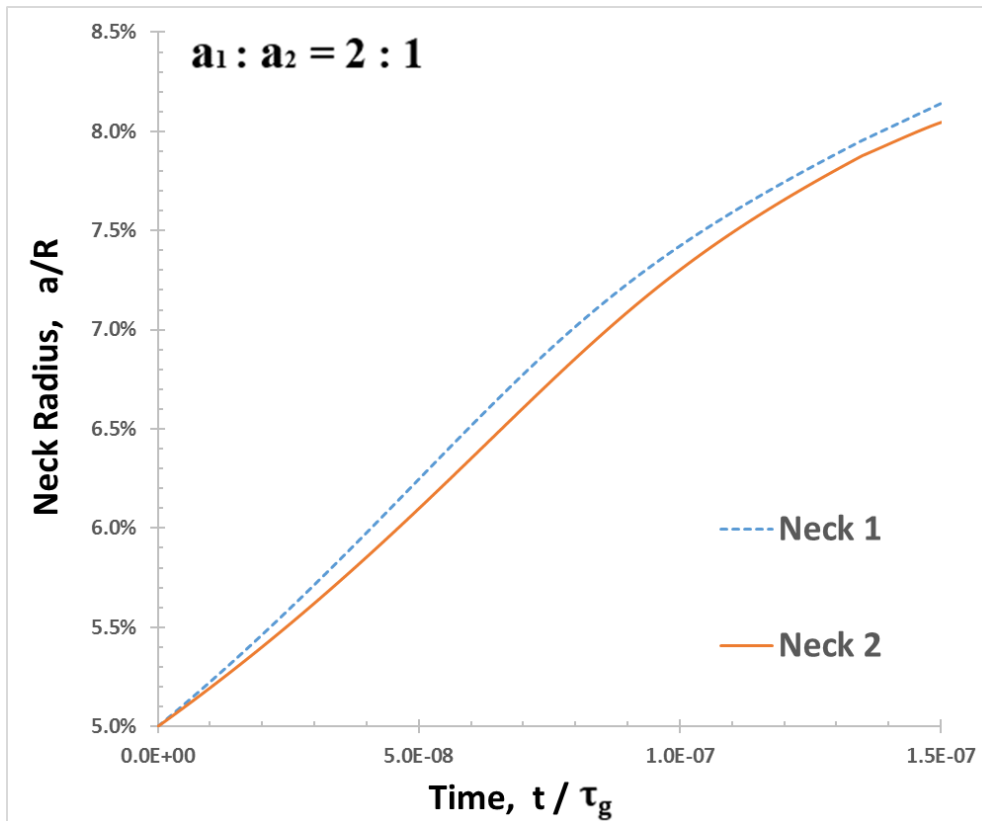
Fig. 5.16 The neck radius over time for $a_1 : a_2 = 2{:}1$

(5) Inhomogeneity of the Particle Size

In this case, the inhomogeneity results from the difference of particle sizes. Hence, the radius ratio of three particles, $R_1:R_2:R_3$, is 2:1:10, where R_2 is equal to the reference value. Furthermore, other parameters are equal to reference values.

Fig. 5.17 shows the shrinkage between two particles over time. Two observations can be made from this figure:

(a) Particle 2 moves towards particle 3 due to its larger radius, while away from particle 1.

(b) The effect of particle size inhomogeneity on particle movement is moderate.

Fig. 5.18 shows the neck radius over time. The observation can be made, and both necks are growing, and neck 2 grows faster than neck 1 due to a larger grain size of particle 3.
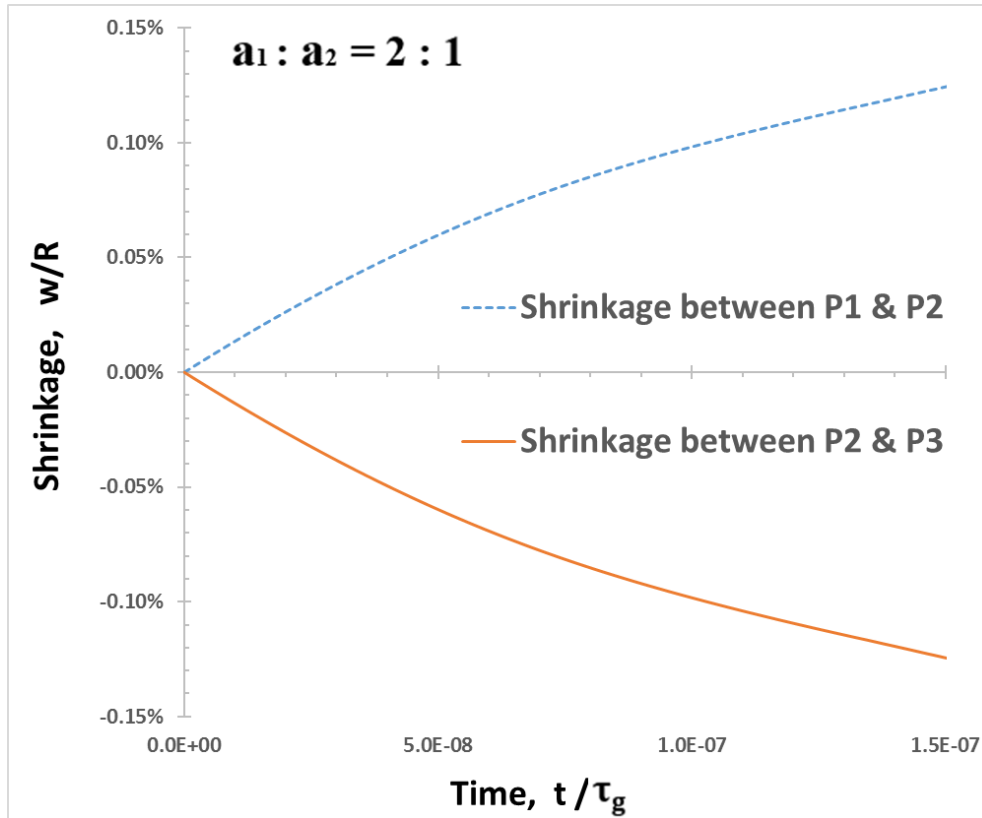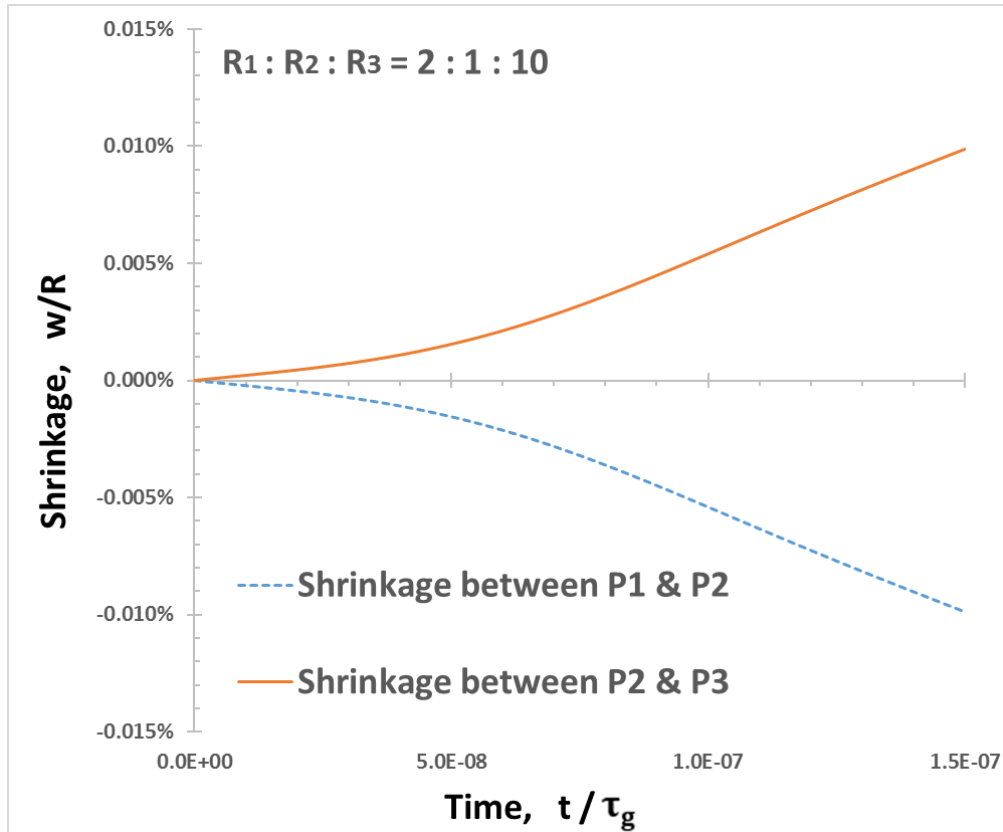

Fig. 5.17 Shrinkage between two particles over time for $R_1:R_2:R_3 = 2:1:10$
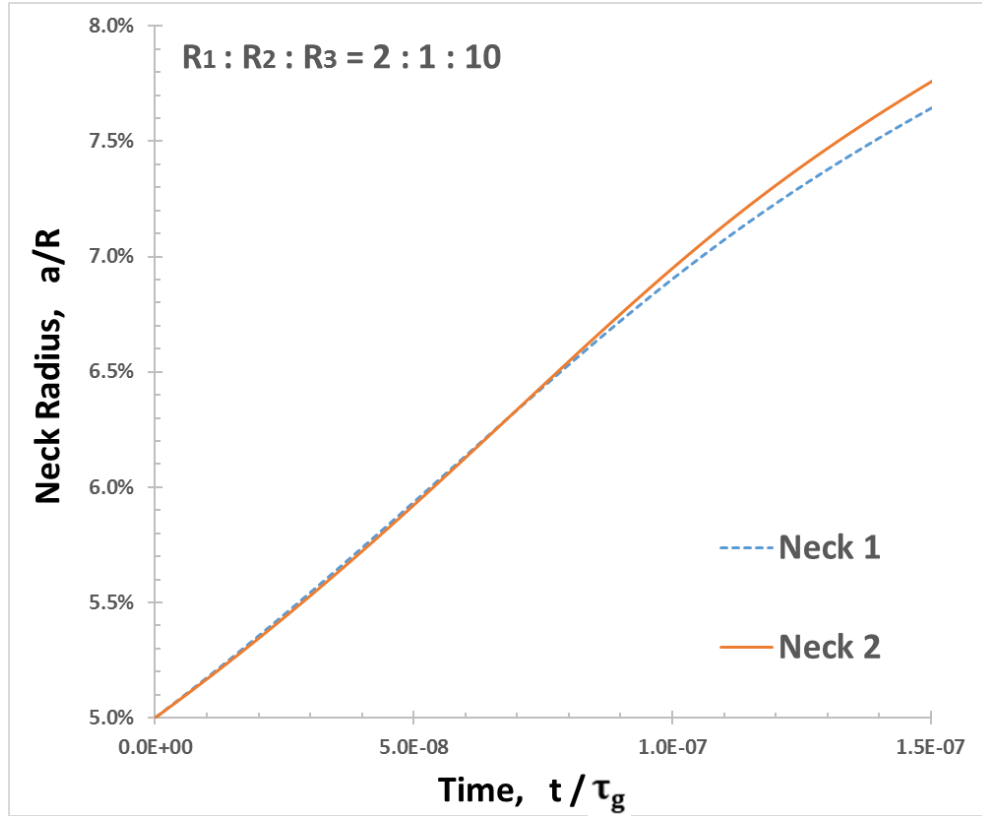
Fig. 5.18 The neck radius over time for R_1:R_2: R_3 =2:1:10

5.4 Summary of This Chapter

In this chapter, a further numerical study on the effects of inhomogeneity on sintering kinetics is presented by observing a de-sintering phenomenon on "three-grain bridge" during sintering. The effects of different sintering variables' inhomogeneity are examined by simulating a series of cases. From the above results, conclusions can be obtained as follows.

(a) The middle particle (particle 2) moves towards the particle featured with larger sintering variables.

(b) Effects of some variables' inhomogeneity such as surface tension, the dihedral angle and the initial neck size on sintering kinetics are obvious, while effects of other variables such as surface diffusivity are weak.

For these two features, a straightforward explanation is given as follows by analysing the equation of $V_{(2)}$ [Eq. (5.33)].

$$V_{(2)} = \frac{8\left[a_1^2\gamma_{s(1)}\kappa_{tip(1)} - a_2^2\gamma_{s(2)}\kappa_{tip(2)}\right] + 16\left[a_1\gamma_{s(1)}\sin\theta_1 - a_2\gamma_{s(2)}\sin\theta_2\right]}{\dfrac{a_1^4}{\mathcal{D}_{gb(1)}} + \dfrac{a_2^4}{\mathcal{D}_{gb(2)}}}$$

From this equation, the conclusion (a) can be clearly explained if the sintering variable of neck 1 such as $\gamma_{s(1)}$ is larger, and then particle 2 will get a positive velocity moving towards particle 1.

For conclusion (b), its understanding is surface tension γ_s featured with a large weight, and every term in the numerator is multiplied by γ_s. Hence, the effect of surface tension inhomogeneity on sintering kinetics is significant. Similarly, for inhomogeneity of the dihedral angle and the initial neck size, their roles in sintering kinetics can be explained as mentioned above. However, for other parameters, the effects of inhomogeneity are only reflected in the curvature κ_{tip} at the triple junction, and their weight in the equation is relatively small.

Noticeably, no matter which direction particle 2 moves towards, both neck 1 and neck 2 grow owing to the backflow of fast surface diffusion, which means neck growth is mainly controlled by the backflow of fast surface diffusion. This phenomenon once again proves that the previous assumption of fast surface diffusion is invalid for initial sintering of typical ceramic powders under practical sintering conditions.

Chapter 6 Concluding Remarks

6.1 Conclusions

Computer modelling of sintering at particle scale is the fundamental and essential way of understanding sintering behaviours and connecting sintering behaviours to sintering variables. Especially at particle scale, computational models provide a straightforward understanding of sintering in terms of the driving forces, the mechanisms, and the influence of major sintering variables such as the particle size, temperature and applied pressure. Only if these sintering factors are clarified, a larger scale model such as the mesoscale model and the continuum model can be built properly.

The finite difference method, close to the method developed by Bross and Exner [19], is adopted to build computational models in this thesis with two main differences. The first one is the coupled sintering mechanism of the grain boundary, and surface diffusion is considered in these models, and the second one is the curvature (chemical potential) at the triple junction (pore tip) that is numerical solved by applying proper continuous conditions proposed by Pan and Cocks [40]. Then by using different parameter settings and geometries in different studies, the achievements and conclusions are obtained as follows.

Chapter 3 presents a computational study on the role of surface diffusion and external pressure on first-stage sintering of ceramic powders which are densified by grain-boundary diffusion. Two conclusions can be made. The first one is the curvature at the triple junction κ_{tip} as a combination of all sintering variables acting at the triple junction such as diffusivity, external stress, surface tension, the dihedral angle and the local-area curvature. Therefore, it cannot be simply the curvature which is determined by the local geometry of the free surface at the triple junction. The advantage concerning the numerical solution of κ_{tip} is that if there are more driving forces for densification during sintering, they can also be added into the formula of κ_{tip}. The second conclusion is the assumption of fast surface diffusion that is invalid for typical sintering conditions and materials in the first stage of sintering. As the study reveals a simple explanation for the role played by surface diffusion in matter redistribution of the combined grain-boundary and surface diffusion — surface diffusion changes the direction from moving atoms away from a contact neck to depositing atoms

onto it as the rate of surface diffusion increases. The reverse surface diffusion blunts the neck and retards densification. It is shown that this mechanism is significant not only for free sintering but also for pressure assisted sintering.

Chapter 4 presents a computational study of the role played by the fast heating rate on sintering. In this chapter, a temperature dependent model is developed for simulating the sintering with a heating process from 600°C to 1400°C. Then, there is a conclusion that the widely observed SPS's effect on densification can be partially attributed to its fast heating rate, because the rapid heating rate supports sintering to quickly pass through the low temperature domain (600°C to 1200°C in Fig. 4.1), where surface diffusion plays a dominated role due to the backflow mechanism of fast surface diffusion, and then minimises the blunting effect of fast surface diffusion near the triple junction.

Chapter 5 presents a computational study on the effects of inhomogeneity concerning sintering kinetics by observing a de-sintering phenomenon on "three-grain bridge" during sintering. In this study, five critical sintering variables such as the grain size, surface tension and diffusivity are chosen to study the effects of their inhomogeneity on sintering kinetics. Through the analysis of numerical results, the conclusion that the movement of the middle particle (as shown in Fig 5.4) prefers the direction of larger sintering variables is obtained. Furthermore, the effects of some variables' inhomogeneity such as surface tension, the dihedral angle and the initial neck size on sintering kinetics are obvious, while the effects of other variables such as surface diffusivity are weak, because inhomogeneity of different variables has different weights in velocity of middle particles [as Eq. (5.33)].

In addition, the features of computational models listed in chapter two on page 15 have been included in this study.

6.2 Future Work

Several modelling limitations such as distortion of total sintering time, quite simple geometry and only considering two sintering mechanisms still exist in this thesis. For practical applications, these issues should be addressed. Potential research directions are as follows.

1) For the distortion of total sintering time, it can be corrected by adding an empirical formula before the governing equations.

2) For quite simple geometry, a multi-particle model can be achieved by considering the governing equations as a contact law of these particles. For example, the governing equation of grain-boundary velocity V_{gb} can be employed to describe the shrinkage among particles.

3) For only considering two sintering mechanisms, more governing equations of other mechanisms can be added in the methodology section by applying proper continuity conditions.

References

[1] Y. Wang, Y. Liu, C. Ciobanu and B.R. Patton, "Simulating microstructural evolution and electrical transport in ceramic gas sensors," *J. Am. Ceram. Soc.*, **83** 2219-2226 (2000).

[2] S-J. L. Kang, *Sintering Densification, Grain Growth & Microstructure*; pp.7, Elsevier Butterworth Heinemann, Inc., London, 2005.

[3] S-J. L. Kang, *Sintering Densification, Grain Growth & Microstructure*; pp.8, Elsevier Butterworth Heinemann, Inc., London, 2005.

[4] J. Frenkel, "Viscous Flow of Crystalline Bodies under the Action of Surface Tension," *J. Phys.,* **9**, 385-391 (1945).

[5] G. C. Kuczynski, "Measurement of self-diffusion of silver without radioactive tracers," *J. Appl. Phys.*, **21**(7) 632-639 (1950).

[6] W. D. Kingery and M. Berg, "Study of the initial stages of sintering solids by viscous flow, evaporation-condensation and self-diffusion," *J. Appl. Phys.*, **26**(10) 1205-1211 (1955).

[7] R. L. Coble, "Sintering crystalline solids I. Intermediate and final state diffusion models," *J. Appl. Phys.*, **32**(5) 787-793 (1961).

[8] R.M. German, *Sintering Theory and Practice; John Wiley & Sons*, Inc., London, 1996.

[9] M.F. Ashby, *HIP6.0 Background Reading*; Engineering Department, Cambridge University, 1990.

[10] A.C.F. Cocks, "Overview No. 117. The structure of constitutive laws for the sintering of fine grained materials," *Acta Metall.*, **42**, 2191-2210 (1994).

[11] E.A. Olevsky, "Theory of sintering: from discrete to continuum," *Material Science and Engineering*, **R23**, 41-100 (1998).

[12] A.C.F. Cocks, S.P.A. Gill and J. Pan, "Modelling microstructure evolution in engineering materials," *Advances in Applied Mechanics*, **36**, 81-162 (1999).

[13] H. Rafii-Tabar, "Modelling the nano-scale phenomena in condensed matter physics via computer-based numerical simulations," *Physics Reports*, **352**, 239-310 (2000).

[14] F.B. Swinkels and M.F. Ashby, "Overview 11: A second report on sintering diagrams," Acta Metallurgica, **29**, 259-281 (1981).

[15] J. Pan, "Modelling sintering at different length scales," *International Materials Reviews*, **48**[2], 69-85, (2013).

[16]   J. Pan, J.A. Yeomans, P. Smith, S. Kucherenko and R. Dorey, "On the stability of some solid state sintering models," Sintering Technology 2000, Conference Proceedings of Sintering 99, November 1999, Pennsylvania.

[17] C. Herring, "Surface tension as a motivation for sintering," *The Physics of Powder Metallurgy*, New York, McGraw-Hill (1951).

 [18]   F. A. Nichols and W. W. Mullins, "Morphological Changes of a Surface of Revolution due to Capillarity‐Induced Surface Diffusion," *J. appl. Phys.*, **36**, 1826 (1965).

[19] P. Bross and H.E. Exner, "Computer simulation of sintering processes," *Acta. Metall.*, **27**, 1013-1020 (1979).

[20] D. Bouvard and R.M. McMeeking, "The deformation of interparticle necks by diffusion controlled creep," *J. Am. Ceram. Soc.*, **79**[3], 666-672 (1996).

[21] W. Zhang and J.H. Schneibel, "The sintering of two particles by surface and grain-boundary diffusion - a two-dimensional study," *Acta Metall.*, **43**, 4377 (1995).

[22]   W. Zhang and J.H. Schneibel, "Numerical simulation of grain-boundary grooving by surface diffusion," *Computational Materials Science*, **3**[3], 347-358 (1995).

[23]   J. Svoboda and H. Reidel, "Pore-boundary interactions and evolution equations for the porosity and the grain size during sintering," *Acta Metall.*, **40**[11], 2829-2840 (1992).

[24]   W. Zheng and I. Gladwell, "Sintering of two particles by surface and grain-boundary diffusion – a three-dimensional model and a numerical study," *Computational Materials Science*, **12,** 84-104 (1998).

[25]   J. Pan, H. Le, S. Kucherenko, and J.A. Yeomans, "A Model for the Sintering of Spherical Particles of Different Sizes," *Acta Materialia*, **46**, 4671-4690 (1998).

[26] R. Ganeriwala and T. I. Zohdi, "Multiphysics Modeling and Simulation of Selective Laser Sintering Manufacturing Processes," p.299 in 6th CIRP International Conference on High Performance Cutting. Edited by D. Dornfeld and M. Helu, California, 2014.

[27] R. Ganeriwala and T. I. Zohdi, "A coupled discrete element-finite difference model of selective laser sintering," *Granular Matter*, 18 [2] 1-8 (2016).

[28] K. Shinagawa, "Numerical methods for controlling shape, size and microstructure of sintered compacts," *Journal of the Japan Society of Powder and Powder Metallurgy*, **63** [1], 3-9 (2016).

[29] M. Jan and A.C.F. Cocks, "A constitutive model for the sintering of fine grained alumina, Solid Mechanics and its Applications," Vol. 53, Proceedings of the IUTUM symposium on Mechanics of Granular and Porous Materials, Cambridge, 15-17 (1997).

[30] A.C.F Cocks and J. Pan, "The influence of an interface reaction on the creep response of damaged materials," *Mechanics of Materials*, **18**, 269-287 (1994).

[31] G. C. Kuczynski, "The Mechanism of Densification During Sintering of Metallic Particles," *Acta Metall.*, [4], 58–61 (1949).

[32] R. L. Coble, "Initial Sintering of Alumina and Hematite," *J. Am. Ceram. Soc.*, **41** [2] 55-62 (1958).

[33] J. Pan and A. C. F Cocks, "A Constitutive Model for Stage 2 Sintering of Fine Grained Materials—I. Grain-boundaries Act as Perfect Sources and Sinks for Vacancies," *Acta Metall. Matter.*, **42** [4] 1215-1222 (1994).

[34] R. M. McMeeking and L. T. Kuhn, "A Diffusional Creep Law for Powder Compacts", *Acta Metall. Matter.*, **40** [5] 961-969 (1992).

[35] F. A. Nichols and W. W. Mullins, "Morphological Changes of a Surface of Revolution Due to Capillarity-Induced Surface Diffusion," *J. Appl. Phys.*, **36** [6] 1826-1835 (1965).

[36] R. M. German and J. F. Lathrop, "Simulation of Spherical Powder Sintering by Surface Diffusion," *J. Mater. Sci.*, **13** [5] 921-929 (1978).

[37] P. Bross and H. E. Exner, "Computer Simulation of Sintering Processes," *Acta Metall.*, **27**, 1013-1020 (1979).

[38] H. E. Exner, "Neck Shape and Limiting GBD/SD Ratios in Solid State Sintering," *Acta Metall.*, **35** [3] 587-591 (1987).

[39] J. Svoboda and H. Riedel, "New Solutions Describing The Formation of Interparticle Necks in Solid-state Sintering," *Acta Metall. Matter.*, **43** [1] 1-10 (1995).

[40] J. Pan, and A. C. F. Cocks, "A Numerical Technique for The Analysis of Coupled Surface and Gran-boundary Diffusion," *Acta Metall. Mater.*, **43** [4] 1395-1406 (1995).

[41] W. Zhang and I. Gladwell, "Sintering of Two Particles by Surface and Grain Boundary Diffusion – A Three-dimensional Model and A Numerical Study," *Comput. Mater. Sci.*, **12** [2] 84-104 (1998).

[42] A. Maximenko, A. Kuzmov, E. Grigoyev and E. Olevsky, "Direct Multi-scale Modeling of Sintering," *J. Am. Ceram. Soc.*, **95** [8] 2383-2388 (2012).

[43] F. Li, J. Pan, O. Guillon and A. Cocks, "Predicting Sintering Deformation of Ceramics Film Constrained by Rigid Substrate Using Anisotropic Constitutive Law," *Acta Metall.*, **58** [18] 5980-5988 (2010).

[44] A. Akash and M. J. Mayo, "Pore Growth During Initial-stage Sintering," *J. Am. Ceram. Soc.*, **82** [11] 2948-2952 (1999).

[45] W. S. Coblenz, J. M. Dynys, R. M. Cannon and R. L. Coble, "Initial Stage Solid State Sintering Models: A Critical Analysis and Assessment;" p.41 in Proceedings of the Fifth International Conference on Sintering and Related Phenomena. Edited by G.C. Kuczynski. Plenum Press, New York, 1980.

[46] O. Guillon, J. Gonzalez-Julian, B. Dargatz, T. Kessel, G. Schierning, J. Räthel and M. Herrmann, "Field-Assisted Sintering Technology/Spark Plasma Sintering: Mechanisms, Materials, and Technology Developments," *Adv. Eng. Mater.*, **16** [7] 830-849 (2014).

[47] Z. Shen, M. Johnsson, Z. Zhao and M. Nygren, "Spark Plasma Sintering of Alumina," *J. Am. Ceram. Soc.*, **85** [8] 1921-1927 (2002).

[48] Y. Zhou, K. Hirao, Y. Yamauchi and S. Kanzaki, "Densification and Grain Growth in Pulse Electric Current Sintering of Alumina," *J. Eur. Ceram. Soc.*, **24** [12] 3465-3470 (2004).

[49] K. Sairama, J. K. Sonber, T. S. R. Ch. Murthy, C. Subramanian, R. K. Fotedar , P. Nanekar, R. C. Hubli, "Influence of Spark Plasma Sintering Parameters on Densification and Mechanical Properties of Boron Carbide," *Int. J. Ref. Mat. H. Mat.*, **43** 185-192 (2014).

[50] E. A. Olevsky, S. Kandukuri, and L. Froyen, "Consolidation Enhancement in Spark-Plasma Sintering: Impact of High Heating Rates," *J. Appl. Phys.,* **102** [11] 114913–24 (2007).

[51] O. Guillon and J. Langer, "Master sintering curve applied to the Field-Assisted Sintering Technique," *J. Mater. Sci.,* **45** [19] 5191–5195 (2010).

[52] E.Dörre and H. Hübner, *Alumina Processing, Properties, and Applications*; pp. 34-38, Springer-Verlag Press, Inc., Berlin, 1984.

[53] R. M. Cannon, W. H. RHODES, A. H. HEUER, "Plastic Deformation of Fine-grained Alumina (AL_2O_3): I, Interface-controlled Diffusional Creep," *J. Am. Ceram. Soc.*, **63** 46-53 (1980).

[54] S. Prochazka and R. L. Coble, "Surface Diffusion in the Initial Sintering of Alumina: I, II and III," *Phys. Sintering*, **2** [2] 1-18 (1970).

[55] Y. Moriyoshi and W. Komatsu, "Kinetics of Initial Combined Sintering," Yogyo Kyokai Shi, **81** 102-107 (1973).

[56] A. G. Evans, "Considerations of Inhomogeneity Effects in Sintering," *J. Am. Ceram. Soc.*, **65** [10] 497-501 (1982).

[57] R. Raj and R. K. Bordia, "Sintering behaviour of bi-modal powder compacts," *Acta. Mater.*, **32** [7] 1003-1019 (1984).

[58] F. F. Lang, "Densification of Powder Rings Constrained by Dense Cylindrical Cores," *Acta. Mater.,* **27** [2] 697-704(1989).

[59] M. W. WEISER and L. C. D. JONGHE, "Rearrangement During Sintering in Two-dimensional Arrays," *J. Am. Ceram. Soc.*, **69** [11] 882-826 (1986).

[60] O. Sudre and F. F. Lange, "Effect of Inclusions on Densification: I, Microstructural Development in an Al_2O_3 Matrix Containing a High Volume Fraction of ZrO_2 Inclusions," *J. Am. Ceram. Soc.*, **75** [3] 519-524 (1992).

[61] F. F. Lange, "De-Sintering, A Phenomena Concurrent with Densification Within Powder Compacts: A Review," *Sin. Tech.*, **65** [10] 1-12 (1996).

[62] O. Sudre, F. F. Lange, "Considerations of Inhomogeneity Effects in Sintering," *J. Am. Ceram. Soc.*, **75** [12] 3241-3251 (1992).

[63] M. N. Rahaman, *Sintering of Ceramics*; pp. 231, CRC Press, Inc., New York, 2007.

[64] H. E. Exner, *Principles of Single Phase Sintering*; pp. 101, Freund Publishing House, Inc., New York, 1979.